Impact of hydrophobicity and confinement on the structure and dynamics of water at interfaces

Frederik Maria Zysk

Doktorarbeit (Dr. rer. nat.)
dem Department Chemie der Fakultät
für Naturwissenschaften vorgelegt

University of Paderborn
Paderborn, Germany
December 2022

Supervised by:

Prof. Dr. Thomas D. Kühne

Chair of theoretical chemistry, Dynamics of Condensed Matter

University of Paderborn, Paderborn, Germany

Prof. Dr. Matthias Bauer

Chair of sustainable anorganic chemistry

University of Paderborn, Paderborn, Germany

Eidesstattliche Erklärung

Hiermit versichere ich, dass ich die vorliegende Arbeit selbstständig verfasst und keine anderen als die angegebenen Quellen und Hilfsmittel benutzt habe. Alle Ausführungen, die fremden Quellen wörtlich oder sinngemäß entnommen wurden, sind kenntlich gemacht. Die Arbeit war in gleicher oder ähnlicher Form noch nicht Bestandteil einer Studien- oder Prüfungsleistung.

Paderborn den 1. Dezember 2022 ....

Frederik Maria Zysk

Impact of hydrophobicity and confinement on the structure and dynamics of water at interfaces

Frederik Maria Zysk

Abstract

Water is an important part in nearly all life sciences. It is either directly involved in biological, chemical and industrial processes or indirectly as a solvent and building block of life. How hydrophobicity and confinement impact the properties of water is of high importance for applications like coating, surface treatment, membranes, barriers and catalysis among many others. As DFT is a common method to study confined and interfacial systems the accuracy of GGA, meta-GGA and hybrid-GGA functionals is of great importance. A poor description of the interfacial water results in a positive low frequency band for 2D confined water at the water/air interface. Meta-GGA predicts faster dynamics, while hybrid GGA predicts slower dynamics and revPBE0-D3 provides the best results. At the water/air interface I found a correlation between the decay in librational motion of water at times < 0.1 fs in the different layers and the H-bond strength of water. We can predict the H-bond strength from experimentally measurable values as second order reorientation dynamics. Generally long term reorientation dynamics are slowing from layer 1 to bulk with layer 2 and 1 being 7.3 % and 13.3 % faster respectively. We also found considerable impact of the isotope effect on such dynamics. Selectivity and permeability of membranes depend on structural and dynamical properties on a molecular level and their understanding is needed to engineer the membranes of the future.

I modeled idealized silica oxide pores ranging from 0.3 nm to 1.4 nm with hydrophobic (trifluoromethyl/tetramethylsilan) and hydrophilic (hydroxyl) functionalization at the pore walls with liquid water, water vapor and oxygen gas as media. When increasing pore size, surface-water distance measured by Gibbs dividing surface increases as does water diffusion. In hydrophobic confinement the distance between pore wall and water is generally larger and the diffusion is higher than in hydrophilic pores of similar size. Using SFG we show that water in hydrophobic pores is more weakly bonded with the surface indicated by the dominant peak at 3720 cm^{-1}, but bonding with other water molecules is strong. An increase in pore size generally enhances the "liquid" like peaks based on more water-water interactions at the surface. In the hydrophilic systems a peak at around 3680 cm^{-1} becomes more dominant the larger the pore size. Larger hydrophilic systems also show a wide shoulder up to 3500 cm^{-1}, but lack clear "ice" like peaks. In a novel analysis I show that the self-diffusion coefficient vs dipole angle correlation is relatively independent of hydrophobicity, but the prevalence of the dipole angle orientation is diverging strongly, leading to an in dept analysis of most prominent molecular orientations of water at the different surfaces. It is concluded that the slowest water in hydrophilic 1D confinement is probably acting as a H-Bond acceptor to out-of-plane silanols, while water that could act as H-Bond donor is more weakly bonded and more diffusive. The fastest diffusing water is oriented towards the surface with both stretches, indicating that its only interacting weakly as an H-Bond donor to in-plane vicinal silanol groups. In 1D hydrophobic confinement only the prevalence is different. Even so water that is more slowly diffusing is overrepresented in hydrophobic confinement compared to hydrophilic confinement, the overall diffusion is still higher in hydrophobic cases. This is validate by lower H-bond coordination numbers at the surface and in the inner pore for some hydrophobic pore systems and a larger distance between the Gibbs dividing surfaces.

Zusammenfassung

Wasser spielt in fast allen Lebenswissenschaften eine wichtige Rolle. Es ist entweder direkt an biologischen, chemischen und industriellen Prozessen beteiligt oder indirekt als Lösungsmittel und Baustein des Lebens. Wie sich Hydrophobie und Einschluss auf die Eigenschaften von Wasser auswirken, ist von großer Bedeutung für Anwendungen wie Beschichtungen, Oberflächenbehandlung, Membranen, Barrieren und Katalyse und viele andere. Da die DFT eine gängige Methode zur Untersuchung von eingeschlossenen Grenzflächensystemen ist, ist die Genauigkeit von GGA-, Meta-GGA- und Hybrid-GGA-Funktionalen von großer Bedeutung. Eine unzureichende Beschreibung des Grenzflächenwassers führt zu einem positiven niedrigen Frequenzband für eingeschlossenes 2D-Wasser an der Wasser/Luft-Grenzfläche. Meta-GGA sagt eine schnellere Dynamik voraus, während Hybrid-GGA eine langsamere Dynamik voraussagt und revPBE0-D3 die besten Ergebnisse liefert. An der Wasser/Luft-Grenzfläche habe ich eine Korrelation zwischen dem Abklingen der Librationsbewegung des Wassers bei Zeiten $<$ 0,1 fs in den verschiedenen Schichten und der H-Bindungsstärke des Wassers gefunden. Wir können die H-Bindungsstärke aus experimentell messbarer Reorientierungsdynamik zweiter Ordnung vorhersagen. Im Allgemeinen verlangsamt sich die langfristige Reorientierungsdynamik von Schicht 1 zum Bulk, wobei Schicht 2 und 1 um 7,3 % bzw. 13,3 % dynamischer sind. Wir haben auch einen erheblichen Einfluss des Isotopeneffekts auf diese Dynamik festgestellt. Selektivität und Permeabilität von Membranen hängen von strukturellen und dynamischen Eigenschaften auf molekularer Ebene ab, und ihr Verständnis ist notwendig, um die Membranen der Zukunft zu entwickeln.

Ich habe daher idealisierte Siliziumoxidporen von 0,3 nm bis 1,4 nm Größe mit hydrophober (Trifluormethyl/Tetramethylsilan) und hydrophiler (Hydroxyl) Funktionalisierung mit flüssigem Wasser, Wasserdampf und Sauerstoffgas als Medien modelliert. Mit zunehmender Porengröße vergrößert sich der durch die Gibbs'sche Teilungsfläche gemessene Abstand zwischen Oberfläche und Wasser sowie die Wasserdiffusion verschnellert sich. In hydrophobem Einschluss ist der Abstand zwischen Porenwand und Wasser im Allgemeinen größer und die Diffusion höher als in hydrophilen Poren ähnlicher Größe. Mit Hilfe der SFG zeigen wir, dass das Wasser in hydrophoben Poren schwächer mit der Oberfläche verbunden ist, was durch den dominanten Peak bei 3720 cm^{-1} angezeigt wird, aber die Verbindung mit anderen Wassermolekülen im Poreninneren ist stark. Mit zunehmender Porengröße verstärken sich im Allgemeinen die "flüssigkeitsähnlichen" Peaks, die auf stärkeren Wasser-Wasser-Wechselwirkungen an der Oberfläche beruhen. In den hydrophilen Systemen wird ein Peak bei etwa 3680 cm^{-1} umso dominanter, je größer die Porengröße ist. Größere hydrophile Systeme zeigen auch eine breite Schulter bis zu 3500 cm^{-1}, aber keine klaren "eisartigen" Peaks. In einer neuartigen Analyse zeige ich, dass die Korrelation zwischen dem Selbstdiffusionskoeffizienten und dem Dipolwinkel relativ unabhängig von der Hydrophobizität ist, dass aber die Prävalenz der Dipolwinkelorientierung stark divergiert, was zu einer eingehenden Analyse der wichtigsten molekularen Orientierungen des Wassers an den verschiedenen Oberflächen führt. Man kommt zu dem Schluss, dass das langsamste Wasser im hydrophilen 1D-Confinement wahrscheinlich als H-Bond-Akzeptor für Silanole außerhalb der Ebene fungiert, während Wasser, das als H-Bond-Donor fungieren könnte, schwächer gebunden und diffusiver ist. Das am schnellsten diffundierende Wasser ist mit beiden Ausdehnungen zur Oberfläche hin orientiert, was darauf hindeutet, dass es nur schwach als H-Bindungsdonor mit den in der Ebene befindlichen vicinalen Silanolgruppen wechselwirkt. Bei hydrophobem 1D-Einschluss ist nur die Prävalenz anders. Obwohl Wasser, das langsamer diffundiert, in hydrophobem Confinement im Vergleich zu hydrophilem Confinement überrepräsentiert ist, ist die Gesamtdiffusion in hydrophoben Fällen immer noch höher. Dies wird durch niedrigere H-Bindungs-Koordinationszahlen an der Oberfläche und in der inneren Pore für einige hydrophobe Porensysteme und einen größeren Abstand zwischen den Gibbs-Teilungsflächen validiert.

Contents

List of Figures

List of Tables

Motivation

Theoretical approaches, today often using computational methods, have long found their place in life sciences. Understanding natural sciences phenomena by using computational methods to extend our knowledge, solve problems and design processes for a better and more sustainable future is at the heart of what I do. Cooperating with experimental scientists to combine the best of two worlds is of the essence to go new ways.

Classical empirical molecular dynamics, monte-carlo, ab-initio and electron structure calculation methods all play their part in different areas of application. Classical molecular dynamics is best for very large systems, in biological modeling or chemical process research. Ab-inito methods are computationally limited to smaller systems but include nuclear quantum effects and can be used to calculate a wide variety of properties. For example in the use of electron structure calculation to provide information about electron density, polarizability, band gaps and charge transfer. In this way choosing the right method and understanding its limitations for the problem at hand is the basis of all theoretical work in this area.

In this work different life science aspects are studied in ways that are not easily possible with experimental means, but can be used to complement and analyze measurable results. It is this interplay that leads to a better understanding of the world around us. To be able to not rely on chance and simple trial by error we have to understand all aspects that interplay to lead to an observation that was made and to adapt those aspects to engineer materials with the properties we need. One of those aspects nearly always present is water.

Water is the most vital and common substance in life, which translates into extraordinary importance in science and technology. In spite of its apparent structural simplicity, it inhibits special properties and shows unusual features, which stem largely from its internal cohesiveness. Water owes this cohesiveness to its high polarity and the ability to form hydrogen bonds. The dominance of the hydrogen bond makes it one of the most complex molecular liquids. It forms a fluctuating hydrogen bond network in the liquid state and can form several different crystal structures in the solid state.

Its structure and dynamics again completely change at interfaces, in confined geometries and based on the polarity of the environment. How can we explain measured changes in diffusion, spectra and how materials look like to facilitate some of those changes? What has to be done to increase diffusion and selectivity at the same time to engineer membranes with specific properties on demand? To give those answers as many aspects as possible have to be reported and analysis on large amounts of data has to be done. This work is not only scientific but also is the essence of what is today called data science or "big" data. It is important to analyze many different variations of a system and to report a wide set of properties to minimize biases and make sure results are not only based on one very specific system but are true for a wider range of systems.

This work focuses on semi-empirical molecular dynamics and electron structure Density Functional Theory (DFT) in confinement. I begin, briefly explaining the methodology in chapter 2. Most prominently semi-empirical methods in section 2.2 and DFT with dispersion correction in section 2.3. There is also a part about the basics of calculating SFG spectra from the velocity-velocity autocorrelation function in section 2.5 and the adaption to pore one dimensional confinements (pores) in section 2.5.1.

The results start with a discussion of the accuracy of different meta- and hybrid GGA functionals used in DFT (chapter 3). Comparing the SFG response at the water/air interface calculated by DFT with various functionals with experimental references this leads to important knowledge about what exchange correlation functionals to use with DFT at the water-air interface. This work is published in ref. [1]. My part was limited to running molecular dynamics calculating to provide data for further analysis by cooperation partners. Then I study water in 2D confinement, at the water-air interface in chapter 4. I focus on the reorientation dynamics in defined interfacial water layers, the water bonding strength, asymmetry and SFG spectra. The properties are used to report correlation with the H-Bond strength in section 4.3.

Chapter 5 introduces the main part of my research regarding water structure and dynamics in 1D confinement. Starting with an analysis of water inside idealized silica oxide nanopores of different sizes and hydrophobicities. The density (section 5.3.1), H-Bond coordination number (section 5.3.2), diffusion coefficient (section 5.3.3), radial diffusion (section 5.3.4), SFG spectra (section 5.3.6) and angular distributions (section 5.3.7) are reported. The angular distribution and diffusion are combined to gain novel insights into the correlation of structure and dynamics and concluding remarks are given in section 5.4. This is followed in chapter 6 by a special case study on a pore system in cooperation with an experimental group, studying similar properties as before. In chapter 7 I study oxygen gas and water vapor self-diffusion in silica pores as part of a cooperative work with experimental groups engineering silica oxide coatings on top of polymers to optimize material properties for membranes and barriers.

The structure and dynamics in confinement was the main focus of my PhD thesis. At the same time several other studies have been done. Some of them are already published, while others are still in the process of publishing and will be submitted shortly. An Overview can be seen in the Appendix. Those include two studies regarding TMA vapor gas infiltration into polymers, calculating the energies of different reaction paths and using calculated IR spectra to interpret experimental ones. I also did work on nuclear quantum effects and their impact on the water-air interface, water structure at the Weyl semi-metal interface and lastly on N_2 surface adsorption position and its impact on dipole strength and direction to help in the interpretation of ambient pressure XPS. In the last chapter 8 I also thank the people most important to me for successfully conducting research over the last years and in preparing this thesis.

Methodology

2.1 Fundamentals

In the following chapter a short overview of quantum chemistry and semiempirical methods is provided. Generally all theoretical and computational chemistry methods want to solve the time-independent Schrödinger equation as exact and fast as possible:

$$\hat{H}\psi = E\psi, \tag{2.1}$$

where $\hat{H}$ is the hamiltonian operator, ψ the wavefunction of the system and E are the associated eigenvalues. The hamiltonian operater, or total energy operator is the sum of the kinetic energy operator and the potential energy operator. For a molecule the hamiltonian is constructed as

$$\begin{aligned}\hat{H} = \sum_{i}^{electrons} \frac{-\hbar^2}{2m_e}\nabla_A^2 + \sum_{A}^{nuclei} \frac{-\hbar^2}{2m_A}\nabla_A^2 + \sum_{i}^{electrons}\sum_{A}^{nuclei} \frac{-e^2 Z_A}{r_{iA}} \\ + \sum_{i>j}^{electrons} \frac{e^2}{r_{ij}} + \sum_{A>B}^{nuclei} \frac{e^2 Z_A Z_B}{R_{AB}}.\end{aligned} \tag{2.2}$$

Those are in order of the terms from left to right the kinetic energies of the electrons and nuclei, the electron-nuclei interactions, the electrostatic electron-electron and nuclei-nuclei interactions.

2.1.0.1 Born-Oppenheimer Approximation

The Eq. (2.1) is only solvable for one-electron or specifically modelled systems. In the following a number of approximations are made to simplify the process. The Born-Oppenheimer approximation is based on nuclei having a much bigger mass than electrons and their coordinates existing independent of each other [2]. As nuclei move much slower than electrons we can freeze the nuclear positions and simplify Eq. (2.1) to

$$\hat{H}_{el} = \sum_{i}^{electrons} \frac{-\hbar^2}{2m_e}\nabla_i^2 + \sum_{i}^{electrons}\sum_{A}^{nuclei} \frac{-e^2 Z_A}{r_{iA}} + \sum_{i>j}^{electrons} \frac{e^2}{r_{ij}} + \sum_{A>B}^{nuclei} \frac{e^2 Z_A Z_B}{R_{AB}}. \quad (2.3)$$

2.1.0.2 Hartree-Fock

We describe the N electron wavefunction as a Slater determinant of one-electron orbitals to take into account the anti-symmetry of the fermionic wavefunction and the Pauli exclusion principle. With that we can obtain the variationally best orbitals from the solution of the Hartree-Fock equation:

$$F\psi_i = \epsilon_i \psi_i, \quad (2.4)$$

with F as the Fock operator, ψ_i denoting the one-electron orbitals and ϵ_i the orbital energy.

2.1.0.3 LCAO-MO

In a further approximation it is estimated, that electrons experience the "field" of all other electrons as a group, not individually, which introduces the idea of molecular orbitals. The molecular orbitals can be constructed as linear combinations of atom orbitals as

$$\psi = \sum_{k} C_{\mu i}\phi_{\mu}, \quad (2.5)$$

where $C_{\mu i}$ are the LCAO coefficients and ϕ_μ denotes the atomic orbitals.

2.1.0.4 Roothan-Hall Equation

Eq. (2.5) can be written as the Roothan-Hall equation

$$\sum_\nu F_{\mu\nu} C_{\nu i} = \sum_\nu S_{\mu\nu} C_{\nu i} \epsilon_i, \tag{2.6}$$

with the overlap martrix $S_{\mu\nu}$ denoted as

$$S_{\mu\nu} = \int \psi_\mu(r_1)\psi_\nu(r_1) dr_1. \tag{2.7}$$

$F_{\mu\nu}$ are the elements of the Fock matrix and the sum of a one-electron part $H_{\mu\nu}$, which is also described as the core Hamiltonian and a two-electron part $G_{\mu\nu}$ to

$$F_{\mu\nu} = H_{\mu\nu} + G_{\mu\nu}, \tag{2.8}$$

with the different parts being:

$$H_{\mu\nu} = \int \phi_\mu(|\vec{r}|) \left[-\frac{1}{2}\nabla^2 - \sum_A V_A(|\vec{r}|) \right] \phi_\nu(|\vec{r}|) d\vec{r} \tag{2.9}$$

$$G_{\mu\nu} = \sum_{\lambda\sigma} P_{\lambda\sigma} \left[(\mu\nu, \lambda\sigma) - \frac{1}{2}(\mu\sigma, \lambda\nu) \right], \tag{2.10}$$

and the bonding matrix $P_{\lambda\sigma}$

$$P_{\lambda\sigma} = s \sum_i c_{i\lambda} c_{i\sigma}. \tag{2.11}$$

Eq. (2.6) is commenly solved in an iterative manner, also called a self-consistent field procedure (SCF) [3].

2.2 Semi-Empirical Methods

To reduce the computational effort dramatically semi-empirical methods introduce a number of approximations to solve the Roothan-Hall equation more efficiently. Generally some terms may be neglected or simplified in the treatment of multidimensional integrals. They generally use core-approximations, where the core is collapsed with all the inner shell electrons. Furthermore only valence electrons are explicitly treated and a minimal valence basis set is used. Instead of solving the equations mathematically with an ab-initio approach, semi-empirical methods establish new formulas based on parameters, which are optimized and benchmarked for certain atoms or systems. The newer semi-empirical methods make use of Neglect of Diatomic Differential Overlap (NDDO) [4] or modified neglect (MNDO).

2.2.1 Neglect of Diatomic Differential Overlap

The neglect of diatomic differential overlap (NDDO) theory consists of a number of main approximations.

2.2.1.1 Overlap Matrix

The atomic orbitals ϕ_μ are set to be orthonormal, which means that the differential overlap is set to zero between basis orbitals at different atoms. As a consequence only one-center and two-center integrals are calculated, because all three-center and four-center two-electron integrals vanish. It also simplifies the overlap matrix $S_{\mu\nu}$ to the identity matrix and the secular equation gets simplified to a standard eigenvalue problem [4]:

$$S_{\mu\nu} = \delta_{\mu\nu}. \tag{2.12}$$

2.2.1.2 Core-Terms

The one-electron matrix elements $H_{\mu\nu}$ can consist of μ and ν orbitals being on the same or different atoms. Depending on this the integrals are treated differently. If both orbitals are on the same atom, $H_{\mu\nu}$ is not approximated and described as

$$H_{\mu\nu} = U_{\mu\nu} - \sum_{B \neq A} (\mu|V_B|\nu) = U_{\mu\nu} - \sum_{B \neq A} V_{\mu\nu,B}, \tag{2.13}$$

whereas $H_{\mu\nu}$ is devided into interactions of electrons of an atom A with their core and one with other cores $B \neq A$. $U_{\mu\nu}$ is representing the interactions of the core A on μ, ν and $V_{\mu\nu}$ those with the cores of B. Because of symmetry it is possible to denote the diagonal and off-diagonal parts individually:

$$H_{\mu\mu} = U_{\mu\mu} - \sum_{B \neq A} V_{\mu\mu} \tag{2.14}$$

$$H_{\mu\nu} = - \sum_{B \neq A} V_{\mu\nu} \tag{2.15}$$

Where μ, ν are orbitals on different atoms A and B and the off-diagonal matrix elements are calculated with

$$H_{\mu\nu} = \beta_{A,B} S_{\mu\nu}, \tag{2.16}$$

where $\beta_{A,B}$ is the resonance parameter, which is calculated empirically. It is implicated, that there is a linear relationship between the overlap integral of the atomic orbitals on different atoms and the one-electron matrix.

2.2.1.3 Two-Electron Integrals

The two-electron integrals $(\mu\nu, \lambda\sigma)$ are set to zero if μ and ν are not orbitals of the same atom A and λ and σ being orbitals of the same atom B, which results to:

$$F_{\mu\nu} = H_{\mu\nu} + \sum_{B} \sum_{\lambda,\sigma\epsilon B} P_{\lambda\sigma}(\mu\nu, \lambda\sigma) - \frac{1}{2} \sum_{\lambda,\sigma\epsilon A} P_{\lambda\sigma}(\mu\sigma|\nu\lambda), \tag{2.17}$$

where the second term is contributing as long as λ, σ are orbitals of B and the third term as long as λ, σ are orbitals of A.

2.2.1.4 Fock Matrix Elements

With those approximations the Fock matrix elements for NDDO are

$$\begin{aligned} F_{\mu\mu} =& U_{\mu\mu} - \sum_{B\neq A} V_{\mu\mu,B} + \sum_{\lambda\sigma} P_{\lambda\sigma} \left[(\mu_A\mu_A|\lambda_A\sigma_A) - \frac{1}{2}(\mu_A\sigma_A|\mu_a\lambda_A) \right] \\ &+ \sum_{B\neq A} \sum_{\lambda\sigma} P_{\lambda\sigma}(\mu_A\mu_A|\lambda_B\sigma_B) \end{aligned} \tag{2.18}$$

$$\begin{aligned} F_{\mu\nu} =& - \sum_{B\neq A} V_{\mu\nu,B} + \sum_{\lambda\sigma} P_{\lambda\sigma} \left[(\mu_A\nu_A|\lambda_A\sigma_A) - \frac{1}{2}(\mu_A\sigma_A|\nu_A\lambda_A) \right] \\ &+ \sum_{\lambda\sigma} P_{\lambda\sigma}(\mu_A\nu_A|\lambda_B\sigma_B) \end{aligned} \tag{2.19}$$

$$F_{\mu\lambda} = \beta_{\mu\nu} - \frac{1}{2} \sum_{\nu}^{A} \sum_{\sigma}^{B} P_{\nu\sigma}(\mu_A\lambda|\lambda_B\sigma). \tag{2.20}$$

Applying a sp^3-basis set the only contributing orbitals are s and p, so that the following parameters are used to approximate the one-center elements:

$$U_{ss}, U_{pp}$$

$$g_{ss} = (ss|ss), g_{sp} = (ss|pp), g_{pp} = (pp|pp), g_{pp|p'p'} = (pp|p'p')h_{sp} = (sp|sp)$$

$$V_{ss}, V_{pp}, V_{sp}$$

As can be seen the coulombic one-center bielectronic integrals are generally denoted $g_{\mu\nu}$, while exchange one-center bielectronic integrals are denoted $h_{\mu\nu}$. The expressions have to be parameterized with experimental results. Oleari [5] made the first attempt to achieve this by atomic spectroscopy. They used the Koopman-Theorem, which establishes a connection between the highest occupied molecular orbital and the orbital energy and between the lowest unoccupied molecular orbital and the electron affinity.

2.2.1.5 Two-Center Repulsion Integral

The two-center repulsion integrals $(\mu\nu, \lambda\sigma)$ represent the energy of interactions between the charge distributions at an atom A and those at an atom B. Clasically they are equal to the sum over all interactions between the multipole moments M_{lm} of the two charge distributions, where l, m are describing the order and orientation of the multipoles. For semi-empirical treatment the integrals are expanded in terms of multipole-multipole interactions:

$$(\mu\nu, \lambda\omega) = \sum_{l_1} \sum_{l_2} \sum_{m} \left[M^A_{l_1 m}, M^B_{l_2 m}\right] \tag{2.21}$$

The multipoles M$_{lm}$ are described by an configuration of 2^l point charges of magnitude $\frac{e}{2^l}$ and the charge separation D$_l$. The interactions between two multipoles are then calculated by semi-empirically adapted point charges and summing over all the charge interactions. Point charges are denoted as i and j and R$_{ij}$ is the configuration of the point charges. This leads to

$$\left[M^A_{l_1 m}, M^B_{l_2 m}\right] = \frac{e^2}{2^{l_1+l_2}} \sum_{i=1}^{2^{l1}} \sum_{j=1}^{2^{l2}} f_1(R_{ij}), \tag{2.22}$$

whereas $f_1(R_{ij})$ is a semi-empirical function, which should make sure, that the equation behaves properly in the limits of R$_{AB}$ close to infinity or 0. The distances R$_{ij}$ of the point charges are determined by evaluating the relevant point charge configurations. With a minimal sp basis set of valence electrons only four configurations are considered, because higher multipole moments vanish by symmetry.

For the semi-empirical function $f_1(R_{ij})$ there are different approaches, based on the Dewar-Sabelli-Klopman (DSK) [6, 7]

$$f_1(R_{ij}) = \left[R_{ij}^2 + (\rho_{l_1}^A + \rho_{l_2}^B)^2\right]^{-\frac{1}{2}} \tag{2.23}$$

or the Mataga-Nishimoto (MN) [8] approximation. The method makes use of three terms ρ_l with (l=0, 1, 2) for the characterization of monopoles, dipoles and quadrupoles in a sp^3-basis set (quantum number equals 2). The terms are chosen as such, that Eq. (2.22) yields the correct semi-empirical one-center limit for the interactions between two monopoles g$_{ss}$, two dipoles h$_{sp}$ and two quadrupoles h$_{pp}$ [9]. While ρ_0 is equal to $\frac{e^2}{2g_{ss}}$ the values of $\rho_{1,2}$ are calculated numerically.

To calculate the distances R$_{ij}$ from the interatomic distance R$_{AB}$ the relevant point charge distributions have to be defined. With the minimal sp basis set there are only 4 possible configurations. Higher multipole moments of the charge distributions vanish because of symmetry. The charge separations D$_l$ are calculated from the known Slater exponents. As such R$_{ij}$ is defined as

$$R_{ij} = \left[R_{AB}^2 + (D_1 + D_2)\right]^{-\frac{1}{2}} . \tag{2.24}$$

This means the parameters ρ_0, ρ_1 and ρ_2 for the two-center integrals are added to the previously described one-center parameters needed for NDDO. All the parameters need to be empirically calculated for every type of atom.

2.2.1.6 Electrostatic Long-Range Scheme

The DSK, Eq. (2.23) tends to represent a pure Coulomb potential in the long-range limit. When choosing fitting parameters ρ_{0-2}, it can also represent the short-range one-center limit well. At intermediate distances the results are lower than the exact expressions. While the formula can be transformed into a long range sum by performing a laplace transformation, the outcome is a Bessel function which leads to series expansions in both the real and reciprocal space. This is not guaranteed to coverge rapidly [10].

To solve this problem a number of different NDDO long-range schemes have been developed. One of those is splitting the electrostatic contributions into a short-range and a long-range term to

$$\left[M_{l_1m}^{A}, M_{l_2m}^{B}\right] = \left[M_{l_1m}^{A}, M_{l_2m}^{B}\right]_{SR} + \left[M_{l_1m}^{A}, M_{l_2m}^{B}\right]_{LR}. \tag{2.25}$$

The single terms are denoted as

$$\left[M_{l_1m}^{A}, M_{l_2m}^{B}\right]_{SR} = \frac{e^2}{2^{l_1+l_2}} \sum_{i=1}^{2^{l1}} \sum_{j=1}^{2^{l2}} \left[\frac{1}{\left[R_{ij}^2 + (\rho_{l_1}^{A} + \rho_{l_2}^{B})^2\right]^{\frac{1}{2}}} - \frac{1}{(R_{ij}^2)^{\frac{1}{2}}} \right] \tag{2.26}$$

for the short range interactions and

$$\left[M_{l_1m}^{A}, M_{l_2m}^{B}\right]_{LR} = \frac{e^2}{2^{l_1+l_2}} \sum_{i=1}^{2^{l1}} \sum_{j=1}^{2^{l2}} \frac{1}{R_{ij}} \tag{2.27}$$

for the long range interactions. The short-range term can be screened using a proper neighbor-list and the long-range term can be evaluated using an Ewald summation scheme for multipoles [11].

2.2.2 Modified Neglect of Diatomic Overlap

Modified neglect of diatomic overlap (MNDO) is an adaption of NDDO, that introduces new parameters and a new view on core-electron attractions and core-core repulsion [9]. One of the changes is to simulate the effect of the nucleus by its valence shell, which is an s-type shell in a monopole. As such the following changes to experessions were made:

$$V_{\mu\nu,B} = -Z_B(\mu^A\nu^A, s^B s^B), \tag{2.28}$$

with the core charge Z_B and the core-core term being modelled as a two-electron two-center integral between two s-orbitals centered on atom A and B as

$$E_{AB}^{core} = Z_A Z_B(s^A s^A, s^B s^B) + f_3(R_{AB}), \tag{2.29}$$

with $f_3(R_{AB})$ defined as

$$f_3(R_{AB}) = Z_A Z_B(s^A s^A, s^B s^B)\left[e^{-\alpha_A R_{AB}} + e^{-\alpha_B R_{AB}}\right]. \tag{2.30}$$

In Eq. (2.28) and (2.29) the effect of the atomic core is simulated by the valence-shell charge distribution ss. Also the off-diagonal matrix elements of the one-electron operator from Eq. (2.16) are changed to

$$H_{\mu\nu} = \beta_{\mu\nu} = f_4(R_{AB})S_{\mu\nu}, \tag{2.31}$$

with $f_4(R_{AB})$ as

$$f_4(R_{AB}) = \frac{1}{2}(\beta_\mu^A + \beta_\nu^B). \tag{2.32}$$

As a consequence MNDO introduced β_s, β_p, α_A and α_B as new parameters. Other parameters were recalculated and changes to the experimental data sets that are used were made.

2.2.3 PM6

A number of semi-empirical methods were developed based on MNDO, using different numbers of parameters and different methods and experimental data to calculate those parameters. The most notable ones are AM1 [12], PM3 [13] and PM6 [14].

MNDO was known to overestimate the core-core interactions and AM1 increased that error even more. One of the problems in semi-empirical methods is the sole dependency of the core-core interactions on the valence electrons. For small elements with few valence electrons this often makes the core appear to small and introduces errors. In general interatomic distances are assumed too small. Voityuk et al. [15] found, that the errors in heat of formation and geometries were unacceptably large. PM6 introduces new diatomic parameters x_{AB} and α_{AB} to describe those core-core interactions as

$$E_{AB}^{core} = Z_A Z_B (s^A s^A, s^B s^B) \left[1 + x_{AB} e^{-\alpha_{AB} R_{AB}}\right] . \tag{2.33}$$

While this greatly improves the accuracy of elements with few valence electrons, it still fails if two atoms approach each other very closely. It was found, that the cause is the neglect of the unpolarizable core of the atoms involved [14]. To solve this problem a function f_{AB} modelled after the first term of the Lennard-Jones potential [16] was added to the core-core interaction term. The term

$$f_{AB} = \left(\frac{Z_A^{\frac{1}{3}} + Z_B^{\frac{1}{3}}}{R_{AB}} \right)^{12} \cdot 10^{-8} \tag{2.34}$$

provides a strong repulsion at very small distances and vanishes at normal chemical distances.

While this works well for most diatomic interactions, there are faults for some specific interactions. If existing approximations were inadequate, changes were made for specific interactions. The hydrogen bonding energy for example is predicted to small with the standard PM6 core-core terms, so Eq.(2.33) was changed to

$$E_{AB}^{core} = Z_A Z_B (s^A s^A, s^B s^B) \left[1 + x_{AB} e^{-\alpha_{AB} R_{AB}^2} \right]. \tag{2.35}$$

At normal O-H separations around 1 Å this term is similar to Eq. (2.33), but at bigger hydrogen bonding distances it increases the hydrogen bond energy. There is a number of further changes for interactions as C-C, N-H and Si-O.

2.2.4 PM6-FM

While PM6 was an improvement for the calculation of water Troy VanVoorhis et al. found, that the PM6 method gives a very poor oxygen-oxygen pair distribution function and as such a lacking description of the water structure [17]. It predicts a water structure with too short of a first nearest neighbour distance and the later neighbor peaks being too diffuse and overall understructered. They attributed this poor packing in PM6 to an incorrect description of hydrogen bond angles. They also found, that PM6 has wrong radial and angular components of hydrogen bonding and thus produces incorrect pair distribution functions.

As PM6 is a method used to describe chemistry over a large number of elements and is not specifically parameterized for water, Troy van Voorhis et al. decided to reparameterize the PM6 parameters with new force-matching approaches [18, 19] and used a PM6 core-core term:

$$E_{AB}^{core} = Z_A Z_B$$

$$\left[(s^A s^A, s^B s^B)\left(1 + x_{AB} e^{-\alpha_{AB} R_{AB}^2}\right) + a_A^{b_a (R_{AB} - c_a)^2} + a_B^{b_B (R_{AB} - c_B)^2}\right], \qquad (2.36)$$

where a, b and c are PM6 parameters for each atom. The new terms decreased the oxygen-hydrogen core-core repulsion and new atomic parameters promoted a tetrahedral electronic geometry. Both changes lead to a more physical hydrogen bonding and a better liquid water structure [17]. They also report more accurate self-diffusion values than in PM6 and better bond length and values. However it does not describe the electronic properties of water in the gas phase correctly. It overstates dipole moments considerably and understates the gas phase polarizability. This is known since NDDO and the new PM6-FM does not correct this. For a comprehensive table of all the parameter changes read reference [17].

2.3 DFT Theory

The aim of most electronic structure theore is to solve the non-relativistiv time independent many-body Schrödinger equation [20, 21]:

$$\hat{H}\psi(\{R_M\},\{r_N,\sigma_N\}) = E\psi(\{R_M\},\{r_N,\sigma_N\}) \tag{2.37}$$

The many-body wave function ψ is a function of all the spatial coordinates of M nuclei R_M and the spatial and spin coordinates of N electrons $(\{r_N,\sigma_N\})$. The Hamiltonian $\hat{H}$ is such the sum of all interactions between nuclei, electrons and between nuclei and electrons and completely describes the quantum mechanical system. With the Born-Oppenheimer Approximation the contributions from electrons and nuclei are seperated to simplify the equation [22]. The idea is to view the nuclei as fixed and the electrons moving around those fixed nuclei. This is a reasonable approximation because of large differences in mass. The repulsion between nuclei is treated as a constant for a fixed configuration of nuclei and the kinetic term for the nuclei is neglected. The total Hamiltonian $\hat{H}$ is reduced to the electronic Hamiltonian H_{el} as:

$$H_{el} = T_{el} + V_{el-nuc} + U_{el-el} \tag{2.38}$$

or in their fully described form by

$$H_{el}(r_i;R_I) = \sum_i^{N_e} \frac{-\hbar^2}{2m_e}\nabla_i^2 + \sum_i^{N_e}\sum_I^{N} \frac{Z_I}{|R_I - r_i|} + \sum_{i>j}^{N_e} \frac{1}{|r_i - r_j|}. \tag{2.39}$$

This includes the kinetic energy term of electrons T_{el}, the electron-electron U_{el-el} and nuclei-electron V_{el-nuc} electrostatic interactions. It dependent only on the known charges Z_I and positions R_I of nuclei and the number of electrons and nuclei N_e and N. This simplifies the Schrödinger equation to:

$$H_{el}\psi_{el}(r_1,..,r_N;R1,..R_M) = E_{el}\psi_{el}(r_1,..,r_N;R1,..R_M). \tag{2.40}$$

Here the electronic wavefunction ψ_{el} only depends on the N electronic coordinates r_i and the M nuclear parameters R_k. Here we omit to assign the corresponding spin to the spatial coordinates. The electric wavefunction ψ_{elec} that gives the lowest energy E_{el} is deemed the ground state. But this is not trivial to solve as the Hamiltonian depends on the interaction of every electron with all others in its presence. The nuclei repulsion is constant when assuming fixed nuclei and then the total energy is defined as:

$$E_{tot} = E_{el} + \sum_{A=1}^{M} \sum_{B>A}^{M} \frac{Z_A Z_B}{R_{AB}} \tag{2.41}$$

Density-functional theory (DFT) differs from the wave function based methods by using the electron density $\rho(r)$ as the central quantity. It always has 3 dimensions and such reduced computational, which alows its applications to much larger system cost compared to wave function methods. It is described as:

$$\rho(r) = n \int dx_1 dx_2 ....dx_{n-1} |\psi(x_1 x_2 ...x_{n-1})|^2 \tag{2.42}$$

Here we have simplified x_i to represent both spatial and spin coordinates and will do so going forward. $\rho(r)$ determines the probability to find any electron of n inside the volume r with the other n-1 electrons having arbitrary positions and spin in the state of ψ.

Integrating $\rho(\mathbf{r})$ determines the total number of electrons, N:

$$N = \int \rho(\mathbf{r}) d\mathbf{r} \tag{2.43}$$

2.3.1 Thomas-Fermi Model

In the Thomas-Fermi theory [23, 24] electrons are considered as a uniform gas and interactions between electrons and between electron and nuclei are treated classically. The kinetic energy of the electrons is defined as,

$$T[\rho] = C_F \int \rho^{5/3}(r)dr, \tag{2.44}$$

and C_F with the approximation that the kinetic energy depends only on the electron density.

$$C_F = \frac{3}{10}(3\pi^2)^{2/3} = 2.871 \tag{2.45}$$

The total energy in written depending on the electron density is then obtained as

$$E[\rho] = C_F \int \rho^{5/3}(r)dr - Z \int \frac{\rho(r)}{r}dr + \frac{1}{2}\int\int \frac{\rho(r_1)\rho(r_2)}{|r_1 - r_2|}dr_1 dr_2. \tag{2.46}$$

It includes the electron-nuclei and electron-electron interactions as well as the kinetic electron energy and shows that the energy can be determined using the electron density. It does not include correlation or exchange effects but has linear scaling with the number of electrons. One disadvantage is that the Thomas-Fermi approximation is not able to describe chemical bonding.

2.3.2 Hohenberg-Kohn Theorem

The field of rigorous density functional theory was born in 1964. [25] They proved the following:

The external potential $\hat{V}_{ext}$ is a unique functional of $\rho(r)$. This means the ground state density determines the complete Hamilton operator and it is in principle possible to calculate the ground state wavefunction

$$\psi_0(r_1, ..., r_N) = \psi_0[\rho_0(r)] \tag{2.47}$$

as a functional of $\rho_0(r)$. As a consequence, all properties of the system can also be calculated and are given by the expectation value of its operator $\hat{O}$:

$$O_0 = O[\rho_0] = \langle \psi[\rho_0] | \hat{O} | \psi[\rho_0] \rangle. \tag{2.48}$$

The ground state density can be calculated, in principle exactly by using the variational principle. The ground state density is defined as:

$$E_0 = E_g[\rho_0] = \langle \psi[\rho_0] | \hat{H} | \psi[\rho_0] \rangle. \tag{2.49}$$

Every $E[\rho]$ has to be higher or equal in energy to the ground state density and the lowest energy corresponds to the ground state density of the system.

Since now, we know that $\rho(\mathbf{r})$ determines N and V_{ext}, it also determines all properties of the ground state, including the kinetic energy of electrons T_e is a functional of density with the following components:

$$E[\rho] = T_e[\rho] + V_{ext}[\rho] + U_{el}[\rho] \tag{2.50}$$

or:

$$E[\rho] = T_e[\rho] + U_{el}[\rho] + \int dr v_{ext}(r) \rho(r) \tag{2.51}$$

2.3.3 Kohn and Sham Method

In 1965, Kohn and Sham [25] transformed density-functional theory into practical electron structure theory, working on the weakness of Thomas-Fermi. They mainly changed the treatment of the kinetic energy operator by reintroducing the idea of one electron orbitals and approximating the kinetic energy of a system as non-interaction electrons. This marriage of wave function and electron density is done by introducing a reference system of non-interacting single electron functions $\phi_i(r)$, whose density $\rho(r)$ equals the density of the interacting system. The kinetic energy is expressed as:

$$T_s[\langle\phi_i[\rho]\rangle] = \frac{\hbar}{2m}\sum_i^N \int d^3r\phi_i^*(r)\Delta^2\phi_i(r) \tag{2.52}$$

Here $T_s[\langle\phi_i[\rho]\rangle]$ is an explicit orbital but implicit density functional.

To solve this equation quickly there is a need to approximate solutions for T_e and U_{ee}, where $T_2(\rho)$ is the kinetic energy of electrons in a system that has the same density as the real system, but does not include electron-electron interactions. The electron-nuclei interactions tho are still included as in equation X in V_{ext}. The electron self-interaction is included explicitly with the corresponding energy,

$$U[\rho(r)] = U_H[\rho(r)] = \frac{1}{2}\int dr\int dr'\frac{\rho(r)\rho(r')}{|r-r'|} \tag{2.53}$$

which is only an approximation of the total electron interaction energy. This is frequently called a system on non-interacting electrons, but electrons still interact with nuclei.

$$\hat{U}_{cl}(\mathbf{r}) = \int \frac{\rho(\mathbf{r}')}{|\mathbf{r}'-\mathbf{r}|}d\mathbf{r}' \tag{2.54}$$

is a purely classical Coulomb interaction between electrons. It includes electron self-interaction explicitly, since the corresponding energy is

$$E_{cl}[\rho] = \int\int \frac{\rho(\mathbf{r}')\rho(\mathbf{r})}{|\mathbf{r}'-\mathbf{r}|}d\mathbf{r}d\mathbf{r}' \tag{2.55}$$

and it represents interaction of ρ with itself. $\hat{V}_{ext}(\mathbf{r})$ is the external potential, the potential coming from nuclei in this case:

$$\hat{V}_{ext} = \sum_\alpha \frac{-Z_\alpha}{|\mathbf{R}_\alpha - \mathbf{r}|} \tag{2.56}$$

The last functional, $E_{xc}[\rho]$, called exchange-correlation energy, is defined by

$$E_{xc}[\rho] = (T_0[\rho] - T_s[\rho]) + (E[\rho] - E_{el}[\rho]) \tag{2.57}$$

$E_{xc}[\rho]$ includes all the energy contributions which were not accounted for by previous terms. Those are the electron exchange, the election correlation and the difference between the true kinetic energy of the system and the approximated $T_0[\rho]$. The formally exact equation for the total energy then reads as:

$$E[\rho] = T_0[\rho] + \int \left[\hat{V}_{ext}(\mathbf{r}) + \hat{U}_{cl}(\mathbf{r})\right] \rho(\mathbf{r}) d\mathbf{r} + E_{xc}[\rho] \tag{2.58}$$

The kinetic energy $T_s[\langle\phi_i[\rho]\rangle]$ is an approximation of $T[\rho]$, but because of its orbital form it can not be directly minimized with respect to the density. When we combine all terms expect the non-interacting electron kinetic energy together we get a system of non-interacting particles moving in a not yet defined potential $\hat{V}_{eff}$:

$$\hat{V}_{eff}(r) = \hat{V_{ext}}(r) + \hat{U}_{el}(r) + \hat{V}_{XC}(r), \tag{2.59}$$

where we lumped together all terms, except our non-interacting electron kinetic energy, into an effective potential depending upon r, where the exchange correlation potential is defined as a functional derivative of exchange correlation energy:

$$\hat{V}_{xc}(\mathbf{r}) = \frac{\delta E_{xc}[\rho(\mathbf{r})]}{\delta\rho(\mathbf{r})} \tag{2.60}$$

As a consequence the density of the interacting many-body system in potential $\hat{V}_{ext}$ described by a many-body SE can be calculated by solving the equation on non-interaction single-body systems in potential $\hat{V}_{eff}$. The form of equation asks for a solution as a Schrödinger equation for non-interacting particles:

$$\left[-\frac{1}{2}\nabla_i^2 + \hat{V}_{eff}(\mathbf{r})\right] \phi_i^{KS}(\mathbf{r}) = \epsilon_i \phi_i(\mathbf{r})^{KS}. \tag{2.61}$$

With the constraint that the orbitals obtained are valid in reproducing the density:

$$\rho(\mathbf{r}) = \sum_{i=1}^{N} |\phi_i^{KS}(\mathbf{r})|^2. \tag{2.62}$$

Which can be used to calculate an improved potential $\hat{V}_{eff}(\mathbf{r})$ and lead to a new cycle of density that can also be used to calculate the total energy from equation (2.58), in which the kinetic energy $T_0[\rho]$ is calculated from the corresponding orbitals, rather than density itself:

$$T_0[\rho] = \frac{1}{2}\sum_{i=1}^{N} \left\langle \phi_i^{KS} | \nabla_i^2 | \phi_i^{KS} \right\rangle \tag{2.63}$$

and the rest of the total energy as:

$$V_{eff}[\rho] = \int \hat{V}_{eff}(\mathbf{r})\rho(\mathbf{r})d\mathbf{r} \tag{2.64}$$

In practice, total energy is calculated from the converged ground state density using orbital energies ϵ_i as:

$$E[\rho] = \sum_{i=1}^{N} \epsilon_i - \frac{1}{2}\int\int \frac{\rho(\mathbf{r})\rho(\mathbf{r}')}{|\mathbf{r}-\mathbf{r}'|} d\mathbf{r}d\mathbf{r}' - \int \hat{V}_{xc}(\mathbf{r})\rho(\mathbf{r})d\mathbf{r} + E_{xc}[\rho] \tag{2.65}$$

Just as in Hartree-Fock theory, the total energy is not the sum of orbital energies. The electron density unique physical meaning in the Kohn-Sham equations. The eigenvalues on the other hand are used to reproduce accurate densities.

Here electrons move in an effective potential $\hat{V}_{eff}(\mathrm{r})$ which includes electron interaction artificially. The electron-electron interaction is replaced by interaction with some medium that is used to define electron-electron interaction on an abstract level. This does actually overstate the electron-electron interactions. which mimics the electron-electron interaction. This corresponds to non-interacting electrons moving slower than the interacting ones we try to approximate.

2.3.3.1 Exchange Correlation functionals

First implementations of the Kohn-Sham method were using the local approximations to the exchange correlation energy. As those energies are relatively small compared to already known terms simple approximations work reasonably well. LDA or local density approximation is based on homogenous electron gas data. There were two variants of this method: Spin unpolarized (LDF/LDA) and spin polarized (LSD) using both α and β electron densities, rather than a total density.

For historical reasons, the exchange correlation energy was partitioned into 2 parts:

$$E_{xc}[\rho] = E_x[\rho] + E_c[\rho] \tag{2.66}$$

the exchange energy, and correlation energy. The correlation energy of the LDA functional is expressed as:

$$E_{XC}^{LDA} = \int \epsilon_X^{xc-hom}(\rho) + \epsilon_C^{Xc-hom}(\rho) dr \tag{2.67}$$

$$\epsilon_X^{xc-hom}(\rho(r)) = -\frac{3}{4}(\frac{3}{\pi})^{\frac{1}{3}}\rho^{\frac{4}{3}} \tag{2.68}$$

As such the exchange energy can be calculated exactly and $\epsilon_C^{hom}(\rho(r))$ can be fitted from quantum monte carlo calculations [26],

where $\epsilon_c[\rho_\uparrow(\mathbf{r})\rho_\downarrow(\mathbf{r})]$ is the correlation energy per one electron in a gas with spin densities $\rho_\uparrow(\mathbf{r})$ and $\rho_\downarrow(\mathbf{r})$.

The local functionals derived from electron gas data worked suprisingly well, taking into account that they substantially underestimate the exchange energy (by as much as 15%) and grossly overestimate the correlation energy, sometimes by a 100%. The error in exchange is however larger than the correlation error in absolute values. LSD/LDF is known to overbind normal atomic bonds, on the other hand, it produces too weak hydrogen bonds.

Later another class of semi-local functionals attempted to improve functionals by GEA (Gradient Expansion Approximation), in which $E_{xc}[\rho]$ was expanded in Taylor series versus ρ and truncated at a linear term [27]. Good improvements only occurred when the Taylor series was not truncated at a linear term but tried to model the asymptotic behavior and scaling for the usually nonlinear expansion. These are called nonlocal or generalized gradient approximations (GGA) functionals and are given as

$$E_{XC}^{GGA}[\rho] = \int d^3r f(\rho(r), \nabla\rho(r)) \tag{2.69}$$

The most widely know at the time were for example Slater for exchange [28] and VWN for correlation [26]. Today some of the most frequently in use are the PBE [29], BLYP [30] functionals. The functionals can be extended through the Kohn-Sham kinetic density

$$\tau(r) = \frac{\hbar}{2m}\sum_i |\Delta\psi_i(r)|^2, \tag{2.70}$$

to a functional named meta-GGA of the form

$$E_{XC}^{meta-GGA}[\rho] = \int d^3 r f(\rho(r), \nabla\rho(r), \tau(r)). \tag{2.71}$$

The will increase in most cases, but the computational cost increases as well. The last class of functionals that makes up the so called Jakob's "ladder to heaven" are the hybrid functionals. They also include exchange parts calculated from Hartree-Fock, which makes them more accurate but also far more costly.

A more economical way is to include dispersion corrections to for example GGA functionals.

2.3.4 D3 Dispersion Correction

The pairwise DFT-D3 diperson energy with the Becke-Johnson (BJ) [31, 32] damping for periodic systems is given by

$$E_{DFT-D3} = E_{KS-DFT} - E_{disp} \tag{2.72}$$

with E_{KS-DFT} being the KS energy obtained from the self-consistent calculation and E_{disp} is the dispersion correction defined as: with $E^{(2)}$ being defined as

$$E_{disp} = \sum_{AB} \sum_{n=6,8,10..} \sum_{T} \frac{C_n^{AB}}{(|r_{AB} + T|)^n + (a_1 R_0^{AB} + a_2)} \tag{2.73}$$

where the sum is over all atom pairs AB. C_n^{AB} is isotropic dispersion coefficient of the nth order and r_{AB} is the distance vector between the two atoms. The $a_1 R_0^{AB} + a_2$ is used as a damping term at short interatomic distances. [33] The unit cell translation vectors T are added to r_{AB} with the cuoff to sum over all the unit cells in real space. A typical cutoff radius would be around 50 Å.

2.4 ALMO

When studying the nature of intermolecular interactions a novel approach is using energy decomposition analysis (EDA) bases on absolutely localized molecular orbitals (ALMO), called ALMO-EDA [34, 35, 36, 37]. Absolutely Localized Molecular Orbitals Energy-Decomposition Analysis (ALMO EDA) separates the total interaction energy of molecules ΔE_{tot} into

$$\Delta E_{TOT} = \Delta E_{FRZ} + \Delta E_{POL} + \Delta E_{DEL} + \Delta E_{HO}, \tag{2.74}$$

where E_{TOT} is the total interactions energy of the unrelaxed electron densities on the molecules and E_{FRZ} is the orbital relaxation energy. E_{POL} is the intramolecular relaxation associated with polarization of the electron clouds on molecules in the field of each other, E_{DEL} the two-body donor-acceptor orbital interactions and E_{HO} a higher-order relaxation term. Take a look at Khaliullin et al.[38] for an extensive description of ALMO EDA. The two-body component as

$$\Delta E_{DEL} = \sum_{D,A=1}^{Mol} \Delta E_{D \rightarrow A} \tag{2.75}$$

is the most interesting for our work. They arise from the delocalization of electrons from the occupied orbitals of donor D to the virtual orbital of acceptor A. Those energies are obtained self-consistently and include cooperativity effects, which is the foundation of a correct description of the hydrogen-bond networks. As it is a natural descriptor of the bond network there is no need to employ arbitrary definition for hydrogen bonds based on geometry.

2.5 SFG

Another way to obtain information about the structure of the surface is the use of spectroscopic techniques. All vibrational spectra calculated from AIMD are based on the Fourier transform of some autocorrelation function. power spectra use the particle velocities, IT spectra the molecular dipole moments and raman spectra the molecular polarizabilities.

Methods as second-harmonic generation (SHG) [39], sum frequency generation (SFG) and X-ray scattering are also used more and more. Vibrational SFG spectroscopy is especially interesting, because it is capable of probing interfacial molecules selectively and we can obtain information about hydrogen bonding and molecular orientation, which makes it especiialy interesting for aqueous interfaces. This surface specific method is gaining popularity and much work has gone into correlating spectral signatures to specific water structures. In the past those calculations required trajectories of several nanoseconds of length for a SFG response through the dipole moment-polarizability time correlation function. With more accurate, but expensive ab initio MD methods those are difficult to obtain. Nagata et al. [40] presented an algorithm to determine the response from the surface-specific velocity-velocity correlation function. This allows the use of much shorter trajectories and according to Nagata et al., reproduces the results calculated with the dipole moment-polarizability time correlation function. To understand the formalism we start with the IR response based on the velocity-velocity autocorrelation function.

Using the fluctuation-dissipation theorem for the first-order *IR* response the function can be related to the dipole-dipole correlation function as [41]

$$X_{ab}^{(1)}(\omega) = \frac{Q(\omega)}{\omega} \int_0^\infty dt e^{-i\omega t} \langle \sum_{i',j'} \dot{\mu}_{b,j}(0) \mu_{a,i}(t) \rangle \tag{2.76}$$

$$\frac{Q(\omega)}{i\omega^2} \int_0^\infty dt e^{-i\omega t} \langle \sum_{i',j'} \dot{\mu}_{b,j}(0) \dot{\mu}_{a,i}(t) \rangle, \tag{2.77}$$

where $\mu_{a,i}(t)$ is the a component of the dipole moment for the ith molecule at time t. $Q(\omega)$ is the quantum correction factor. The molecular dipole moment can be written as the sum of permanent and transitional dipole moments as

$$\vec{\mu}_i(t) = B_i(t)\left(\vec{\mu}_i^0 + \sum_n \mu_{i,n}^{'} \vec{q}_{i,n}(t)\right). \tag{2.78}$$

$\vec{q}_{i,n}(t)$ is the vector n of molecule i at time t, $\vec{\mu}_i^0$ the permanent dipole moment for molecule i and $\mu_{i,n}^{'}$ the transition dipole moment for the normal mode n. All those vectors are defined specifically in the coordinate system of the molecule. As such $B_i(t)$ is needed to rotate the vectors into the coordinate system of the whole system. With equations 2.77 and 2.78 we get

$$X_{ab}^{(1)}(\omega) = \frac{Q(\omega)}{\omega^2}\int_0^\infty dte^{-i\omega t}\langle\sum_{i,j}\sum_{m,n}\mu_{j,m}^{\prime}\mu_{i,n}^{\prime}\dot{q}_{b,j,m}(0)\dot{q}_{a,i,n}(t)\rangle. \tag{2.79}$$

Here $\dot{q}_{a,i,n}(t)$ denotes the by $B_i(t)$ rotated term of $\vec{q}_{i,n}(t)$. It is important to understand that the OH stretch vibration is dominated by the change in the intramolecular O-H bond. Such the the O-H bond length is used as $\dot{q}_{a,i,n}(t)$. It is described as the bond length vector $\vec{r}_{i'}^{OH}$. [42] The resulting IR response such is

$$X_{ab}^{(1)}(\omega) = \frac{Q(\omega)\mu_{str}^{\prime 2}}{i\omega^2}\int_0^\infty dte^{-i\omega t}\langle\sum_{i',j'}\dot{r}_{b,j'}^{OH}(0)\dot{r}_{a,i'}^{OH}(t)\rangle, \tag{2.80}$$

with the transition dipole moment $\mu_{str}^{\prime 2}$ of the O-H stretch mode combined from $\mu_{j,m}^{\prime}$ and $\mu_{i,n}^{\prime}$.This shows that there is a connection between the velocity-velocity autocorrelation function and the IR response. We can follow a very similar process for the SFG response function. It can be written out in terms of the $\mu - \alpha$ time correlations function:

$$
\begin{aligned}
X_{abc}^{(res,2)}(\omega) &= \frac{Q(\omega)}{\omega} \int_0^\infty dt e^{-i\omega t} \langle \sum_{i',j'} \dot{\mu}_{c,i}(0) \alpha_{ab,j}(t) \rangle \\
&= \frac{Q(\omega)}{i\omega^2} \int_0^\infty dt e^{-i\omega t} \langle \sum_{i',j'} \dot{\mu}_{c,i}(0) \dot{\alpha}_{ab,j}(t) \rangle
\end{aligned}
$$

$\dot{\alpha}_{ab,j}(t)$ is the polarizability in ab direction for the jth water molecule at time t. When we decompose the polarizability tensor α into a permanent and transitional component we get

$$
\alpha_i(t) = B_i(t) \left(\alpha_i^0 + \sum_n \alpha'_{i,n} \vec{q}_{i,n}(t) \right) B_i(t) \tag{2.81}
$$

which can be described by two O-H bond polarizabilities, α_{i1}^{OH} and α_{i2}^{OH} [43] as

$$
\alpha_i(t) = B_i(t) \left(\alpha_{i1}^{OH}(t) + \alpha_{i2}^{OH}(t) \right) B_i(t). \tag{2.82}
$$

Morita et al. [43] showed that the off diagonal elements of the tensor are very small compared to the diagonal ones. Morita et al. [43] showed that the off diagonal elements of the tensor are very small compared to the diagonal ones. With this approximation and $\alpha_{xx}^0 = \alpha_{yy}^0 = \alpha_{zz}^0 = \alpha^0$ and $\frac{\Delta\alpha_{xx}^0}{\Delta r^{OH}} = \frac{\Delta\alpha_{yy}^0}{\Delta r^{OH}} = \frac{\Delta\alpha_{zz}^0}{\Delta r^{OH}} = \alpha'_{str}$ the full response function can be written as

$$
X_{abc}^{res,(2)}(\omega) = \frac{Q(\omega)\mu'_{str}\alpha'_{str}}{i\omega^2} \int_0^\infty dt e^{-i\omega t} \langle \sum_{i',j'} r_{c,j'}^{\dot{OH}}(0) \frac{\dot{\vec{r}}_{j'}^{OH}(t) r_{j'}^{\vec{OH}}(t)}{|r_{j'}^{\vec{OH}}|} \rangle \; if\ a = b,\ else\ 0. \tag{2.83}
$$

α'_{str} and μ'_{str} are the transition polarizability and dipole respectively. As this equation is zero in case of $\langle\ r(t)\rangle = 0$ it is surface specific. Keep in mind that the velocities chosen are specifically for analysis of the stretch vibrations. If one would want to analyze librational or bending motions the defining velocities would have to be changed accordingly. This equation can only be used to calculate the autocorrelation of singular OH stretches. In reality those stretches are interacting with stretches of the same molecule and those of others. The terms intra and intermulecular coupling are used here. The importance of this has been shown experimentally [44] and computationally. [45] The expanded ssVVCF is then given by

$$
\begin{aligned}
&X_{abc}^{res,(2)}(\omega) = \frac{Q(\omega)\mu'_{str}\alpha'_{str}}{i\omega^2} \\
&\int_0^\infty dte^{-i\omega t} \times \left\langle \sum_{i,j} g_t(r_{ij}(0); r_t)\dot{r}_{c,i}^{\mathrm{OH}}(0) \frac{\dot{\vec{r}}_j^{OH}(t)\vec{r}_j^{\mathrm{OH}}(t)}{|\vec{r}_j^{\mathrm{OH}}(t)|} \right\rangle, \qquad (2.84) \\
&if\ a = b,\ else\ X_{abc}^{res,(2)}(\omega) = 0.
\end{aligned}
$$

where $r_{ij}(t)$ is the distance between the center of masses of O-H groups i and j at time t, whereas $g_t(r_{ij}; r_t)$ is the function to control the cross-correlation terms with the cross-correlation cutoff radius of r_t. The intramolecular distances and velocities of O-H group j at time t are denoted as $r_j^{\mathrm{OH}}(t)$ and $\dot{r}_j^{\mathrm{OH}}(t)$, respectively. The quantum correction factor $Q(\omega)$ was taken from Ref. [40] and the Hann window function was applied for the Fourier transformation of the TCF. Even though non-Condon effects are neglected, all intramolecular coupling effects are included in terms of the auto-correlation (Auto-C) and intramolecular cross-correlation (Intra-CC) function, whereas the intermolecular coupling is included using the intermolecular cross-correlation (Inter-CC) function of the O-H stretch modes. Nevertheless, it is important to realize that within this formalism, the amount of correlation is increasing by enlarging r_t. For example, when $r_t = 0$ Å, only the auto-correlation of O-H stretch modes is included. However, increasing r_t to 2 Å entails the correlations within a water molecule, that is the auto-correlation and the intramolecular cross-correlation, but no intermolecular cross-correlation. Although in the latter case, the present ssVVCF technique is generally more accurate and computationally much cheaper than the conventional μ-α TCF approach [40], it still requires rather long trajectories to obtain unbiased SFG spectra.

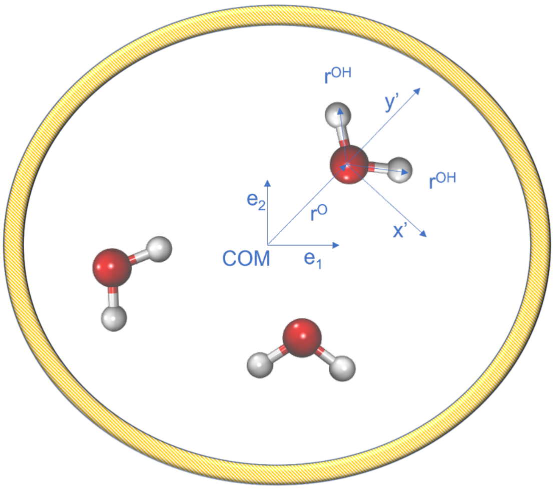

Figure 2-1: Visualization of O-H stretch vectors and their relative position to the center of mass and the pore walls used in equation 2.85

.

2.5.1 Pore adapted SFG

The ssVVCF in the discussed form can only be applied to plain surfaces. The pore systems we want to study cannot be tackled that way.

We are using a surface-specific velocity-velocity correlation function-based SFG algorithm pioneered by Ohto et al. [40] SFG is a second-order nonlinear process able to characterize systems through their vibrational response. In cento symmetric systems, the SFG response vanishes, making it perfect for probing surfaces. [45] To adapt the formula from a planar to a pore interface, the location vector $\vec{r}_{j,O}(t)$ for each oxygen at time t and $\vec{e}_2$ is used to calculate the transition matrix R_α at time t as:

$$\begin{pmatrix} cos(atan2(|\vec{r}_{j,O}(t)\vec{e}_2|, \vec{r}_{j,O}(t)\vec{e}_2)) & -sin(atan2(|\vec{r}_{j,O}(t)\vec{e}_2|, \vec{r}_{j,O}(t)\vec{e}_2)) \\ sin(atan2(|\vec{r}_{j,O}(t)\vec{e}_2|, \vec{r}_{j,O}(t)\vec{e}_2)) & cos(atan2(|\vec{r}_{j,O}(t)\vec{e}_2|, \vec{r}_{j,O}(t)\vec{e}_2)). \end{pmatrix} \tag{2.85}$$

Calculating the new vectors $\vec{r}_j^{\,\prime} = R_\alpha(t)\vec{r}_j(t)$ according to our basis transformation. For a better understanding the vectors used in equation 2.85 are visualized in figure 2-1.

This leaves the full pore adapted formalism as

$$
\begin{aligned}
&X_{abc}^{res,(2)}(\omega) = \frac{Q(\omega)\mu'_{str}\alpha'_{str}}{i\omega^2} \\
&\int_0^\infty dte^{-i\omega t} \times \left\langle \sum_{i,j} g_t(r'_{ij}(0); r'_t)\dot{r'}_{c,i}^{\mathrm{OH}}(0) \frac{\dot{\vec{r'}}_j^{OH}(t)\ \vec{r'}_j^{\mathrm{OH}}(t)}{|\vec{r'}_j^{\mathrm{OH}}(t)|} \right\rangle, \qquad (2.86) \\
&if\ \ a = b,\ \ else\ X_{abc}^{res,(2)}(\omega) = 0.
\end{aligned}
$$

Accuracy of DFT Functionals

3.1 Introduction

Density functional theory-based molecular dynamics (DFT-MD) simulation is a technique for monitoring molecular motions based on the forces calculated using DFT exchange-correlation (XC) methods. [35] While the majority of DFT-MD simulations have employed the generalized gradient approximation (GGA), [46, 30] the recent increase in computational resources and efficient algorithms have allowed for the use of higher-level DFT functionals such as meta-GGA [47, 48] and hybrid-GGA [49, 29] in DFT-MD simulations. Because DFT-MD can deal with complex liquid-solid and liquid-gas interfaces without any empirical force field modeling, it is increasingly being used for gaining molecular-level insight into the structure and dynamics of water at aqueous interfaces. [50, 51, 52, 53, 54, 55, 56] Within the DFT framework, the accuracy of the predicted water properties is sensitive to the adopted XC approximations. Properties of bulk water as well as interfacial water predicted by DFT by applying low levels XC approximations such as GGA are sometimes unphysical. For example, GGA functionals tend to underestimate both the density of bulk water [57, 58] and its surface tension. [59, 1] These limitations arise from three significant drawbacks: (1) GGA methods fail to recover the nonlocal correlation necessary to account for van der Waals (vdW) interactions. [58, 60, 61] (2) GGA methods, which depend only on electronic density n(r) and its gradient Δn(r), provide inaccurate energetics, in particular, for strongly correlated systems. [62] (3) GGA methods suffer from self-interaction error. [63] These three drawbacks may be circumvented by the addition of van der Waals corrections, the extension of GGA to meta-GGA by adding a Δ^2n(r)-dependency in the XC functional, and the extension of GGA to hybrid-GGA by

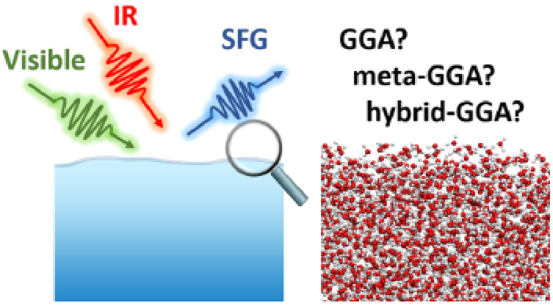

Figure 3-1: Abstract figure of the premise of the study. Accuracy of different DFT functionals studied by using SFG spectra at the interface

mixing exact-exchange with GGA exchangeenergy, respectively. Although the accuracy of the GGA, meta-GGA, and hybrid-GGA functionals for water has been assessed in the gas phase or in the bulk, there is no rigorous and systematic assessment of the XC functionals for describing the structure and dynamics of interfacial water. Because a water

Because a water molecule experiences heterogeneous intermolecular interaction at the interface unlike in the bulk, the systematic comparison of DFT-MD data at the different levels of theory can provide a unique and critical platform for examining DFT accuracy. In this work, we explore the effect of meta-GGA and hybrid-GGA functionals on the structure and dynamics of the interfacial water together with the bulk water. The metrics for interfacial water are relevant to the sum-frequency generation (SFG) spectroscopy, allowing for direct comparison of the simulated data with the experimental results. We find that the revPBE0-D3(0) hybrid-GGA functional shows the best performance among the testified DFT methods, while the M06-L-D3(0) meta-GGA functional shows unexpected poor performance. Subsequently, we discuss the quality of the simulated SFG spectra of O-D stretch mode in isotopically diluted water, by linking with the ranking of the XC functionals, and provide insights into the controversial interpretation of the SFG spectra. [50, 64, 65, 66, 67]

3.2 Computational Methods

Born-Oppenheimer MD (BOMD) simulations were run using BLYP, PBE, and revPBE GGA functionals; M06-L and B97M-rV meta-GGA functionals; and B3LYP, revPBE0, and HSE06 hybrid-GGA functionals with the CP2K code, [68] while Car-Parrinello [69] MD (CPMD) simulation were run using the SCAN meta-GGA functional with the Quantum Espressocode. [70] For hybrid-GGA functionals, we used the auxiliary density matrix method (ADMM). [71] We also used various vdW correction schemes. [60, 72, 32, 73, 74] For describing the core electrons, we used Goedecker-Teter-Hutter pseudopotentials [75] and Ha-mann-Schlüter-Chiang-Vanderbilt norm-conserving pseu-dopotentials [76] in BOMD and CPMD simulations, respectively. We simulated 160 D2O molecules in the simulation box (Lx, Ly, Lz) = (16.63 Å, 16.63 Å, 44.10 Å) for BOMD simulations, while 128 D2O molecules were simulated in the box (Lx, Ly, Lz) = (12.44 Å, 12.44 Å, 50.00 Å) for CPMD simulation. The water-air interface is parallel to the xy plane, and the surfacenormal forms the z-axis. We used the NVT ensemble with the target temperature of 300 K. Furthermore, we performed the MD simulation with the POLI2VS force field model [77] for D2O. For the SFG spectral calculations, we have used the surface-specific velocity-velocity correlation function formalism [41], which was developed for an efficient calculation of the SFG spectra with a limited length of the trajectories. The SFG spectra of isotopically diluted water can be computed from the DFT-MD trajectories of D2O by neglecting the intra/intermolecular couplings. [41] The computed spectra are known to show higher frequency than the experimental data for the O-H (O-D) stretch mode, as the MD simulation with classical nuclei cannot account for nuclear quantum effects. To compensate the red-shift due to the nuclear quantum effects,we multiplied the computed frequency by a factor of 0.96 [78] Asimilar red-shift was also confirmed through the comparison ofclassical and quantum simulation of the SFG spectra. [79]

3.3 Results

To evaluate the different XC functionals, we consider the metrics for the interfacial water including the thickness of the interfacial region (δ), the fraction of the interfacial watermolecules with a free O-D group, the lifetime of a free O-D group (τ_s), average angle of the free O-D group and the surface normal ($\langle\theta\rangle$), together with the bulk water density (ρ) and radial distribution function (RDF) of bulk water. The quantities related with the interface can be connected with various SFG measurements: The fraction of interfacial water with free O-H group was estimated to be 20-25 % from the SFG measurements. [80, 81] Time-resolved SFG measurement identified the lifetime of a free O-H group as 1.1 ps. [82] Furthermore, the information on the free O-H angle was obtained from the polarization-dependent SFG measurement, providing $\langle\theta\rangle = 63°$. [83] Although the data can be essentially obtained for the free O-D group as well, it is currently not available. Thus, we used the POLI2VS data for the reference, because the POLI2VS reproduces the data for the free O-H group accurately. [83, 84] Note that the simulations did not include the nuclear quantum effects, whose effects were examined with force field-based classical MD and quantum mechanical partially adiabatic centroid MD (PA-CMD) simulations. [85, 86] Here, characterizing the free O-D group of the interfacial water is the key for computing the quantities related to the interfacial water. We used the optimal free O-D group definition. [84] The data for selected XC functionals is summarized in figure 3-4. First, we focus on bulk data. The values of the bulk H2O density in our DFT-MD simulations for M06-L-D3(0), SCAN, B97M-rV, and revPBE0-D3(0) are in good agreement with previous reports, [62, 87, 88, 89] while 0.98 g/cm^3 at both the B3LYP-D3(0) and HSE06-D3(0) level have not been reported. Compared with the density of water predicted by the GGA functionals, the density predicted by hybrid-GGA functionals is relatively reduced, yet the density predicted by meta-GGA functionals is relatively elevated.

Overestimation of the density of water with the meta-GGA functionals can be linked with the RDF data. As evident from the absence of the first minimum (hmin) in the RDF for B97M-rV and M06-L-D3(0) functionals, the hydration

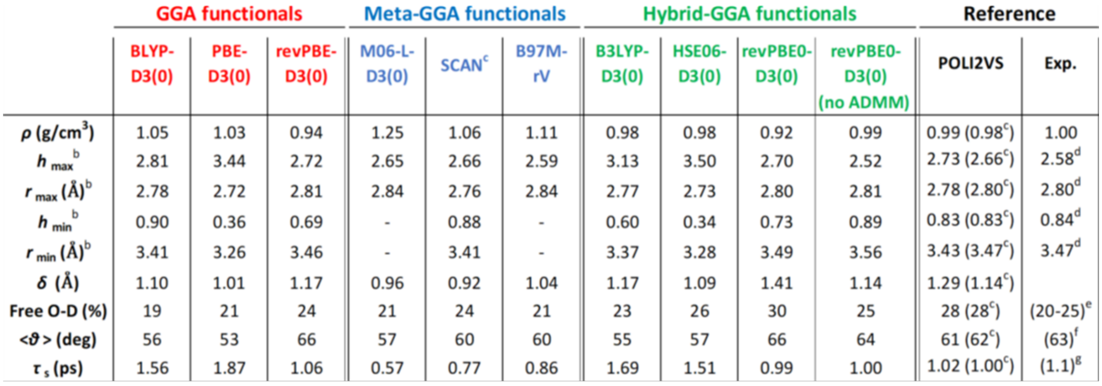

	GGA functionals			Meta-GGA functionals			Hybrid-GGA functionals				Reference	
	BLYP-D3(0)	PBE-D3(0)	revPBE-D3(0)	M06-L-D3(0)	SCAN[c]	B97M-rV	B3LYP-D3(0)	HSE06-D3(0)	revPBE0-D3(0)	revPBE0-D3(0) (no ADMM)	POLI2VS	Exp.
ρ (g/cm^3)	1.05	1.03	0.94	1.25	1.06	1.11	0.98	0.98	0.92	0.99	0.99 (0.98[c])	1.00
h_{max}[b]	2.81	3.44	2.72	2.65	2.66	2.59	3.13	3.50	2.70	2.52	2.73 (2.66[c])	2.58[d]
r_{max} (Å)[b]	2.78	2.72	2.81	2.84	2.76	2.84	2.77	2.73	2.80	2.81	2.78 (2.80[c])	2.80[d]
h_{min}[b]	0.90	0.36	0.69	-	0.88	-	0.60	0.34	0.73	0.89	0.83 (0.83[c])	0.84[d]
r_{min} (Å)[b]	3.41	3.26	3.46	-	3.41	-	3.37	3.28	3.49	3.56	3.43 (3.47[c])	3.47[d]
δ (Å)	1.10	1.01	1.17	0.96	0.92	1.04	1.17	1.09	1.41	1.14	1.29 (1.14[c])	
Free O-D (%)	19	21	24	21	24	21	23	26	30	25	28 (28[c])	(20-25)[e]
<ϑ> (deg)	56	53	66	57	60	60	55	57	66	64	61 (62[c])	(63)[f]
τ_s (ps)	1.56	1.87	1.06	0.57	0.77	0.86	1.69	1.51	0.99	1.00	1.02 (1.00[c])	(1.1)[g]

Figure 3-2: [a]The average error bars for ρ, h_{max}, r_{max}, h_{min}, r_{min}, δ, Free O-D %, $\langle\theta\rangle$, and τ_s,are 0.001 g/cm^3, 0.05, 0.01 Å, 0.03, 0.03 Å, 1.0 %, 1.0°, and 0.1 ps, respectively.[b]h_{max} (r_{max}) and h_{min} (r_{min}) refer to the height (position) of the first maximum and first minimum of the RDF, respectively.[c]Simulations performed using 128 D_2O molecules. [d]RDF data from ref. [90].[e]O-H data from references [81] and [80].[f]O-H data from ref [83].[g]O-H data from ref. [82].

structure simulated with the meta-GGA functionals tends to be more disordered than that predicted by the hybrid-GGA. The improved density by the SCAN functional is attributed to the capture of dispersion forces beyond short-range. Under its influence, the water molecules at intermediate range on the H-bond network are attracted to each other by the non-directional vdW interactions. As a result, the predicted water structure is softened by the increased population of interstitial water molecules. [88] Subsequently, we focus on the structure of the interfacial water. Our data on the thickness of the interfacial water region (δ) indicates that the meta-GGA functionals predict smaller thickness than the GGA functionals, while the hybrid-GGA functionals predict larger thickness. The opposing predictions of the meta-GGA and hybrid-GGA functionals on the thickness δ are consistent with the predicted properties of the bulk water. The different trend is also reflected in the predicted fraction of the interfacial water molecules with free O-D groups; the fraction predicted using hybrid-GGA functionals is greater than that predicted using the GGA functionals, leading to an improved description by reducing the average deviation relative to the reference from 7 % to 3 %. Onthe other hand, the meta-GGA functionals predict free O-D angles very similar to those predicted using the GGA functionals. The free O-D angle also shows the different impact of the meta-GGA and hybrid-GGA. The hybrid-GGA functionals show a deviation of 5° from the reference value, similar to the deviation for the GGA functionals, while for the meta-GGA functionals the deviation is reduced significantly to 3°. As such, the meta-GGA and hybrid-GGA functionals have a different impact on the predicted structure of water at the water-air interface. Now, we focus on the dynamics of interfacial water. Our data show that the GGA and hybrid-GGA functionals predict the free O-D lifetimes of 1.06 - 1.87 ps and 0.99 - 1.69 ps, respectively, while the meta-GGA XC functionals predict 0.57 - 0.86 ps. Compared with the reference value of $1ps$, the meta-GGA functionals predict quite fast free O-D dynamics, while the GGA and hybrid-GGA predict relatively slower dynamics. These different time scales of the dynamics further illustrate the different impact of the meta-GGA and hybrid-GGA functionals on the predicted behavior of the interfacial water and demonstrate that a smart combination of the meta-GGA and hybrid-GGA may substantially improve the description of the interfacial water.

By using the above-listed data, we rank the performance of various XC functionals. The score for the error is computed via

$$K_i^j = \frac{|\chi_i^j - \chi_i^{Ref}|}{\sigma_i} \tag{3.1}$$

where K_i^j is the score of the DFT method j for the calculated property i. χ_i^j denotes the value of the quantity i computed with the method j; χ_i^{ref} is the reference value of the quantity i, and σ_i is the standard deviation for an extensive set of DFT-MD trajectories. [1, 91] The smaller (larger) K_i^j means that the prediction of the XC functional is better (worse). Figure 3-3 shows K, the averaged K_i^j value over i, for each of the different functionals j. This graph demonstrates that the revPBE-D3(0), SCAN, and revPBE0-D3(0) are the best XC functionals at the GGA, meta-GGA, and hybrid-GGA levels of theory, respectively.

Among these, the calculation using the revPBE0-D3(0) hybrid-GGA functional shows the best performance, but at a substantially elevated computational cost (see Figure 3-3 part b). The revPBE-D3(0) GGA functional provides a reasonable description of the interfacial water, at a reduced computational cost. In contrast, the M06-L-D3(0) meta-GGA functional shows rather poor performance,

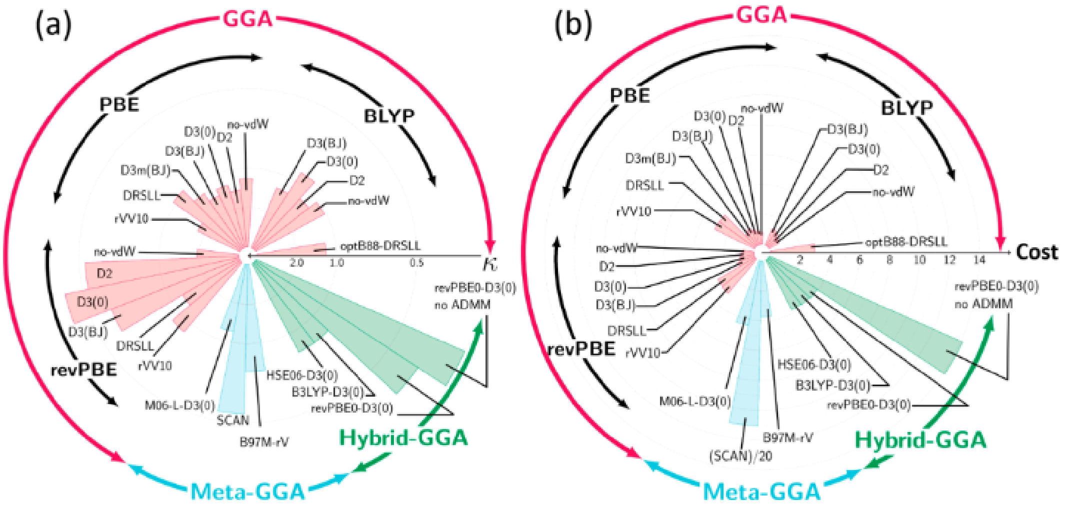

Figure 3-3: (a) Direct comparison of the ability of different functionals to accurately predict water properties. The smaller (larger) score K corresponds to better (worse) predictive power of the functional. (b) Computational cost for different DFT-XC functionals. The data are normalized by the cost of the revPBE-D3(0) GGA functional.

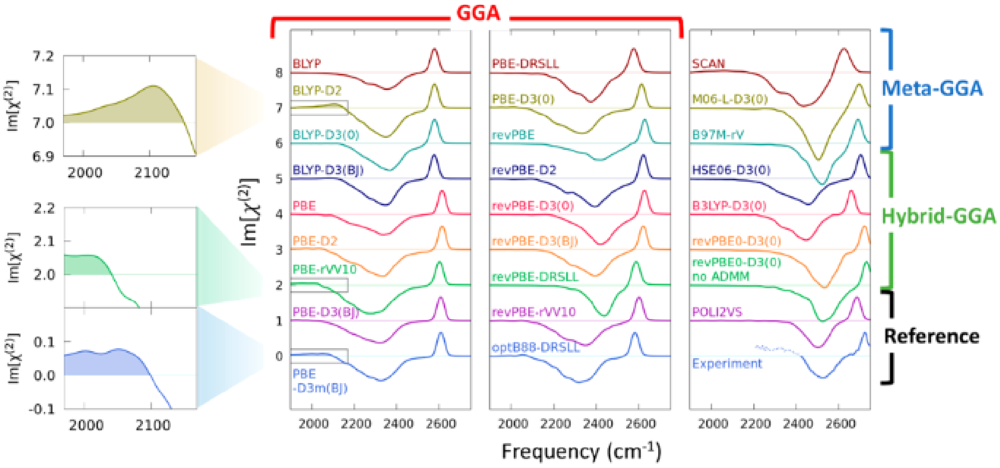

Figure 3-4: Simulated SFG spectra of the O-D stretch mode in H2O for various XC functionals. The POLI2VS spectrum and experimental spectrum were obtained from ref. [92] and ref. [93], respectively. Because the experimental data was obtained for O-H in D_2O, the frequency of the experimental data was scaled down by 0.73546 to convert the O-H stretch frequency to the O-D frequency. Note that a positive band below 2400 cm^{-1} (broken line region) in the experimental data has later been attributed to an experimental artifact of the measurement and should be absent. [66, 67] Each spectrum is offset by increments of 1 for clarity. The free O-D peak top of each spectrum was normalized to 2/3. The highlights of the low frequency regions are displayed in the three panels in the left column.

which is somewhat surprising, given its excellent prediction of gas-phase energetics. It is however consistent with the claim of Medvedevet al. [94, 95] that the XC functionals like M06-L, which does not completely obey exact functional constraints, may produce inaccurate electronic densities. Our data indicate that an accurate description of the electronic density is more critical for bulk and interfacial water than for the gas phase. To connect the predicted structure of water with previously reported experimental SFG spectra, [93] we computed the SFG response of the O-D stretch mode of interfacial HOD molecules in isotopically diluted water (O-D in H2O). The calculated spectra are displayed in figure 3-4. All the simulated spectra show a sharp positive peak at $2550 - 2750 cm^{-1}$ and a broad negative peak centered at $2300 - 2500 cm^{-1}$. A positive (negative) peak corresponds to the free (hydrogen-bonded) O-D group of the interfacial water. [80, 96] Compared with POLI2VS data [92] and experimental data obtained by the Tahara group, [93] we conclude that revPBE0-D3(0) is the best for reproducing the SFG features at the isotopically diluted water-air interface. The excellent reproducibility of the vibrational spectra with the revPBE0-D3(0) functionals can also be found in the infrared spectra of the bulk water. [97] Furthermore, the noticeable differences of the spectra exists with different XC functionals. For example, the spectra calculated at the PBE-D3m(BJ), BLYP-D2, and PBE-rVV10 functionals show a small, but non-negligible positive band below $2100 cm^{-1}$. This is in line with a claim of ref. [65]. However, figure 3-4 clearly illustrates that all the XC functionals showing a positive $2100 cm^{-1}$ band do not reproduce the water properties accurately, implying that the presence of the positive $2100 cm^{-1}$ band may arise from the poor description of the interfacial water. We now discuss the SFG spectra simulated with the meta-GGA functionals. These show a variety of lineshapes, but all deviate somehow from the experimental data. When we focus on the data with the SCAN functional, one can notice that the negative feature is remarkably broad. In fact, the full width at half-maximum of the negative peak is $238 \pm 32 cm^{-1}$, twice larger than the experimental data of $130 cm^{-1}$. [93]

Even compared with BLYP-D3 (0) data of $189 \pm 13\ cm^{-1}$, the SCAN functional predicts a very broad feature elongated to the low-frequency region. These observations may explain the controversial assignment of the SFG spectra of

H2O at the water-TiO2 interface [50, 64], where BLYP-D3(0) does not showa ny positive SFG peaks in the low-frequency O-H stretch region, while the SCAN functional does indicate a positive peak in this frequency region. According to the current data, remodeling these SFG spectra with accurate XC functionals such as revPBE0-D3(0) or meta-hybrid GGA functionals such as SCAN045 is essential for resolving the controversy. In conclusion, we have tested the quality of various GGA, meta-GGA, and hybrid-GGA functionals for a description of the structure and dynamics of water at the air-water interface. We established the significantly distinct impacts of the extension from GGA to meta-GGA and that to hybrid-GGA on the interfacial structure and dynamics. In particular, meta-GGA functionals tend to predict faster dynamics, while hybrid-GGA functionals tend to predict slower dynamics. This indicates that an appropriate combination of meta-GGA and hybrid-GGA may improve the description of interfacial water.Among the XC functionals considered here, revPBE0-D3(0) provides the best performance, while the unconstrained M06-L-D3(0) meta-GGA functional shows poor performance. Linking our results with the poor electron density prediction of the M06-L method indicates that the structure and dynamics of water at the water-air interface highlight the importance of the accurate electron density prediction. By combining the information on the performance of the XC functional with the simulated SFG spectra of water, we found that the poor description of interfacial water tends to generate a positive low-frequency O-D stretch band. The SCAN functional tends to elongate the negative hydrogen-bonded O-D band to the low-frequency region excessively,which differs significantly from the experimental data. Again,the revPBE0-D3(0) predicts the SFG data most accurately.Our observations clearly guide the choice of the XC functional for simulating aqueous interfaces

Unravelling the relationship between the H-Bond strength and the reorientation dynamics at the water/air interface

4.1 Introduction

The water/air interface is ubiquitous in nature. It is present both in macroscopic length scales – in oceans and fresh water resources – and microscopic ones – e.g., in atmospheric [98, 99, 100], marine [101, 99] and therapeutic [102] aerosols; in natural and artificial superhydrophobic surfaces [103]; in surfaces with the ability to adhere to hydrophobic surfaces both in wet and dry conditions [104]. This interface is not an innocent bystander, rather it plays a key role in chemical and physical processes in biology and aqueous chemistry [105, 96, 106]. The chemistry and physics of the air/water interface controls, e.g., the super hydrophobic nature of a surface coating [103], the production of gaseous Cl_2 in aqueous marine aerosols [101], gas exchange [107, 108] and the production of gaseous Cl_2 in aqueous marine aerosols [101]. These strong interfacial effects directly reflect the fact that interfacial water differs from water in the bulk.

A number of experimental and simulation studies have revealed that water molecules at a macroscopic air/water, or air/aqueous solution, interface have both different structure and kinetics that water molecules in the bulk [109, 110, 111, 112, 113, 114, 115, 116, 56].

Most prior computational studies of the air/water interface have used simple empirical potentials which were developed to reproduce the properties of water in the bulk near room temperature. These models potentials necessarily perform far less well at other temperatures [117], are intrinsically unable to capture the change in polarization that water molecules experience when at the interface, and capture nuclear quantum effects only implicitly, at the temperature and for the properties for which they were parameterized. An exception are a newer class of polarizable force fields [118]. Both polarizability and nuclear quantum effects strongly contribute to the properties of water – including their temperature dependence – [119, 120, 121, 122], making ab-initio molecular dynamics simulations explicitly including nuclear quantum effects highly desirable for the study of water. Because of the high computational cost involved in simulating an interface, such simulations are a relatively new occurrence [55].

The most salient feature of water is its ability to hydrogen bond. This ability is hindered when water meets an interface, with both simulation and experiment suggesting that circa 20 % of water hydroxyls at the air/water interface do not hydrogen bond [109, 111, 115, 56, 123, 55, 124, 122]. Furthermore, X-ray absorption spectroscopy experiments and simulations suggest that the intermolecular $\mathrm{O}\cdots\mathrm{O}$ distance increases by circa 6 % at the air/water interface [125, 122], which hints that the strength of the remaining hydrogen bonds in the inter-facial region may differ from bulk or that interfacial water is only under coordinated [126, 127]. The hydrogen bond strength can be studied using information from the OH stretching mode [128, 129, 130]as a weaker H-Bond increases the O-H stretch frequency. Infrared (IR) absorbance and Raman scattering spectroscopy [131, 132, 133] are used to study H-Bonds, but are not surface specific. The response will be noisy from bulk molecules. When only studying inter-facial regions at the interface various experimental studies [134, 135, 136, 137, 96] use Sum-frequency generation (SFG) spectroscopy as a convenient tool, that combines IR and visible pulses to selectively probe inter-facial molecules. Symmetry selection rules lead to bulk responses canceling out. Molecular Dynamics (MD) calculations of the SFG spectra are used to gain inside into the structure and dynamics at the interface [138, 126, 40] and to validate the accuracy of water models [1, 139, 85] reproducing experimental results. It has been found, that the SFG response vanishes from a distance of 5 Å to the surface [126] and that the property changes at the interface are based on an under-coordination of water molecules leading to a "free" O-H peak at around 3700 cm^{-1}, and two hydrogen bounded peaks at 3200 cm^{-1} and 3400 cm^{-1}. Often those two pikes are called "ice-like" and "liquid-like". [135, 81, 55]

Directly characterizing the strength of hydrogen bonds can now be done via energy-decomposition analysis methods such as those based on absolutely localized molecular orbitals (ALMO EDA [38]). This method decomposes interactions into physically meaningful components, enabling deeper insights into intermolecular bonding than the traditional total-energy electronic structure methods. [38, 140, 141] ALMO EDA has been used to investigate the chemical bonding in molecular gas-phase complexes [142, 143, 144]. This method was also used to investigate periodic condensed phase systems: Specifically, it was used to quantify the contribution of the five strongest donor-acceptor interactions to the average delocalization energy of a molecule [34]. The two strongest donor and acceptor interactions are responsible for 93 % of the total delocalization energy of a molecule, while there is a considerable asymmetry of those two strongest interactions.

Energy decomposition analysis provides invaluable insight into hydrogen bond strength, but at great computational cost; its output also cannot be directly compared with experiment. It is thus advantageous to look for observables that give insight into hydrogen bond strength and which are both easily calculated from molecular dynamics trajectories and are also experimentally probable. Prior experimental and computational work has shown that the short time ($<$ 200 fs) reorientation dynamics of the water hydroxyl groups (libration) is related to the hydrogen bond strength [145, 146, 147, 119]. The librational motion is commonly described as forming a cone in the H-bond donor-acceptor direction. The semi-angle of the cone was reported to be inversely proportional to the H-bond strength.

In this work we use quantum molecular dynamics simulations and energy decomposition analysis to address two outstanding questions critical for our understanding of the air/water interface. We investigate the picosecond reorientation dynamics of water molecules as a function of their position relative to the instantaneous air/water interface using models that include polarizability and nuclear quantum effects. To further put those results into perspective we use surface-specific velocity-velocity correlation function (ssVVCF) method [41] to calculate the SFG response as basis for analyzing the structure and dynamics in the different layers.

We use density functional theory (DFT) coupled with ALMO EDA energy decomposition analysis to characterize the average hydrogen bond strength also as a function of the position of each water molecule relative to the instantaneous water/air interface. Finally, we investigate the correlation between the average H-bond strength and short time (< 200 fs) reorientation of water hydroxyl groups with the aim of assessing whether the later observable, which was found to correlate with hydrogen bond strength in the bulk [145], strongly relates to H-bond strength also at the water/air interface.

4.2 Computational Details

4.2.1 Ring Polymer Molecular Dynamics (RPMD) simulation

The system is equilibrated in an NVT ensemble for 10 ps, followed by a centroid molecular dynamics simulation of 8 ps length. The simulation was performed at 300 K using the q-TIP4P/F model by Haberson et al. [148], including a three body correction (E3B) with 32 beads. For the E3B correction, code and parameters published by Tainter et al. [149] were used. The time-steps were chosen at 0.1 fs, whereas every fifth time-step was written into the trajectory and no mts-scheme was applied. The beads were contracted to 1 for both Ewald and Lennard Jones interactions. All other interactions were computed using 32 beads. To average the data, a series of 250 statistically independent trajectories were computed. The model of the water/vapor interface consisted of a bulk water part of $7 \times 7 \times 7$ molecules in a cubic cell of 21.75 Å length. The cell was expanded in z-direction by a factor of 5 to the final dimensions of $21.75 \times 21.75 \times 108.75$ Å to model the water surface.

4.2.2 ALMO EDA

To calculate the average H-bond energy in the various layers and bulk we used 3500 snapshots from a 70 ps long DFT MD simulation with 384 water molecules in a $15.64 \times 15.64 \times 84.00$ Å slab. It was run in an NVT ensemble with a stepsize of 0.5 fs. For each snap the two strongest acceptor and donor interactions of molecules were taken into consideration (see Ref. [37]). For each molecule in layer 1, layer 2 and bulk the average of those interactions was taken into account to approximate the H-bond energy.

4.2.3 Surface-specific velocity-velocity correlation function

A surface-specific velocity–velocity correlation function-based SFG algorithm pioneered by Ohto et al. [41] was used. SFG is a second-order nonlinear process able to characterize systems through their vibrational response. In centro symmetric systems, the SFG response vanishes,making it perfect for probing surfaces defined as:

$$\begin{gathered} X_{abc}^{res,(2)}(\omega) = \frac{Q(\omega)}{i\omega^2} \\ \int_0^\infty dt e^{-i\omega t} \times \sum_{i,j} g_t(r_{ij}(0); r_t) r_{c,j}^{\dot{O}H}(0) \frac{\dot{\vec{r}}_j^{OH}(t) r_j^{\vec{O}H}(t)}{|r_j^{\vec{O}H}|} \rangle \ if \ a = b. \end{gathered} \tag{4.1}$$

If a equal b is not true the whole term is set to zero.

Where $r_{ij}(t)$ is the distance between the center of masses of O-H groups i and j at time t, $g_t(r_{ij}; r_t)$ is the function to control the cross-correlation terms with the cross-correlation cutoff radius of r_t. The intra-molecular distances and velocities of O-H group j at time t is denoted as $\vec{r}_j^{OH}(t)$ and $\vec{r}_j^{OH}(t)$, respectively. The quantum correction factor Q(ω) was taken from Ref. [41] and the Hann window function was applied for the Fourier transformation of the time-correlation function. Even though non-Condon effects are neglected generally all intra-molecular coupling effects are included. [45] In our study, the cutoff r_t is set to 2 Å, thus only including auto-correlation effects. For every water layer the 250 independent RPMD trajectories were used to calculate the individual response and the average of those 250 calculations is reported. A more in dept methodology overview is given in chapter 2.5.

4.3 Results

4.3.1 Instantaneous water/air layer

To study the processes at the water/air interface, a reliable definition of the interface itself is needed. Using a surface definition based on time-averaged density functions neglects spatial fluctuations in space and time. The method of Willard and Chandler is employed here [150]. Instead of using a time-averaged density-field, a coarse-grained but time-dependent density-field in terms of Gaussian functions, located at the center of mass of the water molecules is used. With this mechanism it is possible to deduce the proximity of all water molecules from the instantaneous interface for every time step. The proximity a_i of the *ith* water molecule from the instantaneous interface for every step can be averaged over all instantaneous interfaces. The ensemble-averaged interface and the corresponding mean proximity is obtained as

$$\vec{a}_i = [\langle s \rangle - r_i] \cdot \langle n \rangle \big|_{\langle s \rangle = \langle s \rangle_i} . \tag{4.2}$$

Kessler et al. [56] refer to the three distinct segments of 3 Å each as instantaneous water layers 0 to 2, from top (vapor) to bottom (bulk), which were deducted because of varying water configurations and orientation. Whereby 2.5 Å of the topmost layer 0 are actually located in the vapor phase. While the molecules in layers 0 to 2 have a distinct structural order, phases beyond Layer 2 do not obey any structural order and correspond to bulk water. Layer would end in an approximate distance of 6.5 Å from the surface. Other studies have found, that depending on the definition of distance molecules only as deep as 5 Å show bulk properties [126].

Layer 0 cannot be viewed as a genuine water layer, but rather as a sparse population of water molecules with a higher proximity to the vapor phase than to the first water layer and in this study too few water molecules resided in the corresponding layer at all times to make analysis statistically viable. Going forward layer 1 is considered the topmost interface layer in all analysis.

4.3.2 Reorientation dynamics of OH groups

We calculate the second order rotational dynamics using a second order autocorrelation function similar to previous work by Vila Verde et al. [109] as

$$P_2 = \left\langle \frac{1}{2}(3 \cdot cos^2(\vec{u}_0 \cdot \vec{u}_\tau) - 1 \right\rangle, \tag{4.3}$$

where $\vec{u}$ is the vector characterizing the orientation of an OH group. The maximum of the function is at 1, where a perfect orientation correlation occurs and it has a minimum of -0.5, where all OH groups are orthogonal to their initial orientation. $P_2 = 0$ represents the state of perfect decorrelation. Only OH groups, which are at the same position at $t = 0$ and $t = \tau$ are included. Vila Verde et al. [151] also used this method in a later study to investigate the reorientation dynamics of OH groups in solutions of magnesium sulfate and cesium chloride. Vila Verde et al. [109] also found, that a bi-exponential fit of the form

$$P_2(\tau) = a \cdot exp\left(\frac{-t}{\tau_s}\right) + c \cdot exp\left(\frac{-t}{\tau_l}\right) \tag{4.4}$$

describes the reorientation dynamics reasonably well. The first term represents the short-time decay through the librational motion, while the second term describes the long-time reorientation of OH groups.

We use this approach fitting the reorientation dynamics in the interfacial layers 1, 2 and bulk to a bi-exponential function (Section 4.3.2) with τ_s and τ_l representing the short- and long-time characteristic dynamics. Those decay times can be seen in Table 4.1 labeled as τ_s and τ_l. In Figure 4-1 an acceleration of long-time dynamics from bulk to the topmost interface layer can be seen. The decay times in layer 2 and layer 1 are 7.3 % and 13.3 % faster than in bulk respectively. Vila Verde et al. [109] reported 10 % (SPC/E) to 12 % (TIP4P) faster decay times at the interface than in bulk using classical MD simulations in their study. Considering the splitting of their single interface layer into two distinct layers in our work the results are qualitatively very similar.

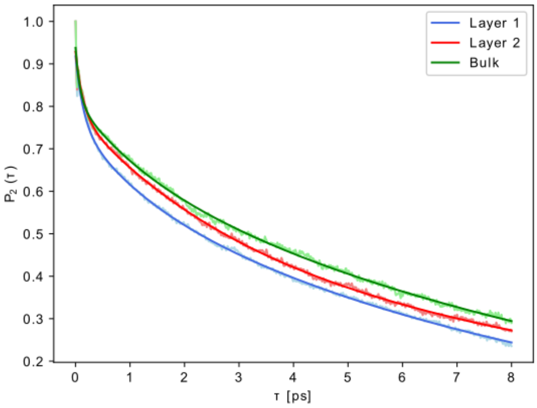

Figure 4-1: Reorientation dynamics of the second order auto-correlation function $P_2(\tau)$ fitted to a bi-exponential function for bulk (green), layer 1 (blue) and layer 2 (red) at the water/air interface.

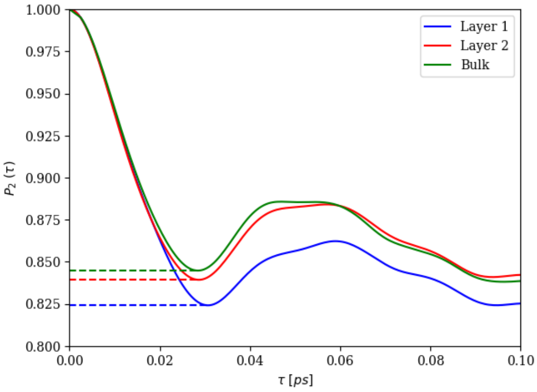

Figure 4-2: Short-time ($\leq$ 0.1 ps) reorientation dynamics $P_2(\tau)$ for bulk (green), layer 1 (blue) and layer 2(red) at the water/air interface. Lines highlight the local minima labeled as $P_2(\tau_{L2})$.

Layer	τ_s	τ_l
1	0.407	7.750
2	0.662	8.289
Bulk	0.622	8.937

Table 4.1: Bi-exponentially fitted short (τ_s) and long (τ_l) decay times for interfacial layers.

The unfitted short-time dynamics for times ≤ 0.1 ps can be seen in Figure 4-2. There is a non-exponential decline at a similar rate for all layers and bulk followed by under-damping. The fitted short-time decay is in the range of 0.41 ps to 0.66 ps (Table 4.1), being the smallest in the topmost layer 1. Layer 2 and bulk have 38.5 % and 34.5 % larger times respectively, which equates to slower short-time reorientation dynamics. In this fit layer 2 behaves very bulk-like in terms of short-time reorientation dynamics, while layer 1 is distinctly different (faster).

4.3.3 H2O, HDO and D2O reorientation dynamics

Similar to the analysis at the water/air interface we compared the water/air dynamics with HDO/air and D_2O/air dynamics. We similarly fitted a bi-exponential function (Section 4.3.2) with with τ_s and τ_l representing the short- and long-time characteristic dynamics to the raw data. As can be seen in Figure 4-3 the long-tim dynamics for HDO follow the same pattern as for H_2O. The dynamics are the fastest in layer 1 followed by layer 2 and are slowest in bulk. Overall the dynamics are between 5.3 % (layer 1) and 17.3 % (bulk) slower than at the water/air interface. For all τ values look at table 4.2. This is expected because of the higher mass of the O-D compared to the O-H group. At the D_2O/air interface the long time dynamics are interestingly diverging from those of the H_2O/water and HDO/water interface. Bulk and layer 2 show very similar long time dynamics, while layer is around 13.6 % faster. It is unclear what change in the D_2O structure leads to this divergence. Further investigations with ALMO EDA or/and calculating SFG spectra would be useful to explain this finding.

Overall D_2O long-time dynamics are the slowest of all three studied systems. Ranging from 17.2 % slower for layer 1 to 27.1 % slower for layer 2. This general

Layer	H_2O ($\tau_s;\tau_l$)	HDO ($\tau_s;\tau_l$)	D_2O ($\tau_s;\tau_l$)
1	0.407;7.750	0.339;8.163	0.258;9.081
2	0.662;8.289	0.285;9.130	0.393;10.534
Bulk	0.622;8.937	0.340;10.485	0.430;10.515

Table 4.2: Bi-exponentially fitted short τ_s and long τ_l range decay times for H_2O, HDO and D_2O interface layers 1, 2 and bulk

slow is easily explained by the isotope effects of D-O compared to O-H. As said before the only divergence from the general trend is bulk D_2O with long-time dynamics as slow as in HDO.

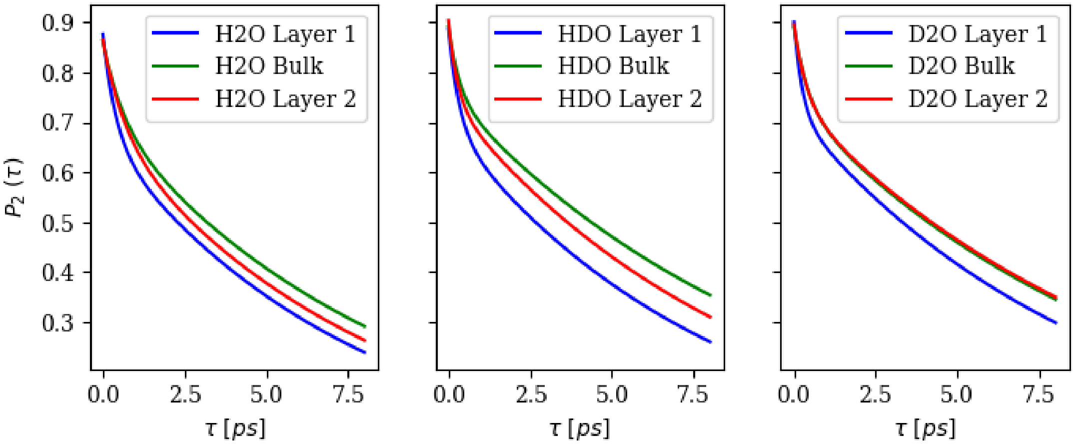

Figure 4-3: Reorientation dynamics of the second order auto-correlation function $P_2(\tau)$ fitted to a bi-exponential function for bulk (green), layer 1 (blue) and layer 2 (red) at the water/air (left), HDO/air (middle) and D2O/air (right) interface.

4.3.4 Water layer SFG calculation

The SFG response divided into the three interfacial layers and bulk for the water molecules can be seen in Figure 4-4. The response for layer 0 shows the characteristic response at 3700 cm^{-1} attributed to "free" or dangling O-H bonds [45, 96]. The strong positive response is based partly on both water stretches pointing towards the surface as SFG is orientation sensitive. A posive imaginary response shows O-H bonds pointing towards the surface, while a negative shows orientation away from the surface. This is supported by the higher donor asymmetry in layer 1. The difference in asymmetry is large as the difference between being a

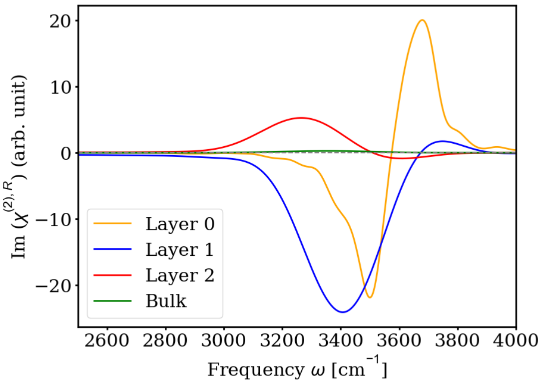

Figure 4-4: SFG response for water layer 0 (orange), layer 1 (blue), layer 2 (red) and bulk water (green). The imaginary response is sensitive to the O-H group orientation. Results are the average of 250 independent calculations from unique trajectories.

donor to water with one or two dangling O-H bonds is huge. The negative peak of layer 0 at around 3500 cm^{-1} is based on the weak donor-acceptor interactions of the molecules having only one dangling 0-H bond. The reponse for layer 1 shows a peak at around 3400 cm^{-1} which is generally attributed to "liquid" like bonded water and a way smaller peak at around 3700 cm^{-1} that is attributed to dangling bonds similar to the more pronounced peak in layer 0. The peak at around 3400 cm^{-1} is oriented away from the surface. According to ALMO EDA data the H-bonds in this layer are much stronger, which can also be observed in the SFG spectra as the calculated frequencies are much lower. O-H stretches pointing downwards are overrepresented.

This aligns well with the results of layer 2 that has an overrepresentation of more strongly bonded O-H stretches at around 3300 cm^{-1} that point upward and as such mirror the peak in layer 1. This diverges from other reports, where a peak at around 3200 cm^{-1} is reported for strongly bonded O-H groups. The bulk response vanishes, which confirms the estimation that water at that surface distance (6.5 Å) has bulk properties. But it also shows, that in layer 2, which is located between 3.5 Åand 6.5 Åaway from the surface. There still is an SFG response based on the asymmetry. The SFG spectrum helps to explain the reorientation dynamics. Overall in layer 1 the O-H groups are more weakly bonded than in layer 2 and the more strongly bonded ones are oriented downwards to layer 2. It such is reasonable that layer 2 is existing in a network of stronger bonding and should reorient more slowly than layer 1.

4.3.5 H-Bond energy and asymmetry

In our ALMO EDA (Table 4.3) calculations the average H-bond energy for molecules in layer 0 is the lowest at 8.04 kJ/mol followed by 14.41 kJ/mol for layer 1 and 17.15 kJ/mol for layer 3. The average strength in bulk is only slightly higher at 17.363 kj/mol. It is important to note, that the energies are the averages of the two strongest donor and acceptor interactions of a molecule. To put the data into perspective the donor asymmetry Υ_D [34] defined as,

$$\Upsilon_D = 1 - \frac{\Delta E_{D \to A^{2nd}}}{\Delta E_{D \to A^{1st}}} \tag{4.5}$$

and the acceptor asymmetry Υ_A

$$\Upsilon_A = 1 - \frac{\Delta E_{A \to D^{2nd}}}{\Delta E_{A \to D^{1st}}} \tag{4.6}$$

can be found in Table 4.3 as well. It shows a larger asymmetry in donor strength in layer 0 (highest) and layer 1 compared to bulk and layer 2. This is to be expected as there are more dangling bonds in the topmost layer 1 and the distortion of the bond network is diminishing towards bulk [55].

A schematic structure of this asymmetric water network at the interface can be seen in Figure 4-5 and is discussed extensively in reference [55].

4.3.6 Relationship between short-time dynamics and H-bond strength

The main idea is to correlate the H-bond strength in different water layers with the short and long-time dynamics, while also taking the SFG response into consideration. The long-time dynamics are clearly in line with the H-bond strength. The long-time reorientation slows from layer 1 to Bulk, which is in line with the increase of H-bond strength in that order.

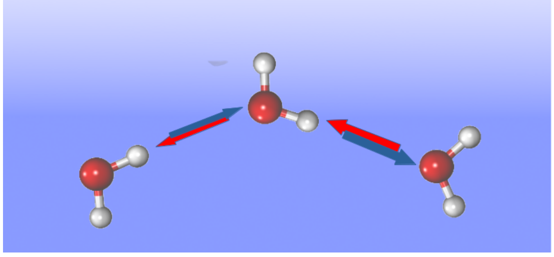

Figure 4-5: Depiction of the two layer surface model of the distorted H-bond network. Showing the dangling molecules in layer 1 and the asymmetric interactions in layer 2. Arrows show the donor (blue) and acceptor (red) interactions.

Layer	E_H	Υ_D	Υ_A	$P_2(\tau_{L2})$	τ_l
0	8.042	0.883	0.879	—	—
1	14.417	0.661	0.614	0.8241	7.750
2	17.156	0.538	0.506	0.8392	8.289
Bulk	17.363	0.541	0.501	0.8447	8.937

Table 4.3: Values of the average H-bond interaction strength E_H in kj/mol, the donor asymmetry Υ_D, the acceptor asymmetry Υ_A, autocorrelation function local minimum $P_2(\tau_{L2})$ in $\tau \leq 0.05$ ps and the long-time reorientation decay time τ_l in interface layers 0, 1, 2 and bulk.

In our study the bi-exponentially fitted values for the short-time decay are outside the timeframe of the dynamics classified as librational motions 2. As the librational motions are happening in timescales ≤ 0.1 ps (Figure 4-2), fitted decay times of 0.4 to 0.6 ps are not representative of the actual phenomena. Short-time decay does not correlate with H-bond strength from ALMO EDA energies in table 4.3 with diverging trends for the water/air interface. Results for HDO and D_2O seen in table 4.2 also show no clear correlation to H-bond strength.

In fact more useful information on short timescales might be extracted by analysing the unfitted data in that time-frame. Looking directly at the raw dynamics for times ≤ 0.1 ps shown in Figure 4-2 there is a steep loss of initial correlation up until times ≤ 0.03 ps. This can be seen as the movement of the O-H stretches in their librational cone. The value of this local minimum is based on the amplitude of this movement as such as a larger decorrelation is equal to a larger amplitude/angle in the OH stretch librational movement.

Our aim is to study the correlation between this librational motion, which is a experimentally measurable observable of P_2 and the H-bond strength quantified by ALMO-EDA. The short-time decorrelation is extracted from Figure 4-2 , labelled as $P_2(\tau_{L2})$ and can be found in Table 4.3. Those values are correlated with calculated ALMO EDA energies in their corresponding layer (Table 4.3). Based on a simple least-square fitting we obtain a linear relationship between $P_2(\tau_{L2})$ and the HB strength $E_{D\to A}$ as

$$E_{D\to A}(kJ/mol) = 151.2515 \cdot P_2\left(\tau_{L2}\right) - 110.124, \tag{4.7}$$

where $E_{D\to A}$ is the H-bond strength in kj/mol and $P_2(\tau_{L2})$ is the correlation value in the local minimum of the L2 librational motion. The mean squared error (MSE) is 0.0778 kJ/mol with a coefficient of determination of 0.957. Keep in mind, that we are only fitting three data points here, but each data point was averaged over a large number of calculations before as we have described in sections 2.4 and 4.2.

We now evaluate the other properties as well. Using the same linear regression to correlate the asymmetry Υ_D and H-bond strength we obtain a coefficient of determination of 0.990 and a mean squared error of 0.139 kj/mol. Υ_A and the H-bond strength show a coefficient of determination of 0.999 and a mean squared error of 0.004 kj/mol. While both values show a high correlation with the average strength Υ_A seems to work especially well.

At last the long-time reorientation decay time τ_l has a coefficient of determination of 0.759 and a mean squared error of 0.4351 kj/mol correlated with the H-bond strength. This shows that $P2(\tau_{L2})$ and Υ_D are by far better predictors of H-bond strength than the long-time reorientation dynamics τ_l.

4.4 Conclusion

We investigated the correlation between the reorientation dynamics and the H-bond strength in distinct layers of the vapor/water interface. Using a bi-exponential fit of the second order rotational autocorrelation function we concluded that it is most useful in describing the long-time reorientation dynamics. The dynamics are supported by SFG spectra calculations showing a blue-shift in the spectrum when moving away from the surface towards bulk. To investigate the correlation between the short-time dynamics and the H-bond strength using the locale minimum of the autocorrelation function resembling the L2 band librational motions appears to be more helpful. In combining this new observable $P_2(\tau_{L2})$ with bond energies from ALMO EDA we found a linear relationship between this experimentally obtainable observable $P_2(\tau_{L2})$ that can predict H-bond strength for the different interface layers and bulk. The donor asymmetry Υ_D is also correlating well with the average H-bond strength showing that lower average strength is majorly based on weakening of the second strongest H-bond.

Impact of hydrophobicity and pore size on structure and dynamics inside nanopores

5.1 Introduction

In restricted or so called confined geometries a high ratio of water molecules is closely interacting with the confining structure. This plays a fundamental role in many natural and industrial processes ranging from geology and biology to chemical engineering. Water absorbed in porous media such as rocks, sand stone, mesoporous membranes, biological cells, microemulsions or bound to macromolecules like proteins are just a few examples of this ubiquitous state. The structural and dynamical properties of water are influenced by the chemical and geometric properties of the confining surface. The hydrogen bond network is altered by the geometric confinement and the competition between the surface-liquid and liquid-liquid interactions. This competition can lead to structures that are not observed in bulk water, which in turn impacts all processes and reactions related to water structure and dynamics. One example of this is the observation that confined water can freeze at 300 K in nanoscale systems [152, 153].

Much research along this line of work studies phenomena arising from water in contact [154, 155] or confined by hydrophilic or hydrophobic materials. [156, 157, 158, 159, 160, 161, 51] The most common examples of hydrophobic confinement are carbon nanotubes [162, 163, 164, 165]. Especially the phenomena of ultrafast water transport and ion selectivity have generated a lot of interest for applications ranging from filtration to energy storage [166].

Among hydrophilic surfaces, silica oxides play a special role as the most abundant solid compound in the earth crust and the main constituent of nanotechnological devices. Numerous technological applications of silica rely on its surface properties and the surface silanol groups serve as hydrogen-bonding sites for a variety of chemical species. Porous silica glass such as Vycor [156, 167], silica gel [168, 169] and mesoporous [170, 171, 158] silica have been used to study absorbed water. They generally manifest well-defined geometries, consisting of a connected network of tubular channels with pore diameter in the nanometer range. Two mesoporous silica with small pore sizes are MCM-41 [172] and SBA-15 [173]. While MCM-41 has pores in the range of less than 2-6 nm [174], SBA-15 has considerably bigger pore radii around 5-10 nm. SBA-15 also exhibits considerable surface roughness attributed to $(\mathrm{Si0}_2)_n$ islands on the surface [175], which influences the water dynamics, for example varying effects on pore-filling have been observed based on different geometries.

Due to the high density and the relatively small pore diameter, these silica materials have very large inner surfaces. The pore-to-pore distance is generally about 20 % larger than the pore diameter. The geometry of the pores is highly anisotropic such that a preferred axis exists in the direction of the pores cylindrical axis and diffusion in the pores exhibits deviations from ordinary diffusion [176]. The surface influences not only the translational but also the rotational degrees of freedom of guest molecules. As the physical properties of the inner surfaces can be chemically modified [177], mesoporous silica materials are very promising candidates for catalytic applications [178, 179].

Confined water can reproduce the properties of bulk water under supercooled conditions, which are difficult to reach in experiments because of homogeneous nucleation [180, 181, 182]. It was shown that crystallization is suppressed in confinement, which is used to study metastable states of supercooled water [183, 184, 185]. Mode coupling theory (MCT), an evolution of glassy dynamics [186] works well in the region of mild supercooling to describe liquids in confinement as distorted, but not as less tetrahedral coordinated [156, 187, 188, 189].

Quite obviously, the pore size impacts the degree of influence of the confinement on the behavior of water within the porous material. [190, 171, 191, 192] The deviation of water behavior depending on pore size compared to the bulk phase has been investigated thoroughly. In a recent study from 2019, Ilgen and coworkers investigated the effect of confinement on the melting/freezing point, density, and surface tension of confined water in various silica (SBA-15 and disordered silica) samples with cylindrical pores. [193] IR and Raman spectra were deconvoluted concerning the contributions of different water phases. A change in pore size from 8 to 2 nm did not strongly influence the IR/Raman spectra compared to bulk water but gets slightly more significant for smaller pores. Similar results were obtained by Le Caër et al. with porous glasses (pore size 8 - 320 nm) [194] and Lendl et al. with porous films (pore size 3 - 8 nm). [195] It has to be pointed out that the influence of pore size on other physical properties like melting, freeing point, surface tension can be more meaningful [196, 197, 198, 199, 200].

These experimental studies have been done on pores greater than 2 nm in diameter. For nanopores mainly theoretical studies have been done regarding the impact of pore size on the dynamics in hydrophobic nanotubes. [163, 165]. In a Review by Hyung Gyu Park et al. [166] studying the structure and dynamics in nanotubes of sizes from 0.8 nm to 2.7 nm it was found that pores smaller than 1.4 nm increasingly diverge from bulk properties regarding the relative Helmholtz free energy and entropic vs enthalpic contributions. They also reported enhancement of water flow in narrow tubes smaller than 1.6 nm.

We generally speak of an ice structure if a high degree of order, i.e., crystal structure, can be achieved. If water molecules assemble in a more ordered structure than liquid water but are not quite crystalline, the term "ice" like water is utilized. It refers to strongly hydrogen-bonded tetrahedrally coordinated water molecules [201] that can be monitored via infrared (IR) spectroscopy. It occurs at wavenumbers of around 3230 cm^{-1} and overlaps with the vibrational band of "liquid" water (3400 cm^{-1}). In this context, the term liquid refers to water molecules that are closely related to bulk water. [202] As mentioned above, the bulk properties of water are dominated by the intermolecular hydrogen bonds between neighboring molecules. Deviations from bulk behavior occur when the hydrogen interactions are disturbed by, e.g., the addition of other molecules or the restrictions through a confined space. [203] The restriction due to confinement, e.g., within a porous structure, can lead to significant changes in the coordination number, in the distance between nearest-neighbor water molecules and the change of the angle of H-O-H (106.8°) and H-O···H (109.7°) because the water molecule is not surrounded by a sufficient number of neighbors, as compared to bulk water or ice. [204, 205]

IR spectra have been used in theoretical and experimental studies to analyze the structure of water in hydrophilic confinement. Alollio et al. [171] found a blueshift of the IR response at the interface compared to bulk, which they explained by a decrease in the coordination number they observed. Another study Sulpizi et al. [51] reported a redshift on an alpha quartz interface attributed to a higher coordination number. A number of experimental studies have also analyzed the neutral hydrophilic quartz-water interface and found the so called "ice" and "liquid" like bands, which generally correspond to responses that can be seen in pure ice and bulk liquid water at frequencies between 3200 cm^{-1} and 3500 cm^{-1}. [206, 207, 154] Another discussion leading from those results is whether water at the interface is actually "ice" and "liquid" like or whether the liquid like response is the interfacial one and more strongly bonded water molecules are located further away from the interface and pointing towards bulk water. Dalstein et al. [208] observed the typical "ice" like and "liquid" like bands on the silica surface but also reported a "free" band at around 3680 cm^{-1}. They even reported that this band is the predominant one. Ellen backhus et al. [209] in response found that this band is most likely related to loosely bound water molecules and not to isolated silanol.

Similarly solid hydrophobic surfaces have been the focus in many studies [210, 211, 81, 212, 213, 214, 215, 209, 96]. Stirnemann et al. showed that water at the hydrophobic surface is mainly made up by two species. "Free" water dangling towards the surface and water tangential to the surface that is more strongly bonded. Zhang et al. called this the ultrafast vibrational dynamics [216] and are based on weak hydrogen bonding at the surface [209]. While Tang et al. [84] added that the definition of "free" water is not clear and supposedly "free" water stretches give rise to the 3600 cm^{-1} and/or 3700 cm^{-1} band based on the specific definition. They attributed "free" water in the 3700 cm^{-1} band having an O-H stretch angle at around 60° relative to the surface normal. While many experimental studies agree on the existence of very weakly hydrogen-bonded water it is not self-evident. It could originate either from a saturation of the hydrogen bond acceptors (silica) or from steric effects based on the confinement and pore size.

Scatena et al. studied the IR spectrum of water at a hydrophobic CCl_4 and hydrocarbon surface. [217] They did report strong structural changes, including a large "free" water peak and did not find an increase in strength of the bonding network with other water molecules or an increase in water-water coordination number. An SFG study by Khatib et al. [218] argued, that the "free" OH peak on the hydrophobic CaF_2 surface is from Ca-OH groups and not from surface water, while Cyran et al. [209] found that the "free" water molecules are situated at the surface. They specifically found that those peaks are correlated with the amount of siloxane bridges in their otherwise hydrophilic pore.

To supplement IR and SFG spectra the angular dipole distribution is helpful. [158, 51] This is true for IR spectra but also to analyze the imaginary part of the SFG response. As the SFG relies on the asymmetry, the total intensity is not shown. The angular distribution can also act as a validation of SFG results. Renou et al. reported a shift of the angular dipole peak from around 60° to 180° when the silica surface is deprotonated. This is a strong shift towards water pointing away from the surface. Cimas et al. [219] studied the angular distribution at the hydrophilic silica surface and found that most angles can be attributed to water interaction with vicinal silanols only. They found maxima of those configurations at around 120° and 50° with minima at 180° and 0°. The contributions of water interacting with geminal silanols (peak at 60°) and isolated silanols (peak at 40°) are relatively small. Apart from this influence Sulpizi et al. also stressed the difference between out-of-plane and in-plane silanols at the surface. [51] They expected weaker bonding when a water is acting as a H-Bond acceptor to an out-of-plane silanol group than when its an H-bond donor to a in-plane silanol.

A number of experimental [220, 116, 221, 222] and computational studies [156, 157, 223] regarding MCM-41 have been carried out in the past, regarding the dynamic properties of water like self-diffusion, hydrogen bonding and translational and rotational motions. Studies have also been carried out at different hydration levels and shown varying water structures and dynamics [174].

Takahara et al. [224] derived the diffusion coefficient of water from quasi-elastic neutron scattering experiments. They found diffusion values between $1.3 \times 10^{-9} m^2/s$ and $1.8 \times 10^{-9} m^2/s$, depending on the fitting method. Spohr et al. [225] reported sub-diffusive behavior at the surface as well. A theoretical study by Bourgh et al. [226] also reported sub-diffusive behavior in hydrophilic silica pores, increasing from $0.17 \times 10^{-9} m^2/s$ to $1.82 \times 10^{-9} m^2/s$ for pore sizes between 1 nm and 4 nm. Newer results by Ab-initio methods measured a diffusion coefficient of only $0.8 \times 10^{-9} m^2/s$ for a 2.2 nm pore. [171] Studies generally agree on a slowdown of water diffusion at the surface. [171, 223, 227, 228] In a rare study Renou et al. [158] reported a sub- to super-diffusive transition towards the surface in a case with sodium cations at the silica surface. They also reported sub-diffusive behavior for pristine pores at the surface and inner pore for their pore with 1.2 nm diameter.

Most past computational studies have used conventional force-field based methods [165, 223, 226, 158, 170]. Those methods are well established, but are based on bulk water as reference, while in confinement a large portion is naturally interfacial. Some studies have employed DFT based AIMD molecular dynamics [51, 219, 171], but they are only done for one (or a limited amount) of systems and system size. Allolio et al. [171] presented an approach at the ab-initio level, including a quantum chemical approach of the actual silica pore itself and a water in MCM-41 calculation.

Because of the scope of aspects and properties that play a role in the dynamics and structure of nanopores, one of the weaknesses of most studies is their limitation on only studying some of those aspects. Only few structural factors are considered or only dynamics is reported. It is also very common that only one pore diameter is considered and generally one type of pore or pore functionalization is considered. This means if we want to compare structure and dynamics over some pore size range and with different levels of hydrophobicity we generally have to rely on many different studies, all of which use different methods.

The aim of this work is to provide a comprehensive study of various structural properties and dynamics over a wide range of nanopores < 2 nm of size. And to study whether there is a correlation between those structural properties and dynamics like translational diffusion.

To that end I decided to use semi-empirical methods. They are based on ab-initio methods, which are important to accurately describe the very important surface interactions, but parameterize parts of the Hartree-Fock equation based on experimental results to lower computational costs. As such they are well versed to use in a study, including a decent number of pore systems for times long enough to extract meaningful diffusion data. One of the problems of known semi-empirical methods as PM6 [15] were inaccurate results of structure and behavior for systems including water. Deficiencies are for example manyfold deviations in bond-length, diffusion and the structure. As water is ubiquitous and important in most biological and chemical processes, this was a big drawback for the use of semi-empirical methods. Lately Welborn et al. [17] published a new parameterisation for PM6, which reproduces accurate structural results for water and generally represents dynamic water behavior much better.

We use those methods to study hydrophilic and hydrophobic silica oxide nanopores of sizes from 0.25 to 1.4 nm of size, where we expect most of the interesting changes to happen, while larger pores should have a more uniform structure. Also most of selectivity in pores comes from effects based on sizes closer to the molecular level and pore wall interactions. I report the density of water and pore wall elements with their Gibbs dividing surfaces. The H-bond coordination numbers from water-water and water-pore wall interactions, power spectra and angular distributions. Novel surface specific SFG [41] implemented based on VVACF is used to not only gain knowledge about the bonding strength in different pore systems, but also the coordination of those bonding water molecules. In an effort to not only report structure and dynamics separately I report the self-diffusion and the correlation of the angular dipole with the self-diffusion coefficient.

5.2 Computational Details

Unfunctionalized Pore sizes nm	Surface Area nm^2	Effective Diameter nm	Si-OH density nm^2	Functional Group Density nm^2	Hydrophobicity %
0.6	2.70	0.35	8.14	–	–
0.8	3.6	0.41	6.67	–	–
1.0	4.5	0.545	6.67	–	–
1.1	4.95	0.256	4.65	1.81	28
1.3	5.85	0.83	6.83	–	–
1.3	5.85	0.502	4.79	1.88	28.2
1.5	6.75	0.68	4.44	2.37	34.8
1.8	8.1	1.27	6.91	–	–
1.8	8.1	1.03	3.95	2.96	42.8
2.0	9.0	1.35	6.88	–	–
2.15	9.67	1.26	5.37	1.75	23.8

Table 5.1: Data to characterize the theoretical pore models based on the pre-functionalized pore diameter, surface area, Si-OH density, effective diameter, functional group density and hydrophobicity.

An amorphous bulk silica melt structure was created by heating a beta-cristobalite crystalline silica structure containing 648 atoms (216 Si + 432 O) or 1455 atoms (485 Si + 970 O) depending on system size to 4000 K at zero pressure via an NPT-ensemble based Metropolis Monte Carlo (MC) simulation using periodic boundary conditions (PBC). The simulation uses the potential developed by D.M. Tether, and modified and tested by Cormack, Du et al. (TCD) [229] for all atomic interactions. Long-range interactions were calculated using the standard Ewald summation. The simulation reaches equilibrium after 2 million MC-steps. The system's density was 2.31 g/cm^3 at this stage, being very close to P. Gallo's MCM-41 model [230], but higher than fused silica (2.2 g/cm^3) and lower than quartz (2.6 g/cm^3). Experimental data from previous studies reveal an apparent density of 2.37 g/cm^3 for MCM-41 silica. [231] The silica pore was created by removing a cylindrical volume of a specific diameter from the melt structure of size 28.64 Å X 28.64 Å X 14.32 Å and 42.96 Å X 42.96 Å X 14.32 respectively. Free valences on the inner surfaces were saturated via additional hydroxyl groups according to a defined process during which trisilanol groups and isolated oxygens were removed from the surfaces. For the non-pristine system, several of the

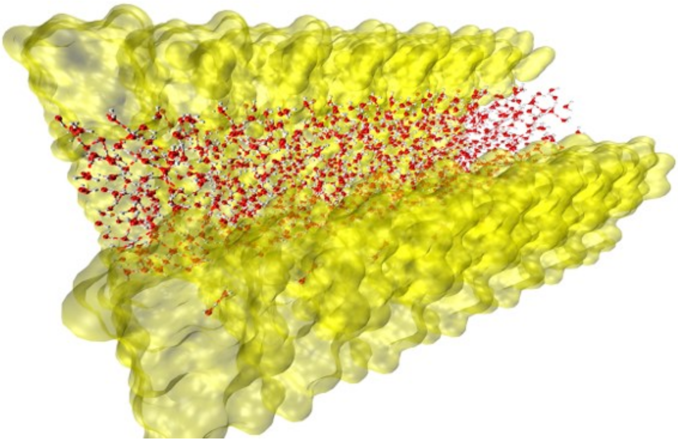

Figure 5-1: Idealized hydrophilic silica oxide pore filled with water. The silica oxide structure is abstracted as yellow, oxygen atoms are red and hydrogen is white. Perdiodic boundary conditions are applied to the systems.

hydroxyl groups were exchanged with trifluoromethyl groups (CF_3), mimicking a more hydrophobic environment using the pore modulation and visualization tool Avogadro. [232] This was done in a way to achieve a decently even distribution of the groups on the surface.

The pore diameters before functionalization can be seen in table 5.1. For the pristine systems they range from 0.6 nm to 2.0 nm in diameter and for the hydrophobic system from 1.1 nm to 2.15 nm. There is no point to have smaller hydrophobic pores as the functional groups are larger and would fill the pore completely. The given surface area of the original pores is given in the table as well for all pore models and the silanol density is calculated based on those values. It can be seen in table 5.1 that most values range between 6.6 and 6.8 silanol per nm^2. The hydrophobic pores have a functional group density which is the CF_3 density. It ranges between 23.4 % and 42.8 % of total possible sites for the functional groups. As such it can be seen that the hydrophobicity of the studied pores increases with pore size.

The systems were equilibrated using the PM6 semiempirical method [233], as implemented with PBC in the CP2K simulation package [234] for 10 ps. Bulk water was generated via CMD simulations using the second-generation Car-Parrinello-based quantum ring polymer contraction method of Kühne and coworkers. [121, 235] Then the water was transferred into the pore system. After inserting the water, the systems were again equilibrated for 10 ps via periodic

PM6 semi-empirical MD [233] calculations [234].The temperature of the system was controlled via a massive CSVR thermostat at 300 K with a time constant of 300 fs. [236] Using a discretized time step of 0.5 fs the total trajectory length of the production run was 100 ps for all systems.

5.3 Results

5.3.1 Pore densities and the Gibbs dividing surface

Actually defining the size of a pore is partly arbitrary. As atoms at the surface are flexible in their positions over time the pore wall position has the form of a probability distribution. Relatively the distribution can be negligible for larger pores, but for nanopores smaller than 2.0 nm the change in pore size can be considerable.

On top there is the issue that most porous systems and pores are not perfectly cylindrical. Even when we model an idealized pore system based on cylindrical shapes the amorphous nature of the material will lead to different surface structures. This one the one hand makes cylindrical pore approximations somewhat more realistic, but on the other hand defining a pore size or diameter becomes more challenging as the diameter changes along the pore axis.

Tools like zeo++ [237, 238] use probes of variable diameters to define characteristic pore properties. The standard probe size is 1.2 Å and the largest included sphere, largest free sphere and largest included free sphere path can be calculated from the geometry file to analyze pore diameters. Other analysis functions include surface area and free volume, relying on a Monte Carlo sampling approach. To reach a characterization of the studied pores the largest included sphere was used as pore diameter and the largest included sphere along the free sphere path was used to estimate the filling of the pore.

The interactions between the pore surface and medium lead to a bonding distance based on pore wall and medium polarity. As such filling the full pore diameter would lead to unrealistically increased water density and would also deform pore walls. This is especially problematic for walls which are functionalized with larger groups that have a wider probability distribution. Many studies use the cylindrical pore diameter based on the cutting of silica bulk to define the pore size and fill the the pore volume with enough water molecules to reach bulk water density. [157, 171, 191] Another way to solve this non trivial problem [239] is performing MD simulations in the Isothermal-Isosurface-Isobaric statistical ensemble [161] or by using a grand canonical monte carlo scheme. [240, 241, 242] This is possible when using classical molecular dynamics but the timescales involved make it infeasible for ab-initio methods in larger systems or when dealing with a large amount of systems.

Figure 5-2 shows the densities of the pristine pore systems from the smallest one at around 0.35 nm of diameter (a) to the largest one at around 1.35 nm (f). All images show the averaged density depending on the radius in nm from the center of the pore. The values for the water density (blue) are as lined out on the y-axis, while the surface hydrogen density (orange) is scaled up to provide reasonable visuals of the surface position distribution.

The pore sizes taken from the largest included sphere diameter from zeo++ [237, 238] are indicated above the diagrams. The zeo++ diffusive line in diagrams shows the diameter that was calculated as the largest included free sphere path, determining the amount of water in the pores. The orange graph shows the surface hydrogen from the different hydroxyl groups. In the hydrophilic pore systems the hydrogen atoms are used to describe the actual pore wall [226]. The other possibility to define the surface would be using the silanol oxygen atoms. [51] On a pristine hydroxylated silica oxide surface there are so called in plane and out of plane silanols. The in-plane silanols are bound to other hydroxyls, orienting them further away from the surface than hydroxyls that are out of plane. Of course because of its amorphous character the pore is not perfectly cylindrical, which adds more variance in hydrogen position based on local geometry.

This can be observed in Figure 5-2 as well. For example in pore d), e) and f). It can be seen that there is a main hydrogen peak and a shoulder towards the surface. The shoulder can be attributed to out of plane silanol groups, while the main peak would be attributed to in-plane silanol groups. This also means that for those systems there are more in-plane silanol groups than out-of-plane ones. This could be important when interpreting how water molecules are binding at the surface. A different picture can be seen in system c) as there is no shoulder present towards the water surface. System b) on the other hand shows a small shoulder and looks more similar to the larger pore systems.

As can be seen for the smallest pore systems (a+b) the water densities diverge strongly from expected bulk values around 1.0 g/cm^3. The definition of pore size and wall geometry is most arbitrary in the smallest pores, as the width of the pore wall distribution makes up a large part of the total pore. This leads to large changes in diffusive diameter and pore volume as percentage of its total pore diameter and volume.

It can be seen that for the smallest pore a), single file water actually leads to a water density up to 2.0 g/cm^3, way higher than bulk water, while the density is never higher than 0.6 g/cm^3 in pore b). This strongly shows that for very small nanopores filled by single file water, small changes in pore size lead to dramatic changes in water density and structure. This happens because in the larger pore b) there is more free volume than in the smallest one a) but not enough to accommodate more than a single file of water.

When using the Gibbs dividing surface formalism we get two lines for water and hydrogen that can be used to estimate the surface position and the distance between those two surfaces. In the pristine cases I indicate a Gibbs dividing surface for the water and hydrogen, while there is another flour surface in the hydrophobic cases. For the smallest pore a calculation of the Gibbs dividing surface is omitted because of the resolution and the arbitrariness of the pore wall location. Generally the larger the pores the better does the zeo++ diffusive distance agree with the Gibbs dividing surface for water calculated from the whole trajectory. This underlines the difficulties to determine pore sizes $<$ 0.8 nm but also shows that the algorithms work reasonably well for pristine pores up to that size.

For pore b) the distance between the two surfaces is very small with around 0.025 nm, but it increases with every pore size to 0.110 nm for the largest pore. The notable exception to this is pore c). Here the distance is the largest of all studied pristine cases. For this pore size the water structure is also special, as it is very structured with just one peak, indicating a single file like water structure in the pore. It is the largest studied pore showing such a structure. This deviates considerably from the next larger pore d) that shows two water layers and pores e) and f), that show a decrease in structure towards a more even bulk like ordering.

This shows that the structure of water decreases over pore size, and distance

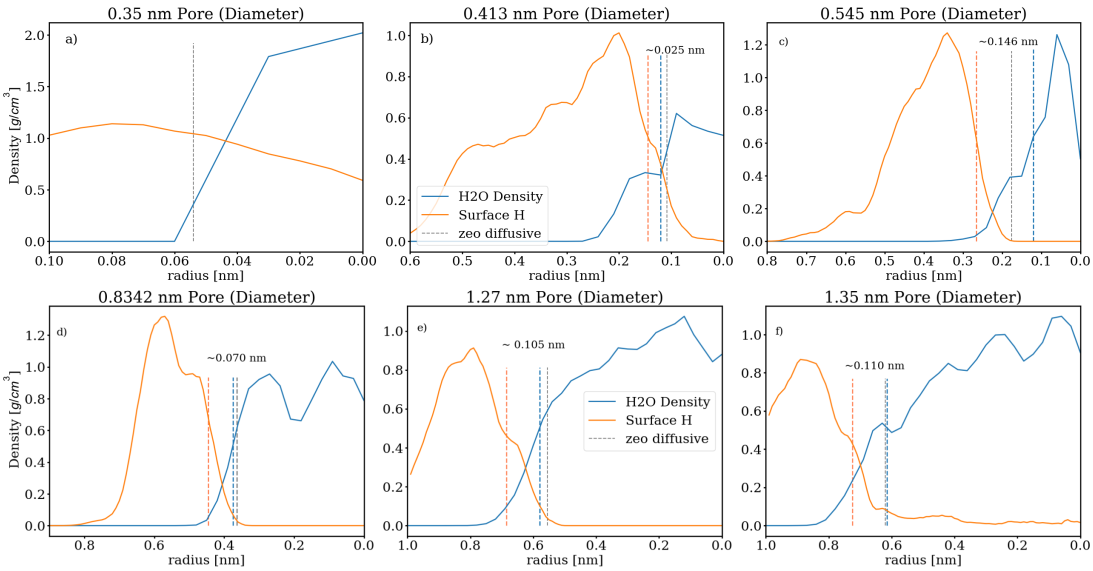

Figure 5-2: The radial density of water (blue) and functional wall element hydrogen (orange) for the pristine pores from the smallest pore system (a) to the largest one (f). The density is shown from the pore surface towards the center of the pore.

between the surfaces generally increases. Over different nanopore sizes various different structures are in existence. This makes nanopore a very interesting topic of research. Larger pores just inhibit an increasing amount of bulk water in the center [191] and a constant surface region, while pores in this study very much see a change in nature of their structure as most of the pore medium can be considered as surface region.

For the hydrophobic CF_3 systems the flour atoms are used to visualize the pore surface. The prevalence is shown in green and added on top of all information already known from the pristine hydrophilic systems. It can be observed in figure 5-3 and figure 5-4 that the flour atoms are dominant in defining the pore wall. The positions of flour atoms are closer to the surface, diminishing the effect pristine silanol can have. Contrary to silanols which have the ability to be in plane or out of plane because of their inter-bonding, flour only has one major peak with a relatively equal distribution. This also underlines that the shoulders and secondary peaks of pristine systems are mainly based on in-plane, out of plane dynamics and not other geometric differences.

The water in the hydrophobic pore b) seen in figure 5-3 is structured with one main layer and a shoulder towards the surface. The distance between the two

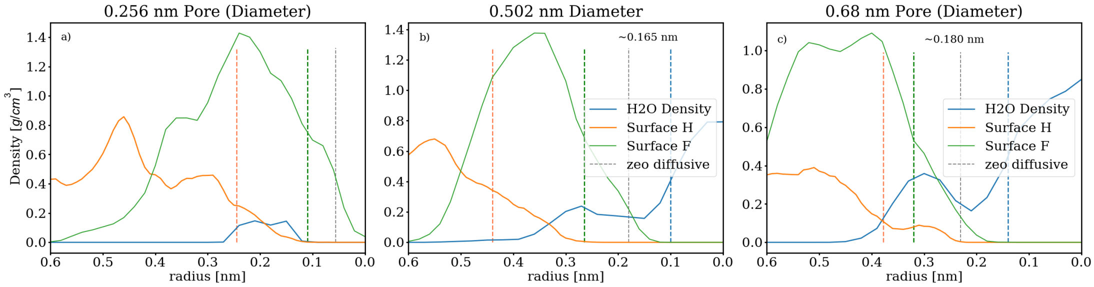

Figure 5-3: The radial density of water (blue) and functional wall elements flour (green) and hydrogen (orange) for the hydrophobic pores from the smallest pore system a) to c). The density is shown from the pore surface towards the center of the pore.

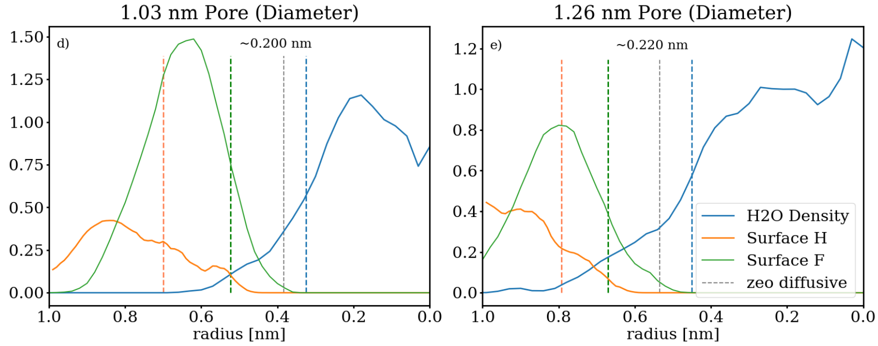

Figure 5-4: The radial density of water (blue) and functional wall elements flour (green) and hydrogen (orange) for the hydrophobic pores for the pore system d) and e). The density is shown from the pore surface towards the center of the pore.

Gibbs dividing surfaces is generally larger than in the pristine systems. In fact the distance in the pristine pore of similar size was around 0.025 nm, while it is around 0.165 nm in the hydrophobic pore. The Gibbs dividing surface distance increases for every hydrophobic pore until it reaches 0.220 nm for the 1.26 nm pore. This is double the Gibbs distance of the largest hydrophilic pore system.

As the strength of interactions between the medium and the pore wall is very much dependent on the distance we can expect fewer strong interactions. This is what we would generally expect from a hydrophobic material. The water also appears slightly less structured in hydrophobic systems. Peaks are not as spiky as for example in the hydrophilic pore system c) and the slope of the water system is different. This can be seen in Figure 5-4 for d) and e) especially. The slope of the water is increasing as in a quadratic function, increasing first slowly, then faster. In the hydrophilic system water density increases steeply until reaching

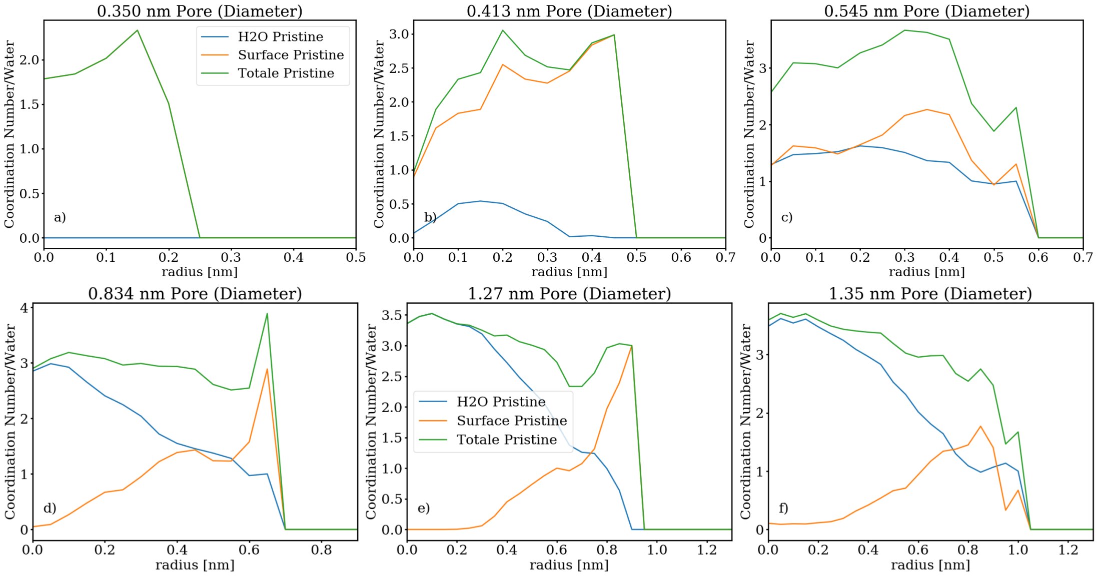

Figure 5-5: The H-Bond coordination number from water-water (blue), water-pore wall silanol (orange) and the sum (green) of interactions vs the radial distance from the center of the hydrophilic nanopores.

asymptotic behavior. This is of course directly correlated to the larger distance of the surfaces.

5.3.2 H-Bond coordination numbers

The different surface structures, water structures and especially the larger distance between the Gibbs surfaces should also be represented when looking at the number of H-bonds that are formed.

As hydrogen bonding plays a big role in the structure and dynamics inside the pore, we want to understand this process better. Studies have shown, that the coordination number reaches its maximum at around 5 Å distance from the surface and generally studies [191, 223, 171] report a loss of coordination at the surface of hydrophilic pores.

I calculated the hydrogen-bond coordination number across the pore based on rOO $<$ 3.55 Å and (O2; O1, H1) $<$ pi/6, which is a common definition. [159, 243] I also included the coordination numbers of the water molecules with the hydroxyl and trifluoromethyl groups in our systems using rCO $<$3.65 Å and (C2; O1, H1) $<$ pi/6. This change corrects for the larger C-F bond length.

The pristine pore systems of all sizes are shown in figure 5-5. The smallest pore a) has only coordination with the pore walls as there is not enough water for water-water coordination. The maximum of coordination is low (just over 2.0) which shows strong undercoordiantion compared to reports of bulk coordination.

As can be seen for pore b) the coordination has a maximum of 3.0, considerably lower than coordination in bulk water. [244] or reported by Allolio et al. in larger nanopores via ab-initio methods. [171] It is also obvious that by far the biggest amount of coordination is based on silanol-water interactions. Water-water bonding contributes only a very small amount and nothing at the very interface.

For the second smallest pore c), part of the coordination comes from water-water hydrogen bonding, but this is decreasing towards the pore walls and slightly more coordination is provided by the interactions with the silanol groups. But generally coordination with the water is of similar magnitude as coordination with silanols. The total coordination number is very similar to the coordination in pore b), just the distribution is coordination is changed.

Pore d) also shown in figure 5-5 has a more typical behavior. This again underlines the exceptional structures that exist in pores smaller than 0.5 nm. In pore d) the coordination number of water decreases constantly from 3.0 at the center of the pore to the surface, while the water-silanol coordination (orange) increases constantly. A strong peak in coordination can be seen directly at the surface where only very few water molecules are present. This peak is interesting but should not be overstated. It is likely that those water molecules very close to the surface located in the peak are interacting with in-plane silanols and are H-bond donors.

A similar pattern can be seen in pore e), but with a higher coordination maximum of around 3.5 H-bonds at the center of the pore. This indicates that we would see even higher maxima in larger pores. Apart from this difference the behavior of water coordination in e) is very similar to that in d). For the largest pore f) the total coordination does not have a peak at the interface, but shows a constant decline. As can be seen this is because water-silanol coordination does decline and does only reach a peak of around 2.0.

Comparing the results with those for the hydrophobic systems in figure 5-6

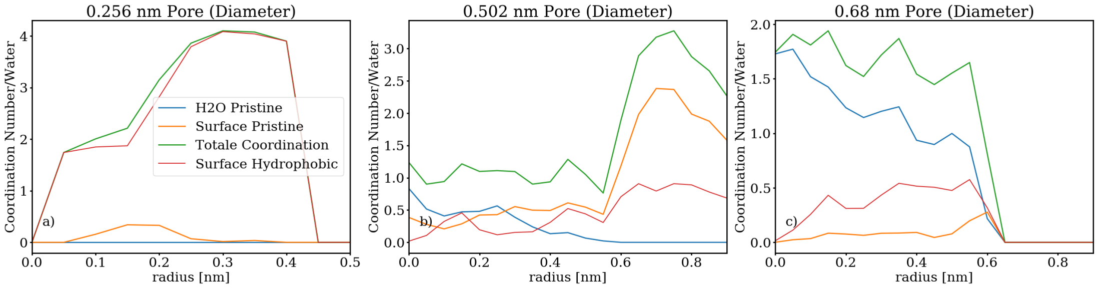

Figure 5-6: The H-Bond coordination number from water-water (blue), water-pore hydroxyl (orange), water-TFM (red) and the sum (green) of coordination vs the radial distance from the center of the hydrophobic nanopores a) to c).

and figure 5-7 stark differences become apparent. For the smallest system a) the coordination number reaches over 4.0, the largest value of all systems yet. This is based nearly only on water-TFM coordination (red). The high agrees well with the high densities reported in section 5.3.1. Similarly the density of hydrophobic pore b) was relatively low and this can also be seen in the coordination number of b). It is mostly lower than 1.5 and only shows a peak up to 3.0 at the interface. This peak might be due to small amounts of water very close to the surface because of variations in pore geometry. It is a special case as most of its coordination is based on water-silanol interactions. This is not the case for any other hydrophobic pore system in this study.

The hydrophobic pore c) on the other hand is a bit larger and shows a more typical behavior. Total coordination is decreasing towards the surface with a maximum of around only 2.0, by far less than in hydrophilic pores of similar sizes. Most of the coordination comes from water-TFM (red) and some from water-silanol (orange) interactions. The coordination from the surface is slightly increasing but compared to the studied hydrophilic pores in figure 5-5 it is only happening slowly and not showing a strong peak directly at the surface.

The two largest hydrophobic systems d) and e) are shown in figure 5-7. The total maximum coordination with 3.0 to 3.5 at the pore center is very similar to the hydrophilic cases of similar pore size. Similarly water coordination decreases quickly towards the surface. As compared to hydrophilic pores here water-silanol coordination is nearly non-existent, which supports that the surface in the hydrophobic pores is made up by TFM, as silanol loses its importance in determining the structure inside the pores.

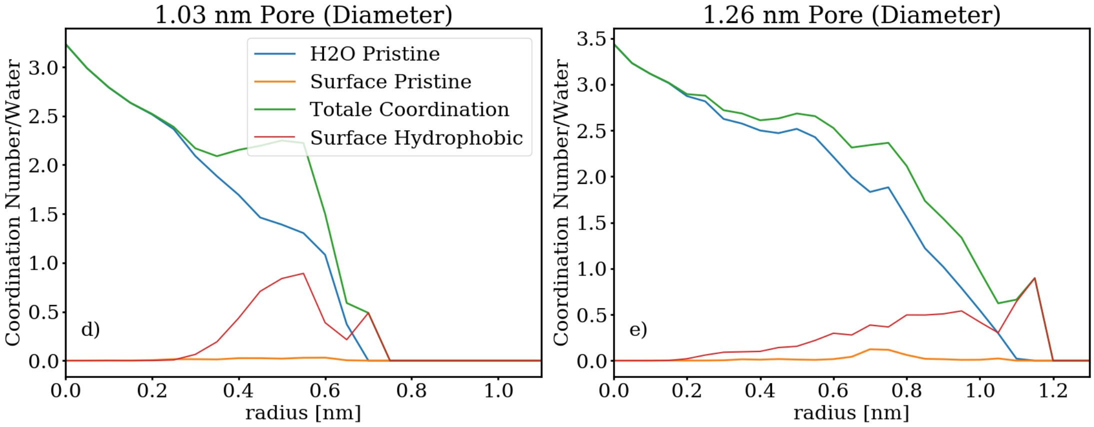

Figure 5-7: The H-Bond coordination number from water-water (blue), water-pore hydroxyl (orange), water-TFM (red) and the sum (green) of coordination vs the radial distance from the center of the hydrophobic nanopores d) and e).

The maximum of coordination from water-TFM is also much lower than those from silanol at the surface of hydrophilic pores. While we reported up to 3.0 H-bonds per water from silanols at the surface the coordination of TFM has a maximum of 1.0. The relatively low coordination number at the pore center could also play a large role in the dynamics inside the pores.

5.3.3 Diffusion coefficients by MSD calculations

The diffusion in pore systems is not only important for selectivity and permeability in membranes but also for most processes and reactions, as those include diffusion of educts to the reaction site and diffusion of products away. Often those processes limit the reaction. There are two common ways to calculate the diffusion from molecular simulations. Either via the integral of the velocity-velocity auto-correlation function and Green-Kubo equation [245, 246] or via the mean square displacement (MSD) and the einstein relation. [247, 248]

Here the MSD is calculated using a correlation length of 10 ps with a 0.5 ps shift of the correlation window, considering 90 ps of the trajectory length as correlation starting points. The diffusion coefficient is then calculated from the 5 ps tail end of the correlation window.

Here I used the MSD to calculate the diffusion coefficients of water in the hydrophilic (pristine) and hydrophobic (trifluoromethyl) pores. The results can be seen in table 5.2 and in figure 5-8 and figure 5-9. The diffusion of water in

Pore model	Effective Diameter nm	Diffusion Coefficient $m^2/s \times 10^{-9}$
0.6 Pristine (a)	0.348	0.034
0.8 Pristine (b)	0.413	0.426
1.0 Pristine (c)	0.545	0.18
1.1 Hydrophobic (a)	0.256	—
1.3 Pristine (d)	0.834	0.64
1.3 Hydrophobic (b)	0.505	0.777
1.5 Hydrophobic (c)	0.677	2.43
1.8 Pristine (e)	1.272	2.12
1.8 Hydrophobic (d)	1.03	3.92
2.0 Pristine (f)	1.357	1.75
2.15 Hydrophobic (e)	1.26	2.89
Bulk PM6-FM	–	2.39

Table 5.2: Diffusion calculation for all pore systems by mean square displacement from a trajectory of 100 ps. The correlation length was calculated as 20000 steps with the diffusion coefficient calculated from the lat 10000 steps of the correlation length to exclude Brownian motions.

bulk is reported as $2.299 \times 10^{-9} m^2/s$ [249]. The reported bulk diffusion for water calculated by the force matched PM6-FM semi-empirical method by Welborn et al. [17] is $2.39 \times 10^{-9} m^2/s$. It also has to be considered that in small periodic cells diffusion calculated by molecular dynamics will be lower because of the finite box size, but corrections are difficult to apply to systems in my study. [250, 251]

Compared to bulk diffusion coefficients the diffusion is slower in most of the hydrophilic nanopores studied. This can be called subdiffusive. The diffusion is slowest in the smallest pristine pore a) with an effective diameter of 0.348 nm. It then increases more than tenfold in the 0.413 nm pore b). The smallest pore a) is very sub-diffusive as the geometry strongly hinders permeability. Even though the water density in pore b) is smaller than in bulk, diffusion is much slower at $0.426 \times 10^{-9} m^2/s$. As can be seen in figure 5-2 both pores a) and b) are filled with a single line of water, but b) has a larger diameter. The 0.54 nm pore c) has lower diffusion ($0.18 \times 10^{-9} m^2/s$) than the 0.41 nm large pore b). Contrary to this we would generally expect that diffusion increases with diameter as several studies reported this correlation, based on the impact of surface area to bulk ratio decreasing. [158, 226] But this is not true for pores of very small sizes as all of the water can still be viewed as surface region water (less than 5 Å distance from

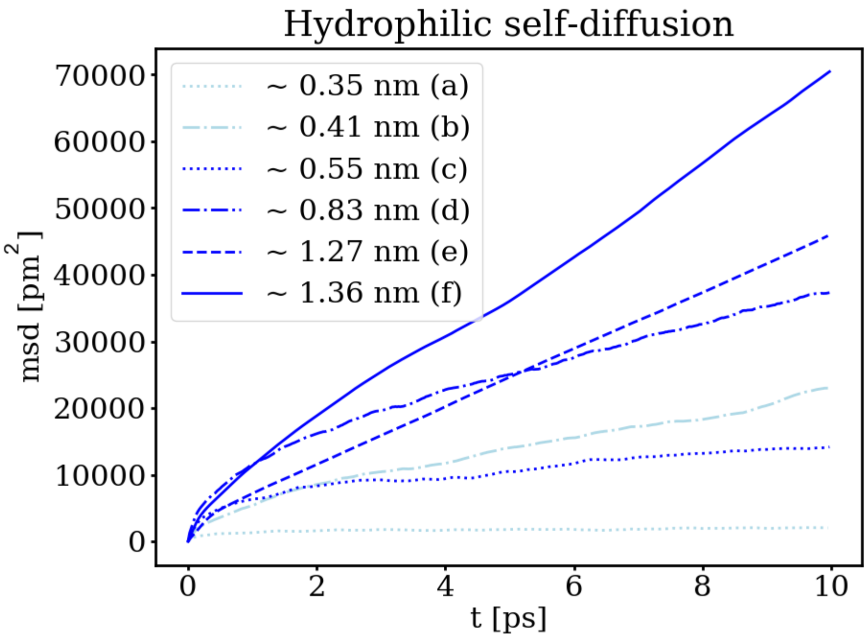

Figure 5-8: The mean square displacement of hydrophilic pores a) to f) is shown over a correlation length of 10 ps

interface [171]). This is underlined by the strong water structure seen in figure 5-2 and an oversupply of out of plane silanols that form hydrogen bonds with the water. This can also be seen in figure 5-5 where pore c) shows coordination mainly from water-pore wall interactions instead of water-water interactions.

For larger pores the diffusion increases constantly up to the fastest one for the 1.272 nm pore at $2.12 \times 10^{-9} m^2/s$ and $1.75 \times 10^{-9} m^2/s$ for the 1.36 nm pore. It is still slower than diffusion in bulk water but as others have reported the water diffusion is expected to keep increasing with pore size until it reaches close to bulk water diffusion properties. [158, 226]

The hydrophobic pores were studied in the same way. It is shown in figure 5-9 that water diffusion in hydrophobic pores mostly accelerates with increase in pore size. The smallest hydrophobic pore at 0.256 nm shows no diffusion other than brownian motions. As such we can determine that this pore size is too small for diffusive behavior. The second smallest hydrophobic pore b) from figure 5-3 has a diffusion coefficient of $0.78 \times 10^{-9} m^2/s$. This puts it close to the diffusion in the much larger pristine pore d) with 0.834 nm diameter. To the same tune the diffusion in the 0.677 nm hydrophobic pore is also close to 4 times faster than the diffusion in the similar sized hydrophilic pore d) we just discussed. A similar

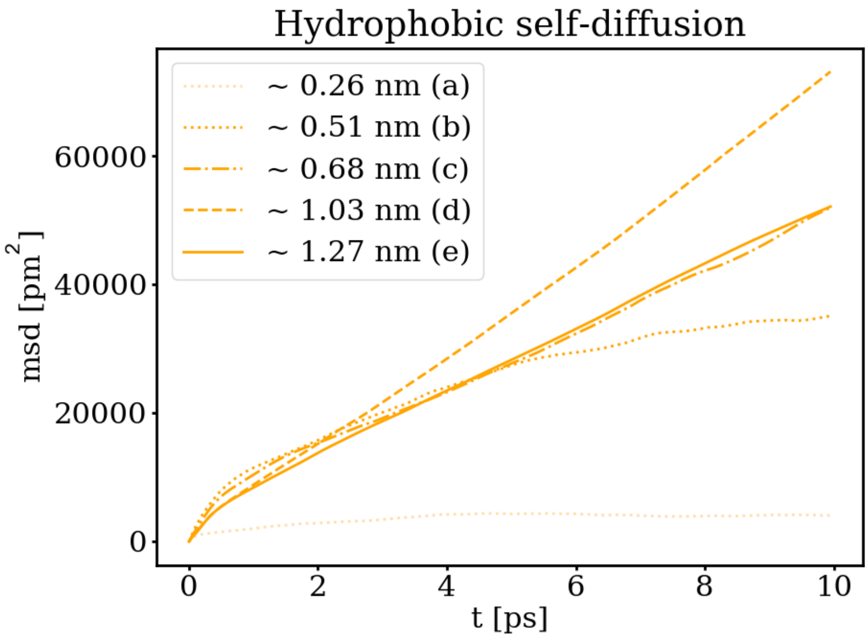

Figure 5-9: The mean square displacement of hydrophobic pores is shown over a correlation length of 10 ps for pores a) to e).

contrast can be seen in figure 5-10 as the 1.03 nm hydrophobic pore is close to 2 times faster than the larger hydrophilic pore. This pore size actually has the fastest diffusion of all studied systems at $3.92 \times 10^{-9} m^2/s$, much faster than any hydrophilic pore, calculated bulk water diffusion and experimental bulk water diffusion. This pore setup can be classified as being superdiffusive. This might partly be based on the reported low coordination number of only 3.0 at the pore center in hydrophobic pore d).

It is also faster than diffusion in the largest studied hydrophobic system with pore diameter of 1.26 nm, showing that small changes in size and structure lead to very different dynamics inside nanopores. This also generally shows that the functionalization of the pore wall and the resulting polarity have a strong influence on the diffusion in nanopores of sizes < 2 nm.

5.3.4 Radial diffusion calculated by MSD

To supplement the diffusion we look at the radial diffusion in the pores. Most studies reported a slow down for water in hydrophilic pores towards the surface [226, 171, 252, 227, 223], while Renou et al. [158] found the opposite effect in some functionalized cases. Here we also find that diffusion generally decreases

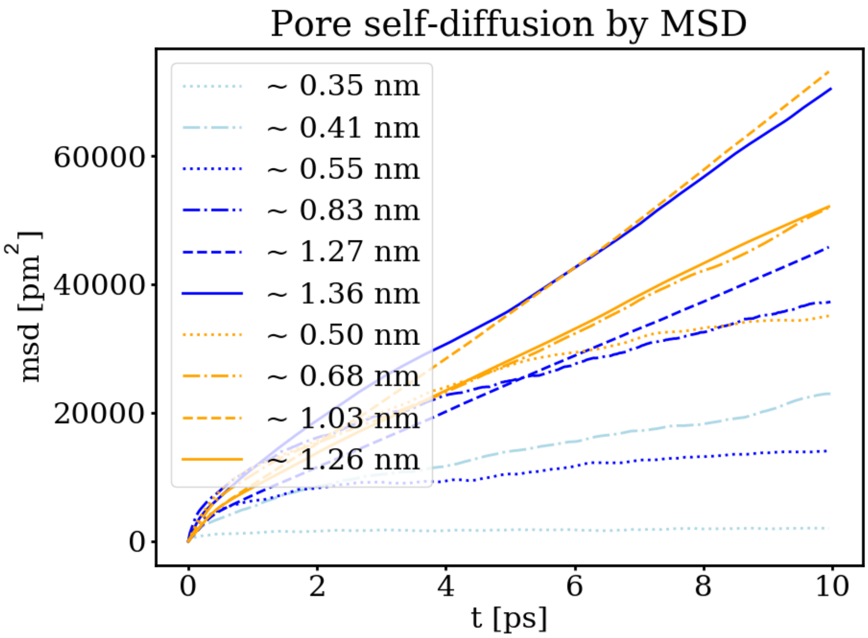

Figure 5-10: The mean square displacement for all hydrophilic and hydrophobic pores over a correlation length of 10 ps of correlation length to compare diffusion based on hydrophobicity.

towards the pore walls. In figure 5-11 the diffusion for all hydrophilic pores can be seen in blue. It was calculated using the mean square displacement similar to how we used it before, but for different radial intervals.

For very small pores the fastest water is slightly shifted from the center of the pore. But all other pores show a very strong decrease in diffusion from the pore center to the pore walls looking at the normalized values.

For the hydrophobic systems in figure 5-12 the behavior is very similar to the hydrophilic one, except for the smallest systems that have shown very different structure and dynamics. As we have reported in section 5.3.3 the overall diffusion is faster in hydrophobic pores. But the radial diffusion shows that this is not based on only water at the surface diffusing faster but on a higher diffusion of all water molecules in the pore overall, especially those in the pore center. This underlines the importance of the water-water bond network in analyzing the water dynamics inside pores. For this the coordiantion number can be taken into account. One observable feature in the largest hydrophobic pore e) in figure 5-12 is the water water slightly outside of the center of the pore is relatively fast, meaning diffusion does not decrease as quickly when moving from pore center to the wall. This is similar to the behavior of water in the hydrophobic pore c) and the smaller pore

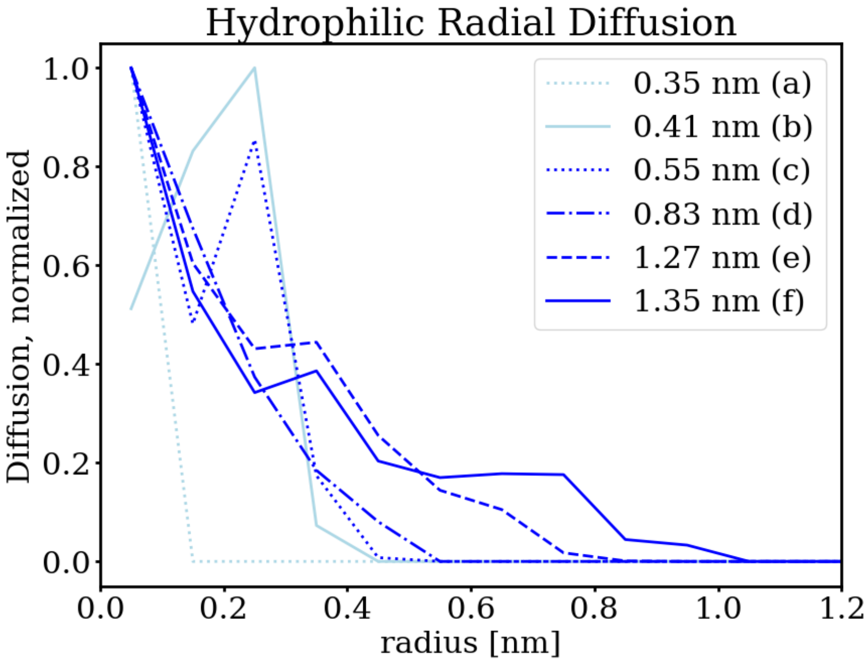

Figure 5-11: The self-diffusion coefficient of water in hydrophilic pores of different sizes vs the radius of the pore from the pore center to the pore walls.

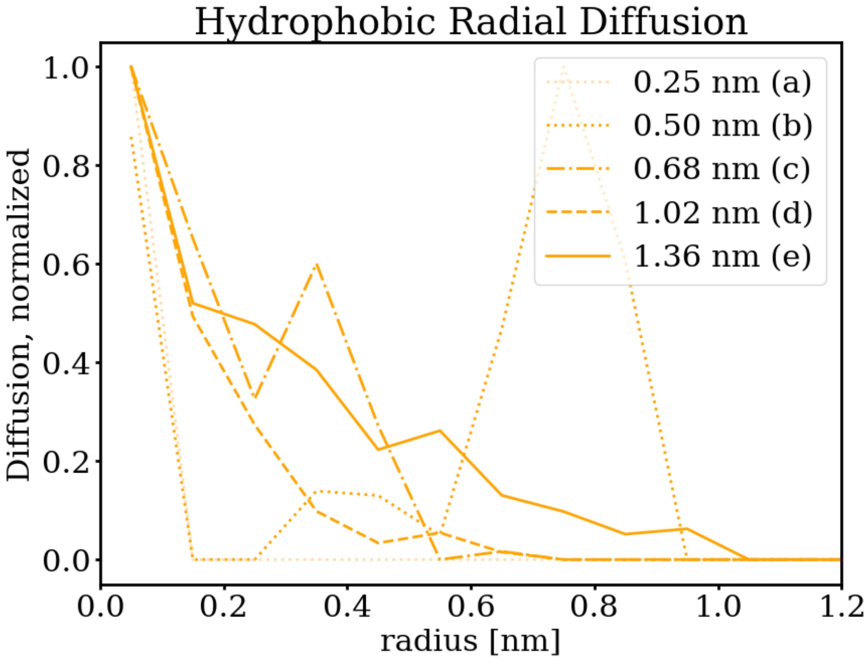

Figure 5-12: The radial self-diffusion coefficient of water in hydrophobic pores of different sizes vs the radius of the pore from the pore center to the pore walls.

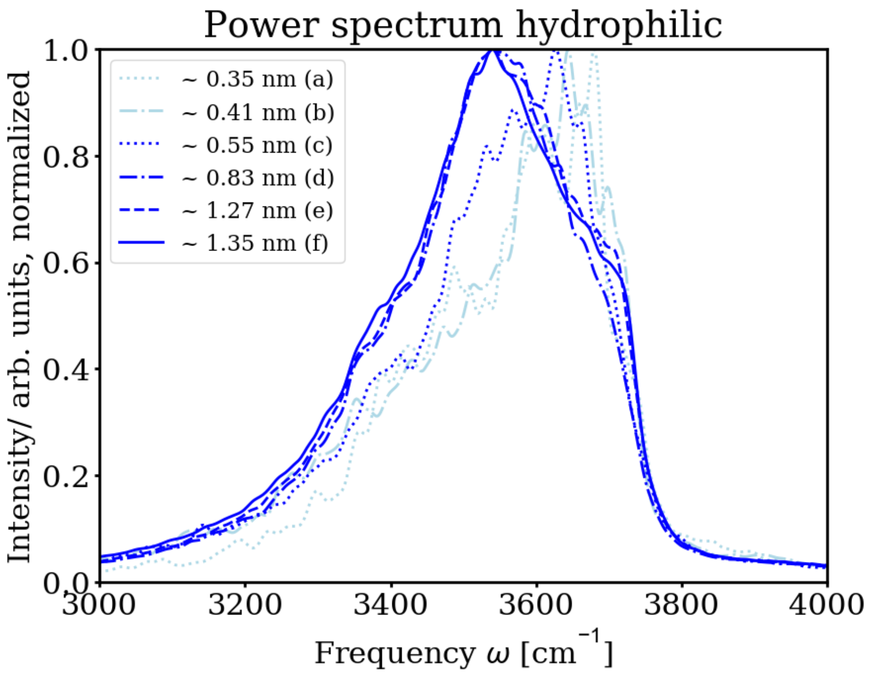

Figure 5-13: Power spectrum of water in hydrophilic pore systems between 3000 cm^{-1} and 4000 cm^{-1} calculated by Travis [253]

c) in the hydrophilic case. As the hydrophobic pore c) already shows relatively high diffusion for its size, it is an interesting observation that might partly explain the higher overall diffusion.

5.3.5 Power spectra of water inside nanopores

One way to analyze the structure of water inside pores is using the power spectrum. Here we calculate the power spectrum using the program travis analyzing all water in a pore system. [253, 254] The power spectra for the hydrophilic pore systems from 0.35 to 1.35 nm are shown in figure 5-13. It can be seen that the smaller pores have a predominant peak at 3700 cm^{-1} . For larger pores starting with the 0.83 nm one the main peak is located at a lower frequency at around 3500 cm^{-1} and the main peak of smaller pores is only visible as a high shoulder. But that shoulder around 3700 cm^{-1} increases slightly from pore d) to f). This would indicate slightly more "free" or dangling bonds but overall more strongly bond water inside the pores. Those frequencies around 3500 cm^{-1} are commonly attributed to "liquid" like interactions.

I have done the same calculation for water in the five hydrophobic systems

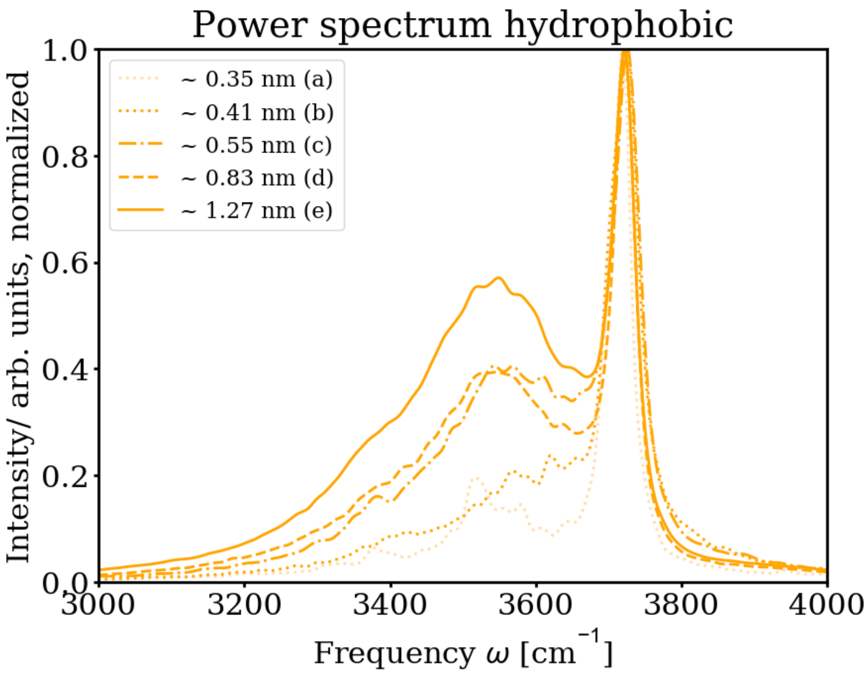

Figure 5-14: Power spectrum of water in hydrophobic pore systems between 3000 cm^{-1} and 4000 cm^{-1} calculated by Travis [253]

from 0.35 nm to 1.27 nm. The normalized results are shown in orange in figure 5-14. It can be seen that all of the systems have a very pronounced main peak at high frequency, representing more loosely or "free" dangling bonds. It is the dominant peak in the hydrophobic systems at around 3720 cm^{-1} in contrast to the liquid peak being most dominant in the hydrophilic systems at around 3500 cm^{-1}. The hydrophobic systems also have the same peak, but its relative prevalence is lower. When increasing the pore size this peak interestingly increases, as does the shoulder towards 3200 cm^{-1} to 3300 cm^{-1} indicating more strongly bonded water, regularly called "ice" like. This means more strongly bonded water relative to weakly bonded water exists in larger hydrophobic pores. But power spectra are not surface sensitive. So we do not know how the spectrum at the surface looks and whether more strongly bonded water is interacting with the surface or other water molecules.

5.3.6 Surface-specific SFG spectra inside nanopores

To analyze the differences in structure at the interface of pore systems we use surface specific Sum Frequency Generation (SFG) spectra calculated from the

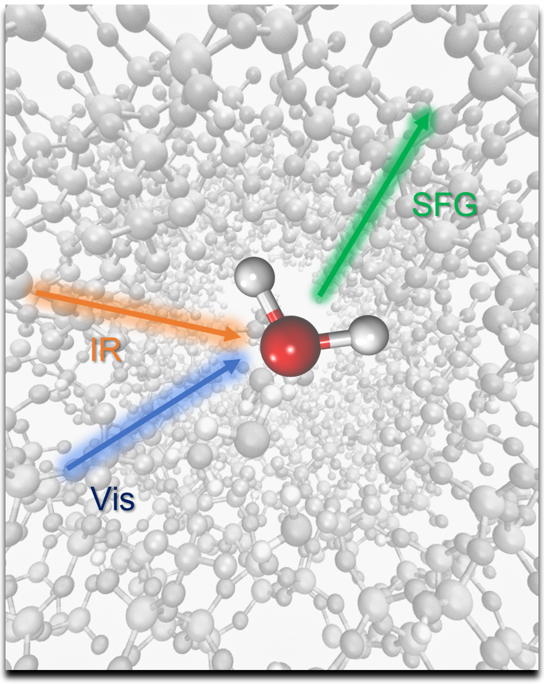

Figure 5-15: SFG is using infrared (IR) and visible (VIS) light to produce the SFG response in a molecular pore system.

velocity-velocity auto-correlation function. The method developed by Otho et al. [41] was adapted to a pore setup.

As SFG is sensitive to the orientation of O-H stretches relative to the surface we can gain knowledge about the dominant frequencies, the corresponding bonding strength and the orientation of such bonds. Generally higher frequencies mean O-H stretches are more weakly bonded, while lower frequencies mean they are more strongly bonded. In the imaginary response shown in table 5-1 positive intensities are the result of overrepresentation of O-H stretches pointing towards the surface and negative intensities of O-H stretches pointing away from the surface towards other water molecules. This SFG spectra calculation method is exploiting the asymmetry of interfacial systems. In bulk the response of the SFG vanishes because of symmetry which makes it surface specific.

It is shown in figure 5-1 that the 0.348 nm hydrophilic (pristine) pore has its main peak at 3680 cm^{-1} and a wide shoulder with peaks from 3600 cm^{-1} to 3300 cm^{-1}. This indicates that the water at the surface (which is all the water in the single file pore) is strongly bounded. Of all pore systems it has the biggest ratio of area in low frequency regions. The fact that it is negative is a lesser concern for the smallest system a), as the orientation is kinda arbitrary for pores where very few water molecules exist very much in the center of the pore.

Comparably for the slightly larger pore b) the strongly bonded frequencies are less pronounced. This means there are less strongly bonded water molecules at the surface, pointing towards the surface, while the weakly bounded parts are dominating the spectra with the dominant peak at 3700 cm^{-1} . This aligns well with diffusion calculations presented in the chapter before that showed faster diffusion in b) than in the smallest pore a). This difference could be based on less strongly bonded water molecules in the surface region.

The 0.545 nm pore c) shows similarly weakly bounded water stretches pointing downwards, but those are well underrepresented compared to before. The main peak around 3650cm^{-1} is pointing upwards and such shows bounding with the surface, not with other water molecules. Whether those are "free" or "liquid" water molecules is still debated. [84] Strong Interactions with the surface are believed to be disadvantageous for fast diffusion through the pore. There are also strongly bounded O-H stretches around 3300 cm^{-1} to 3500 cm^{-1} which are pointing away from the surface, interacting with other water molecules.

This would seem to agree with previous studies [51, 134] attributing the lower frequencies, stronger interactions to "ice" like water that is accepting an H-bond from out of plane silanols. The orientation of O-H stretches away from the surface in that region fits that explanation. Similarly an intense "liquid" like peak pointing towards the surface would be attributed to water donating a H-bond to in-plane silanols. Including the known phenomena of "free" or dangling bonds the last peak at around 3720cm^{-1} is explained as water pointing away from the surface, that does act as a H-bond acceptor.

The calculated diffusion for this pore was especially slow even though the distance between the Gibbs surfaces was not especially small and coordination not especially large. But coordination was mainly happening with the surface and not with other water molecules. The comparison with pore system b) especially supports the idea that diffusion will be faster the more the spectrum is blue shifted to higher frequencies.

For the three larger pores from 0.83 nm to 1.35 nm the spectra is mostly

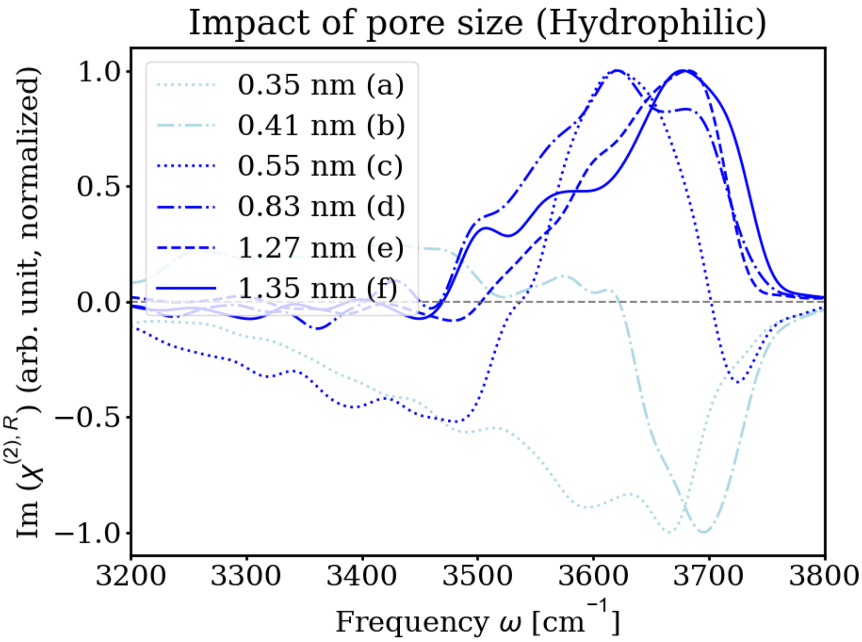

Figure 5-16: Imaginary SFG response for the hydrophilic systems functionalized with trifluoromethyl for sizes of 0.35 nm to 1.36 nm. The intensities are normalized for comparability. The frequencies are scaled by 0.957 to correct for known errors. [17]

positive. While the 0.83 nm pore has multiple peaks, the more "liquid" like peaks change into mere shoulders of the "free" positive peak at around 3680 cm^{-1}. This means the main overrepresentation are O-H stretches pointing towards the surface, but those are less and less strongly bonded with larger pore diameter. The "ice" like peak is non existent for the larger pore sizes and peaks from 3550 cm^{-1} to 3620 cm^{-1} are diminished. That does not automatically mean no bonding like this exists, but that this coordination is not more likely than its complete opposite. That does not mean at all that water-water coordination is low as was seen in section 5.3.2.

This fits in well with our calculated diffusion coefficients also increasing towards larger pore sizes. It is important to note that the absence of negative frequencies indicates that water to water interactions are overshadowed by water-surface interactions. In other words: In the competition between pore wall-water and water-water interactions the pore wall interactions win out in hydrophilic pores.

It is obvious that most hydrophilic systems and all of the larger ones show a "free" band at around 3680 cm^{-1}. This was also found by Dalstein et al. [208]

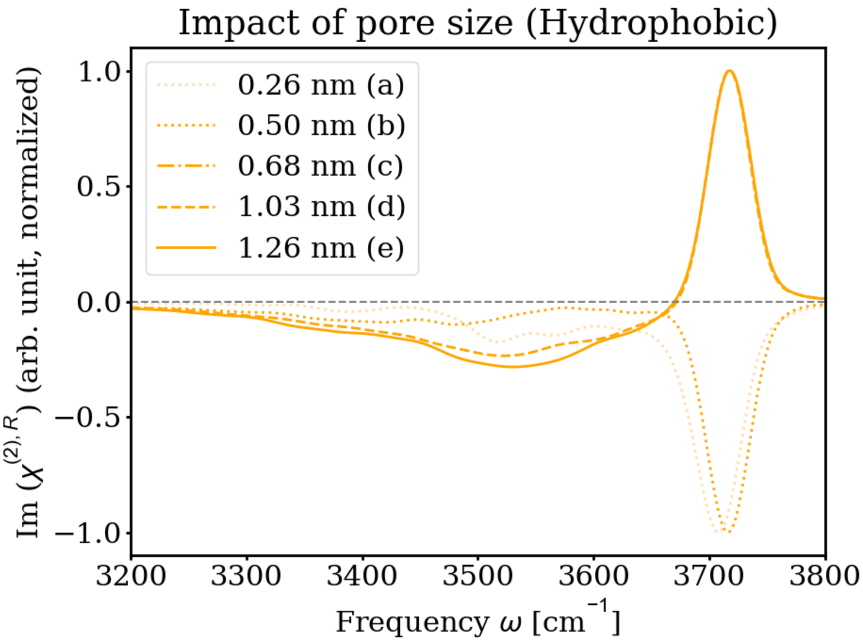

Figure 5-17: Imaginary SFG response for the hydrophobic systems functionalized with trifluoromethyl for sizes of 0.26 nm to 1.26 nm. The intensities are normalized for comparability. The frequencies are scaled by 0.957 to correct for known errors. [17]

and Backus et al. [255], who correctly attributed it to O-H stretches pointing towards the surface. We can also see that this band only becomes predominant with increasing pore size and that this structural phenomenon cannot be studied using for example power spectra.

The SFG response for the hydrophobic pore systems from 0.26 nm a) to 1.26 nm e) can be seen in figure 5-17. The smallest pore mostly shows a "free" peak at around 3720 cm^{-1}. It is slightly blueshifted compared to the "free" peak observed in most hydrophilic systems (figure 5-1). The band is negative in this case, but this is based on the very small pore size and does not provide extra information. Generally the hydrophobic pores don't show as much change with increasing pore size as the hydrophilic systems have. But it is observable that the "liquid" like bands between 3400 cm^{-1} and 3600 cm^{-1} do increase in relative prevalence.

For the largest 1.26 nm pore e) the response is not too different to reported results at the water/air interface. [96, 45, 41, 1] This can be interpreted as water being very weakly bonded or free towards the surface, but interacting with the other water molecules in the pore more strongly in a "liquid" like manner. Here one view would be that the water-water interactions won out in the competition

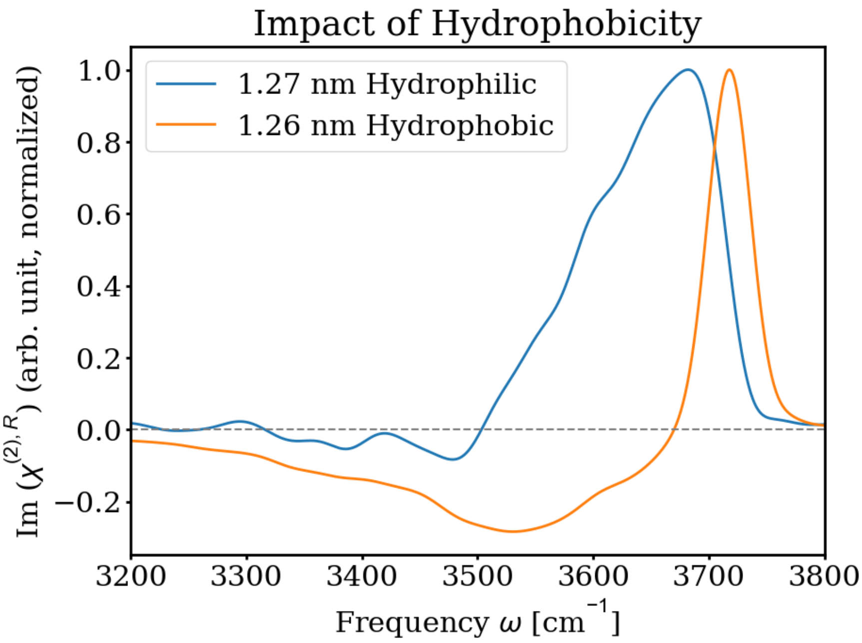

Figure 5-18: Imaginary SFG response of the 1.27 nm hydrophilic system (blue) vs the 1.26 nm hydrophobic (orange) one. The frequencies are scaled by 0.957 to correct for known errors. [17]

between water-water and water-surface interactions.

When comparing a hydrophilic and hydrophobic pore of similar size in figure 5-18 the differences are easy to see. All pores have a "free" or dangling peak, but it is slightly blueshifted in the hydrophobic pore. There also is a wide shoulder starting from 3500 cm^{-1} indicating a "liquid" like peak, but no "ice" like peak can be observed. Tang et al [84] discussed the existence of another "free" like peak at around 3600 cm^{-1}. There is a response at this band and a small peak can be seen. All of those O-H stretches responsible for the bands are pointing towards the surface, indicating that water is bonding with the surface. Comparably the hydrophobic surface has a response in the 3300 cm^{-1} to 3650 cm^{-1} region pointing towards other water molecules. So there is an argument that a small amount of "ice" like water is present at the surface. Generally water is more weakly bonded with the surface and more strongly bonded with other water molecules.

5.3.7 Angular distribution and diffusion based on the dipole angle

So far the results presenting the structure and dynamics are interesting and have not been done in one comprehensive study. But here we add the angular distribution of water at the surface of all studied systems and the self-diffusion coefficient of those angular configurations. Both values are normalized with the highest self-diffusion coefficient and the prevalence, as a value of one means its the most prevalent state and all other values are ratios of that state. A value of 0.5 means the value is 50 % of the maximum value. As such we can study the dipole angle relative to the surface of the pore. A dipole angle of 0° means water is pointing towards the surface, while an angle of 180° means water is pointing away from it. In the figures 5-19, 5-20 and 5-21 the distribution over those angles can be seen.

As such we can first determine the most common dipole angles (water orientations) and their diffusion speeds. The blue arrows are an abstract depiction of the relative diffusion strength of that particular orientation compared to the average of said system. The length of the vector can not be used to judge the diffusion coefficient between different systems. For this we have a look at section 5.3.3 or at section 5.3.4 for the information along the pore radius.

The most common orientations are depicted above or below the figures for each pore size and functional system. As such we correlate the structure at the interface with the dynamics in a novel approach.

It can be seen that water in the smallest hydrophilic pore a) pointing away and towards the surface has the highest prevalence. But water pointing away is much more diffusive compared to water pointing towards the surface as indicated by longer blue arrows and higher normalized diffusion values. It can be seen in figure 5-19 that the water structure changes multiple times when increasing pore size. The dipole angle distribution and self-diffusion looks very different for each pore system a), b) and c).

In case b) it is striking that the prevalence of an orientation and self-diffusion overlap in normalized form. The most common orientation is also the most diffusive one. This partly explains why the overall measured diffusion in b) is higher

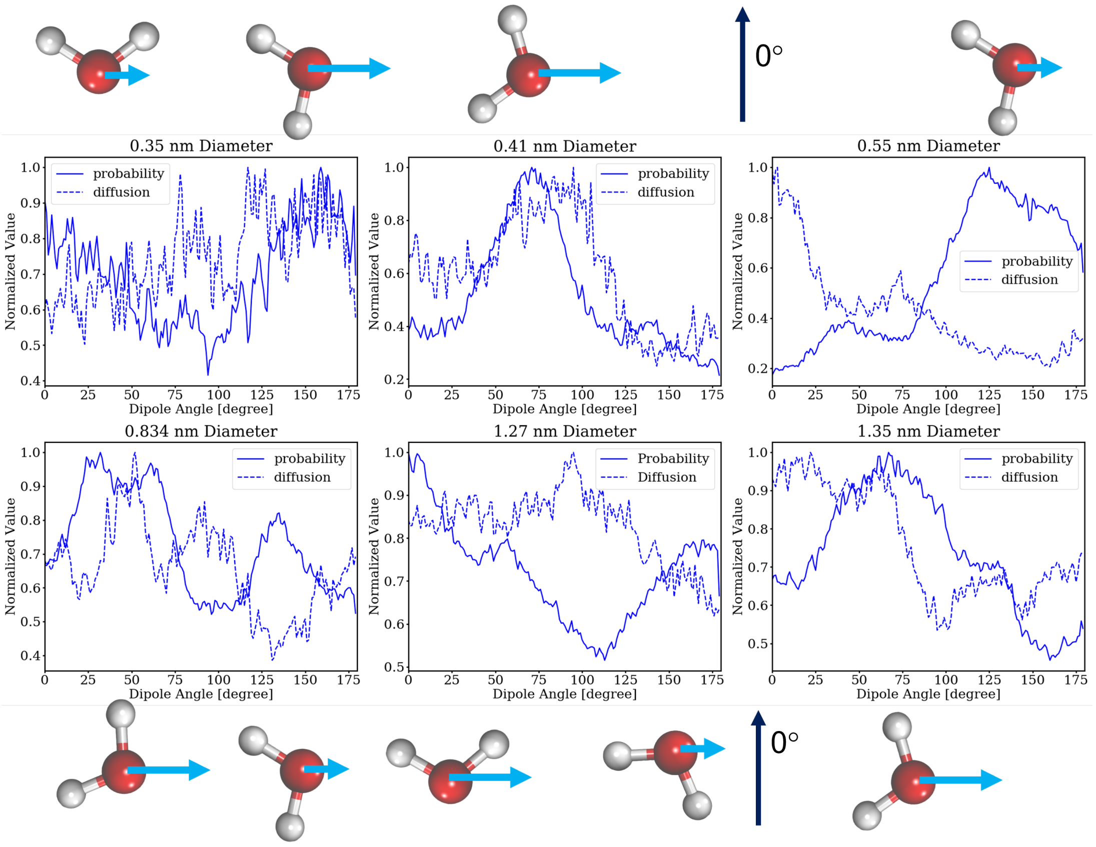

Figure 5-19: Normalized angular distribution of water inside hydrophilic nanopores a) to f) based on the water dipole vector (solid) and the corresponding diffusion (dotted). Angles are given relative to the surface normal. 0° means water is oriented towards the surface. 180° means water is oriented away from the surface.

than in a) and c). As by contrast in c) the most common coordination is the slowest one to diffuse. This is a valid explanation, as the whole system is an interface and such this view of the system actually describes the whole system.

From pore d) on the structure changes less as pores become bigger. These systems generally have a high prevalence of water oriented towards the surface up to an dipole angle of 50° and an prevalence of water oriented away from the surface in a 30° range. In system d) this is least pronounced but the tendency can be observed. Similarly the self-diffusion is relatively higher for coordination towards the surface at around 0° and lower for water that tends to point away from the surface.

This means that for larger pores water pointing towards the surface is faster while water pointing away is slower and could slow overall diffusion at the interface. This would indicate that water pointing away from the surface is more strongly bound and water pointing towards the surface is most weakly bound.

If we combine those thoughts with results from 5.3.6 we can cross-validate results. The SFG results for the larger hydrophilic pores showed a large "liquid" likes positive peak at around 3700 cm^{-1} and a large shoulder up to around 3500 cm^{-1}. The prevalence is skewed towards positive contributions from orientations towards the surface. This aligns with the results in figure 5-19. But we also found that those contributions are actually the fastest water molecules at the interface.

This can be illustrated again by comparing the two largest hydrophilic pore systems e) and f). The reported diffusion for system f) is actually considerably slower than for e). In fact it is $1.75 \times 10^{-9}\ m^2/s$ vs $2.12 \times 10^{-9}\ m^2/s$. From the interface perspective the slowest diffusive species is water pointing away from the surface with a relatively high prevalence, while a much wider range of coordinations has slower diffusion in pore f). Logically this means more water molecules will diffuse slowly and limit self-diffusion. The main species to slow diffusion at the surface in pore f) has a dipole angle of around $100° \ to \ 150°$ relative to the surface. Sulpizi et al. [51] for example analyzed different coordinations at the flat silica oxide surface and divided interactions in H-bond donor and acceptor interactions. In pore f) less water around $100° \ to \ 150°$ is in existence and that

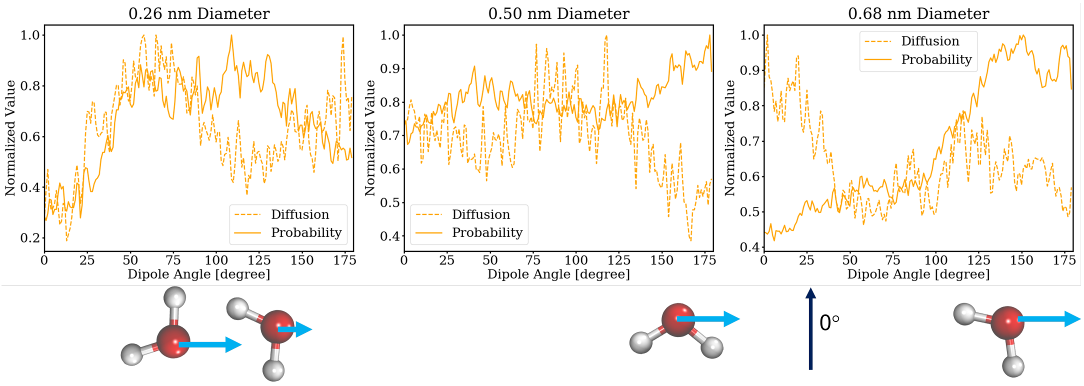

Figure 5-20: Normalized angular distribution of water inside hydrophobic nanopores a) to c) based on the water dipole vector (solid) and the corresponding diffusion (dotted). Angles are given relative to the surface normal. 0° means water is oriented towards the surface. 180° means water is oriented away from the surface.

water is diffusing quickly, meaning it very likely is more weakly bonded or does not act as H-Bond donor at all. While the same coordination in pore f) is slowed down much. This would indicate that the same coordination is a H-Bond donor or at least a stronger one, which slows down diffusion.

Be reminded that according to our findings, agreeing with previous studies, diffusion at the surface is generally slower, but as most of our systems followed this relation faster overall diffusion is correlated with faster diffusion at the surface as well. So molecules preventing fast diffusion at the surface are expected to also be responsible for slower overall diffusion through the strong network effects of water.

The same analysis has been done for the hydrophobic pore systems and can be seen in figure 5-20 (a to c) and figure 5-21 (d +e). Small pores show strong changes in structure again, but the tendency for the self-diffusion distribution is interestingly very similar to the hydrophilic case. In the smallest hydrophobic pore a) the most common coordination is at an dipole angle of around 60° perpendicular to the surface. This is also the fastest species. The further further pores starting with b) then already show very similar distributions. This means that water oriented towards the surface tends to be most diffusive in our case as well and water oriented away from the surface tends to be less diffusive. The main difference lies in the prevalence of said orientations and in variations of diffusion for orientations between 50° and 120°.

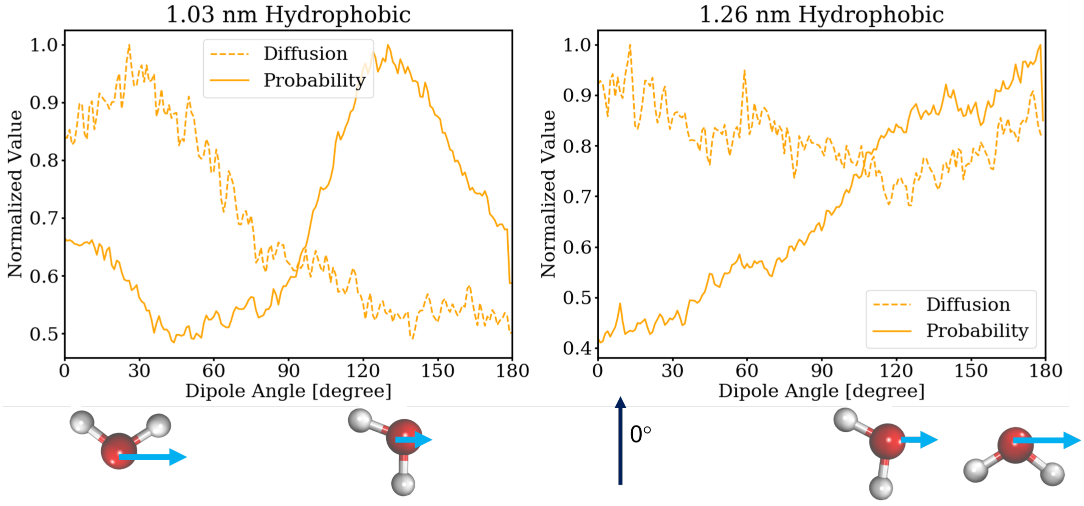

Figure 5-21: Normalized angular distribution of water inside hydrophobic nanopores d) and f) based on the water dipole vector (solid) and the corresponding diffusion (dotted). Angles are given relative to the surface normal. 0° means water is oriented towards the surface. 180° means water is oriented away from the surface.

The diffusion distribution for example is very similar in c) and d). Coordinations between 0° and 60° are the most diffusive, while all others are much slower, with water oriented away from the surface at 180° is the slowest. It is only half as diffusive as water oriented towards the surface. Contrary to this in the largest hydrophobic pore e) the water oriented away from the surface is nearly as fast as water oriented towards the surface. The slowest water at the surface has a dipole angle between 90° and 140°. But the differences in ratio are also very different. While the slowest orientations are up to 50 % slower in smaller pores until d), the largest pore e) has a the minimum at only 30 % slower.

So we would expect that overall diffusion in pore e) is faster than in pore d). But the opposite is true as the diffusion coefficients for d) and e) are $3.92 \times 10^{-9}\ m^2/s$ and $2.89 \times 10^{-9}\ m^2/s$ respectively. It seems to be that the diffusion has to be seen in accordance with the total diffusion. Even though the most prevalent water in pore d) is also the slowest, when comparing the total diffusion coefficient it is still faster than the slowest water in pore e), that is also relatively prevalent.

When comparing the results of the hydrophilic and hydrophobic systems one thing becomes obvious. The internal diffusion distribution does not vary much depending on hydrophobicity. water pointing towards the surface is the fastest and water pointing away tends to be slower. But the prevalence in hydrophilic pores shows more water of the fastest kind, while water of the slower kind is more prevalent in hydrophobic pores. This might sound counterintuitive as overall diffusion is faster in hydrophobic pores. But we have to remember, that even the less diffusive molecules in hydrophobic pores have a higher diffusion coefficient than the slowest or even the fastest coordinations. But it seems to indicate that overall water diffusion is very much limited by the slowest diffusive species in a pore environment. The amount of this species is of less importance for diffusion. This would be one avenue to explain the impact of hydrophobicity.

5.4 Conclusion

I extensively studied idealized hydrophilic and hydrophobic silica oxide pore systems (see figure 5-22). The hydrophilic systems ranged from 0.35 to 1.37 nm in size and were pristine. The hydrophobic systems were functionalized with some ratio of trifluoromethyl and ranged from 0.25 nm to 1.26 nm in size. I generally found higher diffusion in hydrophobic pores of the same size, especially for the larger pores in this study (Figure 5-23). The fastest diffusion was found in the second largest hydrophilic pore of size 1.27 nm at $2.12 \times 10^{-9}\ m^2/s$ and in the second largest hydrophobic pore of size 1.03 nm at $3.92 \times 10^{-9}\ m^2/s$. The diffusion coefficient in the hydrophobic system is considerably larger not only than the in the hydrophilic systems, but also larger than measured in bulk water ($2.29 \times 10^{-9}\ m^2/s$) and in bulk calculated with the same method ($2.39 \times 10^{-9}\ m^2/s$). Interestingly, diffusion slowed for the slightly larger pore systems, which could indicate that there are narrow distinct pore sizes that support fast diffusion up to super diffusion faster than bulk water. This aspect definitely needs further investigation.

The radial diffusion distribution showed that this was not based on a difference in behavior based on the relationship between diffusion at the pore wall and diffusion at the pore center. More so it is based on diffusion at the interface being higher, just as overall diffusion is through the pore. This underlines the importance of the water network. The distance between the water surface and the pore wall was found to be larger in hydrophobic than hydrophilic pores.

We also found a stark shift in the power and SFG spectra based on size and functionalization at the surface. When pore size in hydrophilic pores increases there is a slight red shift in the main peak in the power spectrum, raising the prevalence of the "liquid" H-bond band. In the hydrophobic spectrum the more strongly bonded "liquid" peak becomes more pronounced as well. This means the changes with pore size are relatively independent of hydrophobicity, even though changes with increasing pore size are more pronounced in the hydrophobic pores. Generally the power spectrum is strongly blue shifted for hydrophobic systems compared to hydrophilic ones with a large "free" or dangling peak. But what does this shift mean and how much of it is actually happening at the surface,

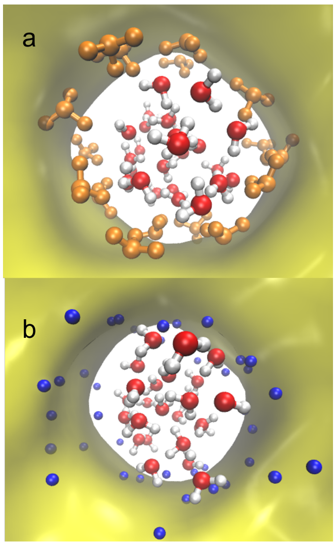

Figure 5-22: Abstracted silica oxide pore systems with functional groups and water depicted on a molecular level. Pristine hydrophilic (b) and hydrophobic trifluoromethyl (a). Hydroxyl is shown in blue; trifluoromethyl is shown in orange.

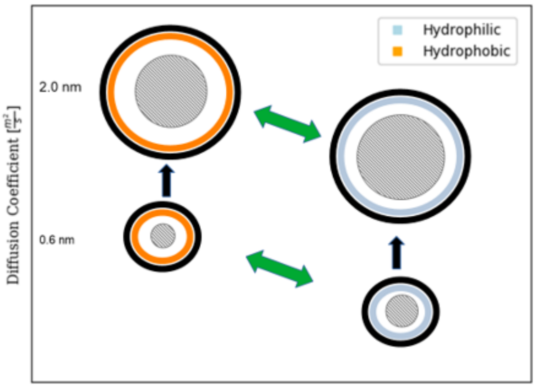

Figure 5-23: Generally diffusion increases with increasing pore size. The distance between hydrophobic pore walls and water is bigger than in the hydrophilic cases. Water diffusion in hydrophobic pores is faster for comparable pore sizes, even higher than in bulk water for larger hydrophobic pores.

where our main interest lies.

The SFG also provides information about the coordination and is surface specific. It shows that with increasing hydrophilic pore size the "liquid" like peak increase from the power spectrum does not happen. It is either not happening at the surface (which is likely because the "liquid" interactions are water-water interactions from the bulk region) or the interactions are symmetric. Such the SFG actually shows a decrease in "liquid" like interactions towards the surface with pore size. That means less water molecules are pointing towards the surface and are interacting strongly with the pore walls. And we observe an actual shift towards more "free" or dangling bonds in the larger hydrophilic pores at around 3680 cm^{-1}. Comparable the SFG in hydrophobic pores shows a strong "free" peak at around 3720 cm^{-1}, slightly shifted blue from the 3680 cm^{-1} hydrophilic peak from O-H stretches pointing towards the surface. It also shows strong "ice" and "liquid" like peaks from water O-H stretches pointing away from the surface.

The angular distribution changes towards a regime where water pointing towards the surface with a dipole angle of 0° relative to the surface perpendicular has the highest prevalence and water pointing away from the surface is also relatively prevalent. This is different from analysis of Cimas et al. [219], who found very low prevalence of water orientation at around 0° and 180° and only reported relatively small differences between other orientations.

In the hydrophobic system of similar size as seen in figure 5-24 the prevalence of the dipole vector increases the more the water is pointing away from the surface. This prevalence in the hydrophobic pore is also more pronounced than the differences between the probabilities of dipole vectors in similar hydrophilic pores. This is in contrast with the angular distribution of the self-diffusion coefficient. Here the behavior of self-diffusion is very similar in hydrophilic and hydrophobic pores. Diffusion is generally higher at small angles and slower between 60° and 120°. One small difference is, that water directly pointing away from the surface with an dipole angle of around 180○ is again nearly as fast as water pointing towards the surface in the hydrophobic case.

Combining the calculated SFG spectrum, the dipole angle distribution and diffusion dynamics we can begin to draw a full picture of the situation as in fig-

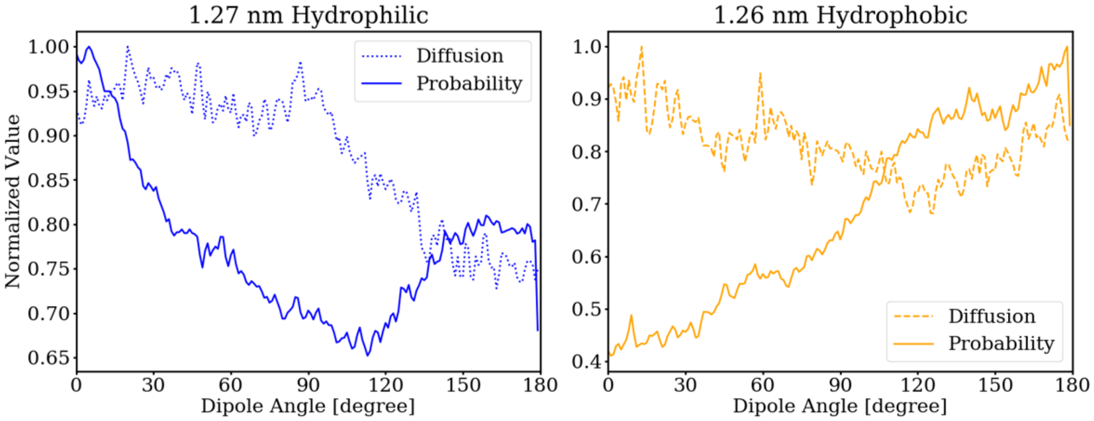

Figure 5-24: Dipole angle distribution (full line) relative to the surface perpendicular for the hydrophilic (left) and hydrophobic (right) case of similar size pores. The diffusion vs the dipole angle is shown in dotted lines.

ure 5-25. In the center the SFG spectrum for one hydrophilic and one hydrophobic pore system of similar size are shown, as reported in section 5.3.6. Using the angular distribution as shown in figure 5-24 and section 5.3.7 we can determine the most prevalent water orientations based on the dipole vector relative to the surface perpendicular inside the pore.

Those most likely cases of interest are shown in descending order in their respective category in figure 5-25. We can also deduct which orientations are responsible for the peaks in the SFG spectrum. When interpreting the large "free" or dangling peak in the hydrophobic pore systems the second and third most prevalent coordinations have a positive contribution. As the third coordination is very much underrepresented we would expect this peak to be a results of coordination two with a dipole angle of around 120°. But this coordination is the slowest to diffuse and as such probably most strongly bonded of all coordinations, which would question whether this coordination is responsible for the "free" dangling peak at $3720cm^{-1}$. A relatively low amount of coordination c) in the hydrophobic case might be responsible for the very strong "free" peak. The negative "ice" and "liquid" like peaks on the other hand can be attributed to coordination a) and b). Here we would consider b) being the most strongly bonded as it is diffusing the slowest and such being responsible for the low frequency "ice" like band, while coordination a) would be responsible for the more "liquid" like peak.

When explaining the positive response of the hydrophilic system between

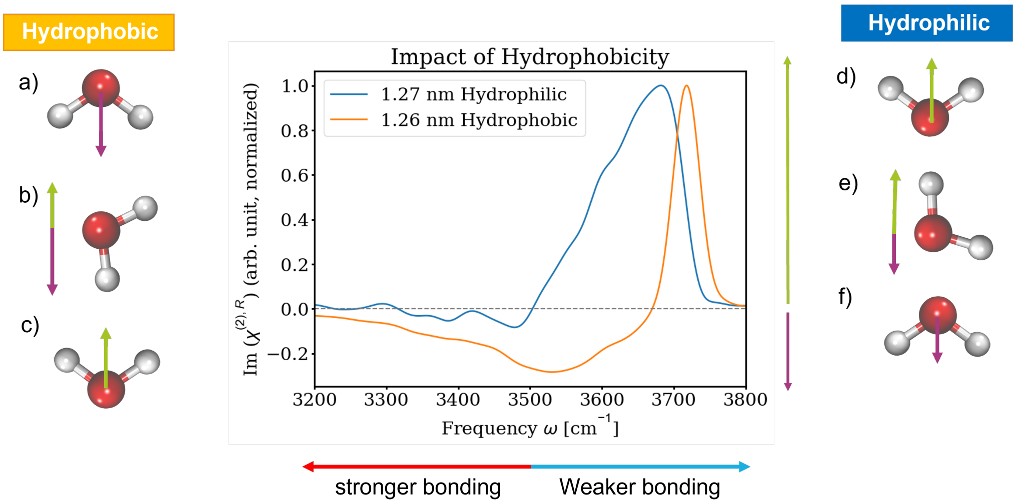

Figure 5-25: The SFG spectra for "large" hydrophilic and hydrophobic pores of the same size can be seen in the middle. The three most prevalent or important water coordinations at the surface are shown on the left (hydrophobic pore) and on the left (hydrophilic pore). Their contributions in terms of O-H stretches is depicted in green for positive and in red for negative.

3500 cm^{-1} and 3700 cm^{-1} using angular distributions we identified three most important coordination which are shown in figure 5-25 on the right side. The top configuration with the dipole angle of 0° is the most prevalent and also the fastest diffusion one. When connecting this with the idea that less bounded molecules diffuse faster we expect the top coordination to be responsible for the peak shoulder with the highest wavenumber and with the highest peak at around 3680 cm^{-1}. This is a good assumption as the highest peak should coincide with the highest prevalence. The second configuration than would be attributed to stronger bonded molecules between 3500 cm^{-1} and 3600 cm^{-1}. Those are less prevalent but also play a large role. This also aligns with the diffusion as we would expect more weakly bounded water at higher wavenumbers to diffuse faster. This is the case as coordination d) is diffusing faster than coordination e). There are only few molecules of coordination f) that are also diffusing the slowest and as such might be responsible for the very slight negative feature between 3300 cm^{-1} and 3500 cm^{-1}, or the contributions could just be negated by positive response contributions from coordination e).

When looking at the diffusion coefficient of different coordinations we can try to further interpret the results of the hydrophilic case based on the silanol groups water can be close to. With the line of thought of Cimas et al. [219] The

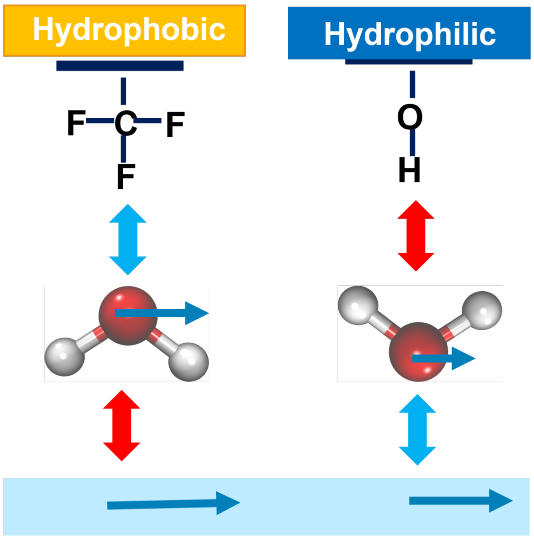

Figure 5-26: The most common water coordination in hydrophobic and hydrophilic pores is either weakly or strongly bonded to the pore surface and their diffusion is indicated. Water in hydrophobic pores because of the coordination is also strongly interacting with the water at the middle of the pore.

attributed water in hydrophilic pores between 0° to 60° to water acting as an acceptor from out-of-plane silanols. This would correspond to coordination d) that are diffusing the fastest. From 70° to 140° who are on average donating one H-bond to a silanol. This would be coordination e) in our case. As water at higher angles 140° to 180° (coordination f) is the slowest in our hydrophilic pore it seems possible that part of those molecules donate two H-bond to silanol groups.

this would mean that coordination d) is more likely to be bound to isolated silanol only and as such is most strongly bound. This fits well with it being the slowest to diffuse, while coordinations bound to geminal only are also relatively slow to diffuse. Most others then would be bound to vicinal silanol that is either in- or out-of-plane. Generally water pointing away from the surface would be expected closer to the in-plane silanol and more strongly bonded, while the water at the out-of-plane silanol would be the H-bond donor and less strongly bonded. Our diffusion distribution supports this analysis, as the diffusion is getting continuously slower from 0° to 180°.

As reported in section 5.3.1 the Gibbs surface distance is much larger in the hydrophobic systems and the H-bond coordination number is also much lower at the surface and in some cases also at the pore center. This means while water pointing away from the surface is also the slowest in many hydrophobic cases, it is not bound to the surface as strongly. This can also be seen in section 5.3.6, where I discussed the SFG spectrum. There the "liquid" like signal was much more pronounced in the hydrophilic cases. In the hydrophobic cases they are less pronounced and mostly strongly linked to other water molecules. As such the water network is increasing more strongly and water at the surface is swept through the pore in an accelerated manner.

This ultimately leads to faster overall diffusion in hydrophobic pores especially keeping in mind the lower coordination at the pore center in some of the hydrophobic system, which could also contribute. But the radial diffusion distribution as we have discussed is very similar for hydrophobic and hydrophilic pores. Another interesting finding is the diversity in structure for nanopores of different sizes. The structure and dynamics inside larger pores $>$ 2 nm are not necessarily true for pores only somewhat smaller and structure is still more complex for pores with single file water. There might even be specific pore sizes that exhibit preferable properties as faster diffusion or more selectivity in a very narrow size range. For example the second largest hydrophobic system d) has a very specific structure with molecules of coordination b) and c) being most likely, with very little of coordination a). This actually led to the fastest overall diffusion of all systems.

Influence of polarity on water structure in trimethylsilanol (TMS) functionalized and hydrophilic pores

6.1 Introduction

The results of this study were published in Ref. [256]. I advise a study of this research as the results presented here are only part of the research and a full read is needed for a comprehensive understanding. Parts of the results explained here are are directly taken from Ref. [256]. Instead of a functionalization with CF_3 as done in the previous chapter 5 we used TMS in cooperation with an experimental group in this work to reduce surface polarity.

6.2 Computational Details

An amorphous bulk silica melt structure was created by heating a beta-cristobalite crystalline silica structure containing 648 atoms (216 Si + 432 O) to 4000 K at zero pressure via an NPT-ensemble based Metropolis Monte Carlo (MC) simulation using periodic boundary conditions (PBC). The simulation uses the potential developed by D.M. Tether, and modified and tested by Cormack, Du et al. (TCD) [229] for all atomic interactions. Long-range interactions were calculated using the standard Ewald summation. The simulation reaches equilibrium after 2 million MC-steps. The system's density was 2.31 g/cm^3 at this stage, being very close to P. Gallo's MCM-41 model [230], but higher than fused silica (2.2 g/cm^3) and lower than quartz (2.6 g/cm^3). Experimental data from previous studies reveal an apparent density of 2.37 g/cm^3 for MCM-41 silica. [231] The silica pore was created by removing a cylindrical volume of a specific diameter from the melt structure of size 28.64 Å X 28.64 Å X 14.32 Å. Free valences on the inner surfaces were saturated via additional hydroxyl groups according to a defined process during which trisilanol groups and isolated oxygens were removed from the surfaces. For the non-pristine system, several of the hydroxyl groups were exchanged with trimethylsilyl group (TMS), mimicking a more hydrophobic environment using the pore modulation and visualization tool Avogadro. [232] This was done in a way to achieve a decently even distribution of the groups on the surface. The systems were equilibrated using the PM6 semiempirical method [233], as implemented with PBC in the CP2K simulation package [234] for 10 ps. Bulk water was generated via CMD simulations using the second-generation Car-Parrinello-based quantum ring polymer contraction method of Kühne and coworkers. [121, 235] Then the water was transferred into the pore system. After inserting the water, the systems were again equilibrated for 10 ps via periodic PM6 semi-empirical MD [233] calculations [234].The temperature of the system was controlled via a massive CSVR thermostat at 300 K with a time constant of 300 fs. [236] Using a discretized time step of 0.5 fs the total trajectory length of the production run was 40 ps for all systems.

6.3 Results

6.3.1 Characterization of simulated pore systems based on surface area, effective diameter, and functional group density

The two studied systems are pristine MCM-41, having a hydroxyl functionalization, and a more hydrophobic functionalization with Trimethylsilyl (TMS). The surface area was calculated according to the pore size before functionalization. The density of functional groups was calculated by dividing the number of functional groups of hydrophilic (OH) or hydrophobic ($Si(CH_3)_3$) nature by the surface area of said pore. Fraction of hydrophobicity is given by the number of hydrophobic groups divided by the number of hydrophilic groups as summarized in table 6.1. The surface area of the pristine pore is less than that of the hydrophobic, because it was chosen to consider the introduction of larger functional groups in the hydrophobic system. The functional groups will decrease the effective pore size, bringing the effective diameter more in line with the pristine pore which will minimize the finite size effect on pore structure and dynamics. The overall functional group density on the pore surface as described in table 6.1 is 6.84 hydroxyl groups per nm^2 for the pristine pore and slightly lower at around 6.42 for hydrophobic. Si-OH is exchanged with TMS groups so that roughly 19 % of groups are TMS, while the remaining 81 % remain hydroxyl groups.

Pore models	Surface Area nm^2	Si-OH density nm^{-2}	TMS Density nm^{-2}	Hydrophobicity %
Hydrophilic (pristine)	5.85	6.84	0	0
Hydrophobic (TMS)	8.10	5.32	1.24	19

Table 6.1: Data to characterize the theoretical pore models based on surface area, Si-OH density, TMS density and hydrophobicity.

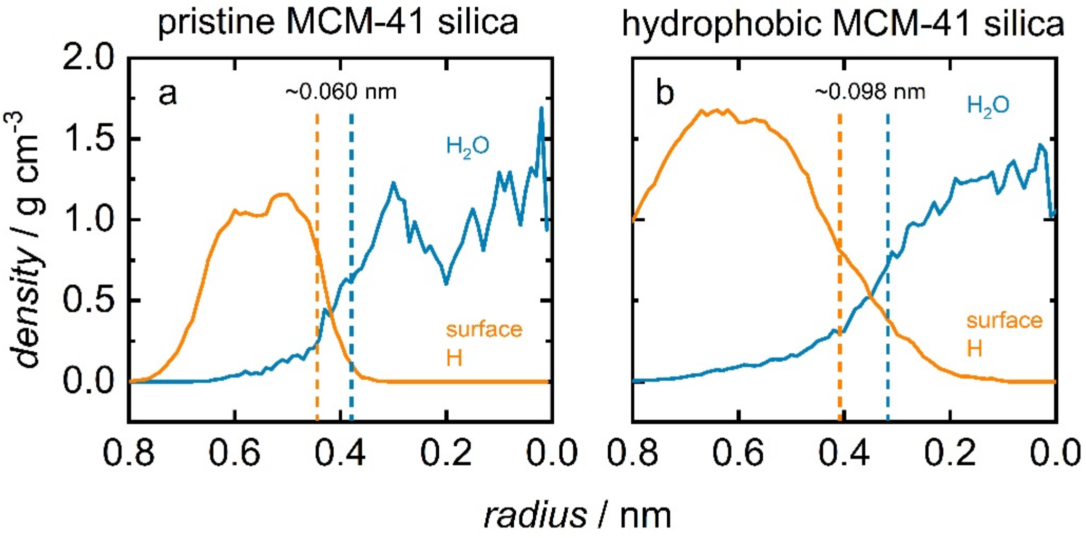

Figure 6-1: The radial density of water (blue) and functional wall elements (orange) for the pristine (a) and hydrophobic (b) pores. The density is shown from the pore surface towards the center of the pore.

6.3.2 Radial Density Distribution of water and defining functional group elements

We calculated the densities of water and the respective pore surfaces in different pore setups as shown in figure 6-1. The radial density of the water in the pore is shown in blue, while the density of the surface functional groups is shown in orange. In the pristine pore the surface is made up of hydroxyl groups. Such the hydrogen density can give an estimate of the surface coordinates in the system. In the case of the pristine pore in figure 6-1a, the hydrogen density is shown in orange with scaled density to ensure visual comparability of the graphs. The Gibbs dividing surface formula is used as a model to quantify the distance between the medium and pore surface. In the pristine pore this was calculated to 0.60 nm in distance. The water is structured roughly into two layers, one close to the pore surface and one at the center of the pore.

he hydrogen density is showing a shallow double peak from the different hydroxyl group arrangements. In pristine silica pores the hydroxyl groups can either be free and pointing away from the surface, which we attribute to the first peak, or form hydrogen bonds with other hydroxyl groups orienting them parallel to the surface (second peak). [219] The hydrophobic system (6-1 b) inhibits less structure, but a steady increase in density towards the center of the pore in a more uniform distribution. The same is true for the methyl hydrogen representing the pore surface of the hydrophobic system. The modeled TMS pore seems to be more uneven with the free radius of the pore varying as the slope of the density is much shallower. The distance of the Gibbs dividing surfaces is 0.098 nm. This is more than in the pristine pore that had a distance of 0.060 nm. Water tends to be further away from the pore surface in the hydrophobic TMS environment. This is in line with studies reporting similar effects. [257]

6.3.3 Coordination number of water molecules with itself and the hydroxyl Surface

As hydrogen bonding plays a big role in the structure and dynamics inside the pore, we want to understand the hydrogen bonding process better. We calculated the hydrogen-bond coordination number across the pore based on rOO $<$ 3.55 Å and (O2; O1, H1) $<$ pi/6, which is a common definition. [159, 243] We also included the coordination numbers of the water molecules with the hydroxyl and TMS groups in our systems using rCO $<$ 3.65 Å and (C2; O1, H1) $<$ pi/6. For the pristine pore shown in figure 6-2, the water-water coordination number decreases constantly from 0.6 nm onwards (blue), while the water-silanol coordination increases steadily (orange) but is providing less coordination in total (green). That leads to a lower coordination number close to the surface and a relatively deep impact onto interface structure. Comparing the results to those in Figure 6-1, most water molecules in pore areas with high densities are highly coordinated, but a small amount of water at the surface is less coordinated. One possible explanation is that less coordinated molecules only interact with silanol groups that are oriented parallel to the surface and have already formed hydrogen bonds with other silanol groups. Those water molecules would act as hydrogen bond donors and move very close to the surface. We attributed those silanol groups to the hydrogen peak around 0.6 nm radius in figure 6-1.

For the hydrophobic environment in Figure 6-2b the decrease in total coordination number is a bit less smooth but still constant to the surface. Even though the density profile as seen in Figure 6-1b is less structured than that of the pristine pore, the total coordination is very similar, indicating that water is

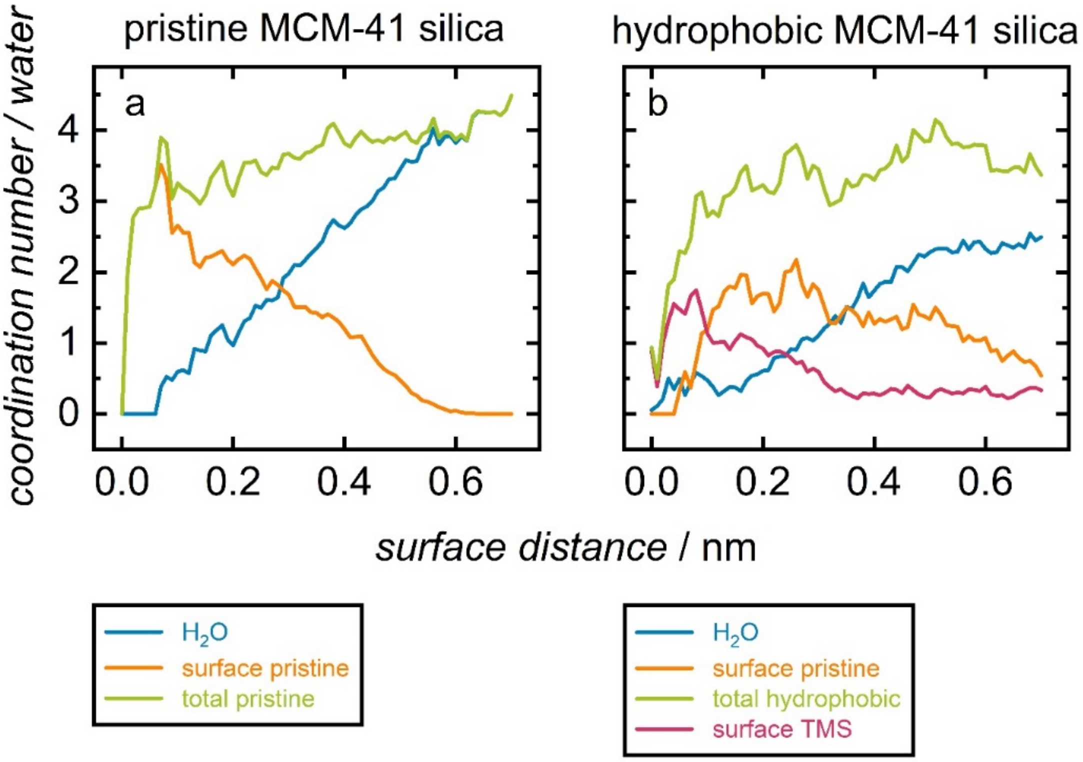

Figure 6-2: Coordination number of water molecules shown against surface distance in nm. Coordination number from water-water hydrogen bonds (blue), water-pristine (orange), water-TMS (red) and total coordination (green).

naturally rearranging its coordination balancing molecular variances in density. Water-silanol coordination is still present over the whole radius, but closest to the surface TMS is the main source of water coordination. At the surface, water-water coordination plays the least important role. The main mechanism seems to be competition between the functional groups for water coordination relative to their density. In this case as described in Table 6.1 the ratio of silanol to TMS is around 4:1.

6.3.4 Analysis of water structure at the surface based on velocity-velocity surface specific SFG calculations

We used the previously adapted SFG method to calculate the responses for the pristine and hydrophobic pores (6-3). The characteristic response important to our discussion is happening between 2200 cm^{-1} and 2800 cm^{-1}. The shift compared to experimental results is based on the use of semi-empirical PM6. PM6 underreports the O-H stretch frequency but reproduces SFG responses qualita-

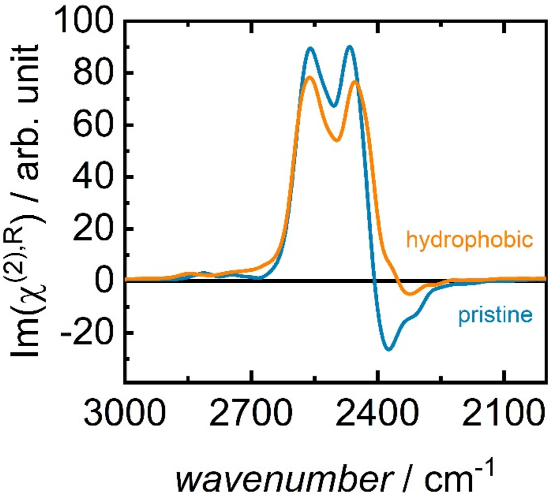

Figure 6-3: Imaginary part of the second order SFG spectra of the pristine pore (blue) and hydrophobic pore (orange) in the range between 2000 cm^{-1} and 3000 cm^{-1}.

tively otherwise. A positive response means O-H stretch modes pointing towards the surface are dominant in that wavenumber range, while a negative response means the opposite. Thus, in a bulk system no response would be seen as all configurations should be equally likely. The pristine and hydrophobic pore exhibit a main positive peak just below 2600 cm^{-1}. This peak (with the highest frequency) correlates with the strength of bonding of said OH stretching vibrations in the bond network. The highest frequency peak is generally attributed to free O-H-stretch modes. In the hydrophobic case a slight shoulder of the peak towards higher frequencies can be observed, perhaps attributed to being further away from the surface as discussed in Figure 6-1 b or a low number of molecules close to the surface showing lower coordination number as seen in Figure 6-2.

As the SFG also gives an insight into the dominant orientation of those groups it can be deduced that in that wavenumber range both systems are dominated by O-H stretch modes pointing towards the surface. The second peak is generally attributed to more 'liquid-like' bonded O-H modes, and both systems show similar positive peaks. As the wavenumber decreases, O-H-stretch modes decrease and water is more strongly bound, called 'ice-like' bonding. In the pristine sample, O-H-modes pointing away from the surface are dominating in that strongly bonded region. The SFG response in that area is relatively broad, with a second smaller peak at around 2300 cm^{-1} that may be attributed to water bond asymmetry in the following water layer. We have shown in Ref. [256] that the 'ice-like' strongly bonded response is more pronounced in the pristine case. Combining both analyses it can be said that in the pristine pore 'ice-like' water at the surface is found more often than in the hydrophobic pore. The 'ice-like' response arises from O-H-stretch modes pointing away from the surface. We assume that water with OH stretches pointing away from the surface interacts strongly with non-hydrogen bonded silanol groups at the surface, that act as hydrogen bond donor, while the water oxygen acts as the acceptor. Those molecules as discussed in Ref. [256] can move closer to the pore surface.

6.3.5 Analysis of water structure at the surface based angular distribution analysis

The angular distribution of the O-H stretching vibration of the water molecules relative to the silica pore surfaces normal was calculated (Figure 6-4) to supplement the previously discusses SFG data. The angle between the surface normal, oxygen and the hydrogen atoms H and H' are called α and β, respectively. Chemically speaking, H and H' are equal and therefore α and β interchangeable. Angles smaller than ± 90° are pointing towards the pore surface (i.e., lead to a positive signal in the SFG spectrum) and vice versa. figure 6-4 a visualizes the angular distribution of O-H vibrations within a pristine and figure 6-4 b in a hydrophobic silica pore. A few water molecule configurations are highlighted in Figure 6-4 c.

The angular distribution in the pristine case in generally broader compared to the hydrophobic surface. Therefore, it is more likely to find water in configuration A (H and H' pointing away from the pore surface, $\alpha = \beta = 74°$) in the pristine pore compared to the hydrophobic, even though it is a quite unlikely configuration overall. The probability to find a configuration rises with an increasing amount O-H vibrations pointing towards the surface, leading to the conclusion that the configurations B ($\alpha = 0°, \beta = -104°$), C ($\alpha = 52°, \beta = -52°$) and D ($\alpha = 60°, \beta = -44°$) can be found with an increasing probability for the pristine and hydrophobic surface. The latter configuration is about the center of the most frequent configurations. All these effects could already be observed in the SFG spectra in Figure 6-3 as the negative signal (O-H vibrations pointing away from

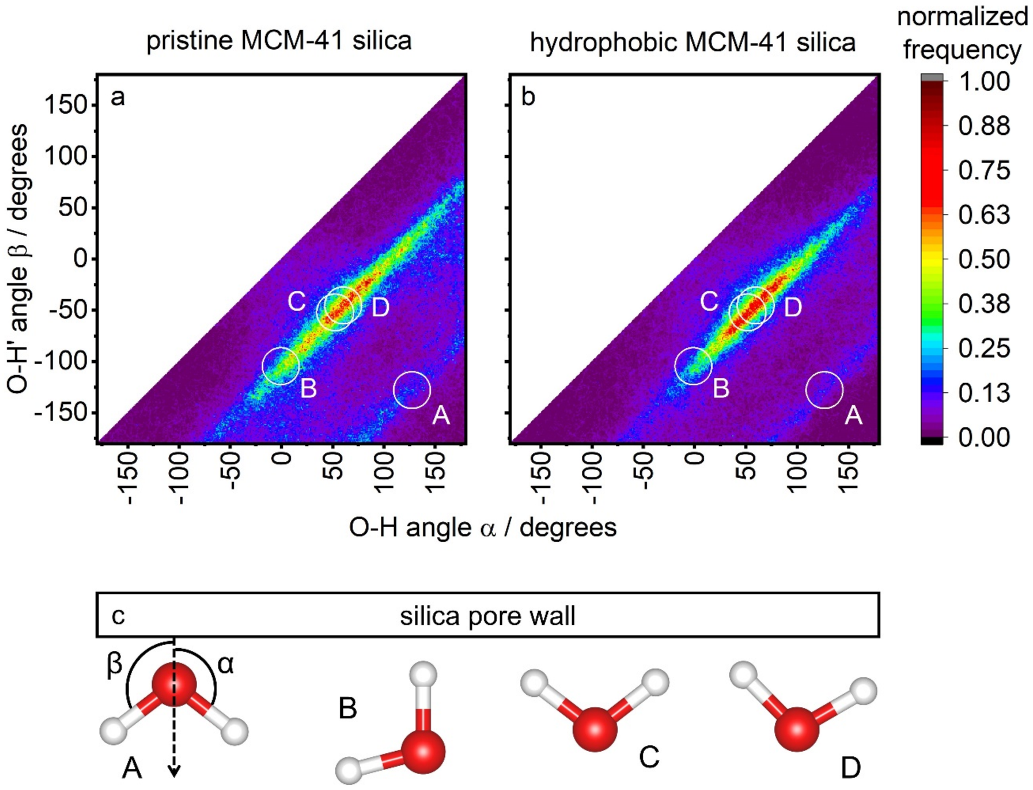

Figure 6-4: Angular distribution of the water molecule's OH stretching vibrations relative to the pristine (a) and hydrophobic silica surface (b). Example water molecule configurations are depicted in (c).

the surface like in configuration A) is more pronounced for the pristine pore. The water molecules generally prefer to orient both of their O-H bond vibrations towards the silica surface (configuration B and D; both with a positive response in the SFG spectra in Figure 6-3). Thus, the 'ice-like' negative SFG response can likely be attributed to configuration B and D with slight impact from A. As A and D can act as hydrogen bond donor to unbound silanol groups they play the biggest part in explaining the structure in the pristine pore and the existence of 'ice-like' bonding.

6.4 Conclusion

When the pore wall polarity in silica mesopores is altered from hydrophilic (pristine) to hydrophobic, the structure of water within the porous system changes. In the case of a hydrophilic mesopore filled with water, IR spectroscopy reveals a predominant ice-like structure because of comparably strong interactions between the water molecules with the pore wall, confirmed by calculated sum frequency spectra. For a hydrophobic surface, i.e., after surface functionalization with trimethylsilyl chloride, water behaves more liquid-like. As there are fewer interaction sites at the pore wall, the water molecules rather interact with each other than with the silica surface. Water sorption experiments further confirm these findings where the pore filling step is shifted to higher relative pressure for a more hydrophobic environment while the overall amount of water is reduced simultaneously. These effects can be further investigated by computed silica pores, enabling to monitor water density distribution with respect to the distance to the silica pore wall. The coordination number changes in dependence on the decoration of the surface with silanol, methyl, and trifluoromethyl groups as these alter the polarity of the pore wall. The calculated coordination numbers reflect the influence of the pore wall-to-water interactions from the experimental results. SFG and angular distribution calculation of the pore system reveal the water orientations most likely responsible for our findings in both systems.

Impact of hydrophobicity on the gas self-diffusion of oxygen and water vapor in mesoporous silica pores

7.1 Introduction

To investigate the influence of pores on gas transport through SiOx coatings, Wilski et al. established a simulation model to describe gas permeation through PET with defective barrier coatings [258, 259]. Experimental validation showed good agreement, but the studied pore size was limited to macropores. This approach is now extended with a molecular dynamics approach. While this prevents a consideration of the entire macroscopic system with the full range of pore sizes and distributions, it enables us to investigate the interaction between the permeating species and the pore wall and can give valuable information. Gas diffusion in micropores is a complex phenomenon that depends on pore size, morphology, the concentration of the gas medium and temperature. Some work has been done to calculate diffusion of gases in porous systems [260, 261, 262] mostly using classical molecular dynamics especially around CH3 diffusion and selectivity for hydrogen

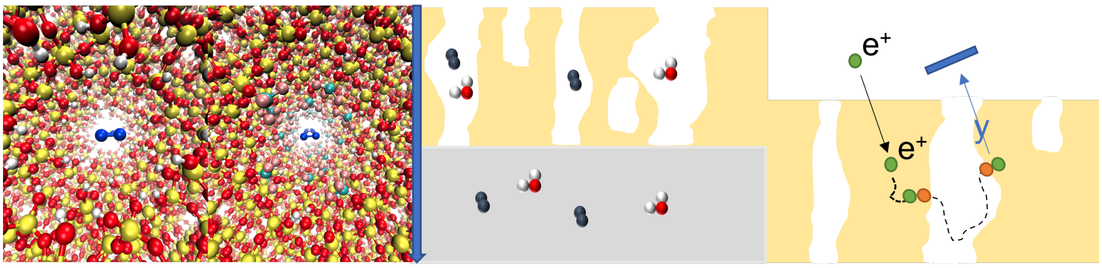

Figure 7-1: Molecular level pores structures (left) and the principles of selectivity (center) and methodology of PALS (right) encapsulates the context of this work.

purification [263]. Molecular dynamics simulations have been shown to be a good tool to study gas diffusion in porous systems as they are able to accurately model the pore wall and medium interactions on a molecular level. [264, 265] The main avenue of study has focused on the impact of temperature and pressure on the diffusion or on equilibrium. It is generally accepted, that with higher pressure self-diffusivity decreases. [266] The importance of surface interactions has been shown to play an important role in porous silica. Krishna and van Baten [267] showed, that gas diffusion in porous structures can be sub diffusive if molecules are trapped in small pores [268] or adsorbing at the surface. Most of the studies analyze singular pore sizes or a porous medium with a network or pores [269] with some work done in silica zeolites [270]. In a work studying high temperature diffusion in mesoporous amorphous carbon structures R. Ranganathan et al. found a wide range of diffusivities based on pore size and pore wall interactions [271].

The silica oxide pore structures where created similar to those used in chapter 5 and chapter 6. After this the systems were equilibrated for 20 ps using the PM6 (oxygen gas) and PM6-FM (water vapor) semi-empirical method [233] as implemented with PBC in the CP2K simulation package [234] by molecular simulations [235]. The two systems, hydrophilic (left) and hydrophobic (right) can be seen in figure 7-2. The temperature of the system was controlled via a massive CSVR thermostat at 300 K with a time constant of 300 fs [236]. Using a discretized time step of 0.5 fs the total trajectory length of the production run was at least 50 ps for all systems.

The results are part of a study with Franke and Zysk et al. to access the transport of gas through PECVD coatings. The general principles are shown in Figure 7-1.

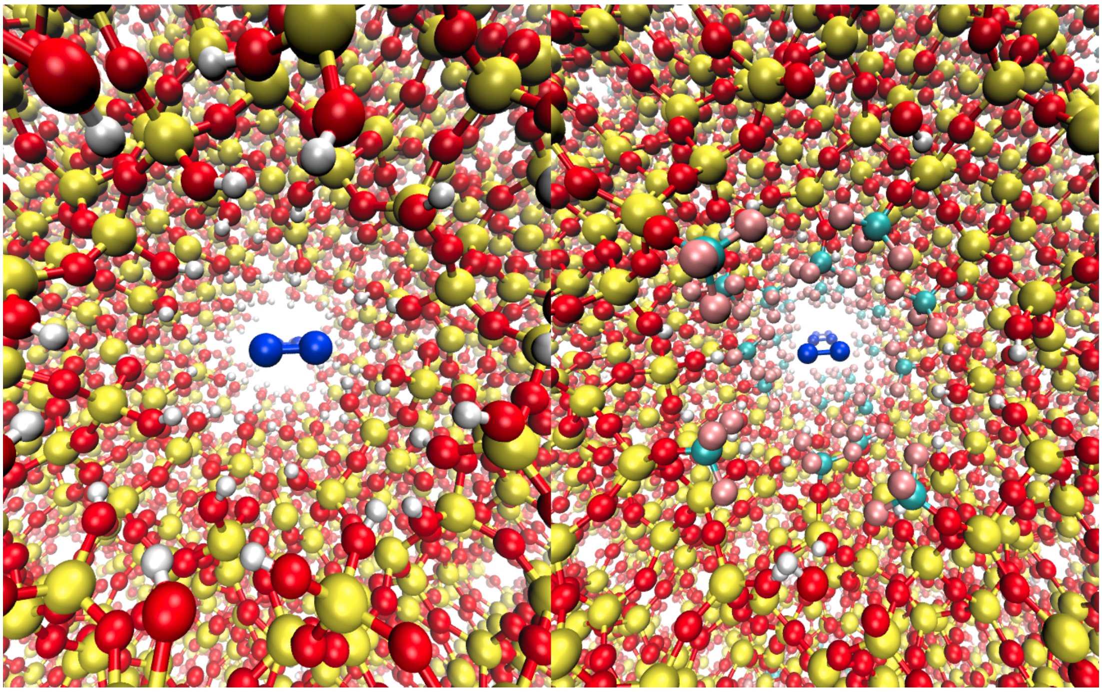

Figure 7-2: Molecular pore structure of idealized amorphous silica oxide pores with hydrophilic (OH) (left) and hydrophobic (CF_3) (right) functional groups and oxygen gas as medium

7.2 Results

Using PALS, we have started to characterize the porosity and pore size distribution for diameters smaller than 2 nm. The small sizes lead not only to a sieving effect but also pore wall interactions play a prominent role in the diffusion and selectivity. Different diffusion mechanisms can overlap, and it is very hard to quantify the influence of each mechanism for a given pore size. This makes it difficult to calculate the diffusion with macroscopic formulas as it would be possible in larger pores where Knudsen diffusion is most dominant. Molecular Dynamics calculations are used here to calculate the self-diffusion coefficients of oxygen gas and water vapor in idealized silica oxide micropores with diameters from 0.25 to 1.30 nm. Two examples of the modelled structures can be seen in Figure 7-2. Oxygen gas in a hydrophobic environment (right) and hydrophilic environment (left) are shown. To determine the pore sizes of our molecular models we used the open-source software Zeo++ [237] to calculate the largest included sphere diameter. The resulting diameters are the pore sizes used in this work (Figure

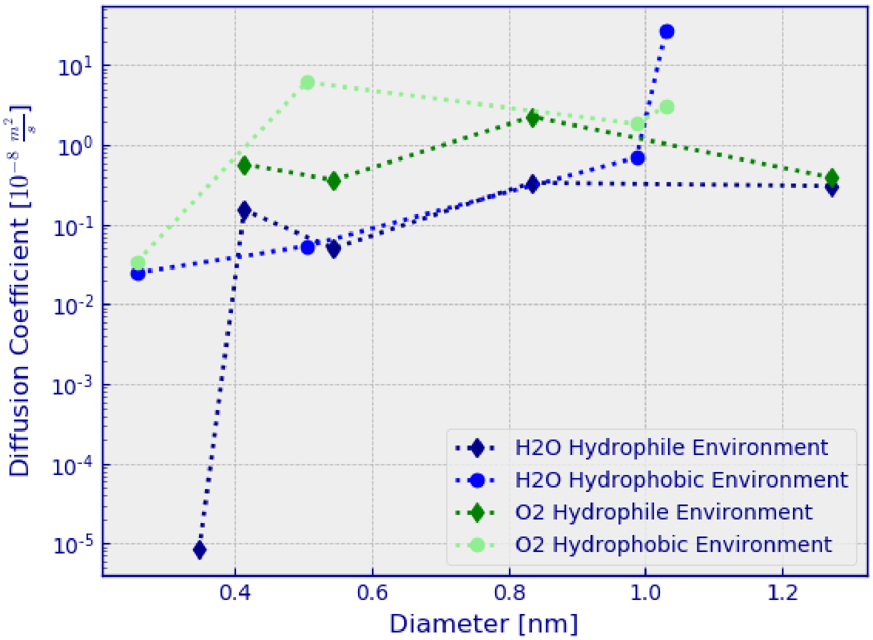

Figure 7-3: Self-Diffusion Coefficients of O_2 gas (dark green/green) and H_2O vapor (dark blue/blue) in Hydrophilic (Diamant) and hydrophobic (Circle) silica oxide pores with diameters ranging from 0.25 to 1.30 nm in logarithmic scale.

7-3).

As can be seen in Figure 8 the magnitude of most of the diffusion regimes is around 10^{-8} to $10^{-9} m^2/s$. The oxygen gas self-diffusion over pore diameter in logarithmic scale is shown in dark green and green for the hydrophilic (Circle) pore functionalization and the hydrophobic (Diamond) pore functionalization respectively. The water vapor self-diffusion is shown in dark blue and blue for the same two cases respectively. For micropores smaller than 0.56 nm in diameter, labelled d_3 by the PALS analysis of lifetime components, it can be seen, that very small hydrophobic pores of around 0.25 nm size still show considerable self-diffusion. The hydrophilic pores on the other hand showed concentration behavior for pores smaller than 0.4 nm i.e., diffusion occurs only to a very limited extent. This was evident in the fact that no diffusion could be observed for oxygen and water vapor showed strongly sub diffusive behavior. This indicates that the pore ranges from PALS for d_3 agree decently well with our calculations, as 0.4 nm is close to our minimum of self-diffusion in pores. The results for very small hydrophobic pores might be partly based on polarity effects that lead to stronger bonding in hydrophilic cases compared to hydrophilic ones and the structure of the hydrophobic pore system. Not all silanol groups are functionalized with hydrophobic groups in hydrophobic pores, which might lead to a more uneven pore surface. Thus, the effective diameter might vary over the simulation time. Up to 0.56 nm there is little difference between water vapor diffusion based on hydrophobicity, but oxygen gas diffusion is about one magnitude faster in the hydrophobic pores. Also, oxygen gas self-diffusion is faster than water vapor diffusion in similar pores. As PALS analysis estimates that up to 21 % of relative porosity exists in this pore range of d_3 between 0.42 nm and 0.56 nm it is important to note that self-diffusion in that pore range is considerable for all cases and especially for oxygen gas in hydrophobic pores. For the second pore size range d_4 estimated to be between 0.60 nm and 2.50 nm our studied pore range extends to 1.3 nm. The self-diffusion increases for all four studied systems up to a diameter of 1 nm with hydrophobicity having little influence on the water vapor diffusion. This is unexpected as the pore wall to medium distance is still relatively small, and interactions could play a role. Oxygen gas self-diffusion is till around one magnitude faster than water vapor diffusion. Due to its non-polar nature, oxygen might interact less and thus diffuse faster. It is way less likely to adsorb, while water vapor might briefly adsorb and desorb at the surface, which may lead to condensation effects. In this context, the influence of capillary condensation should be considered separately in further investigations. An interesting finding is, that self-diffusion for pores > 1.0 nm seems to decrease slightly or at least not increase in hydrophilic pores but does increase in hydrophobic ones. With those calculation we can quantify the pore range distribution and diffusion in combination to classify porous systems.

Bibliography

[1] Lawrie B Skinner, Congcong Huang, Daniel Schlesinger, Lars GM Pettersson, Anders Nilsson, and Chris J Benmore. Benchmark oxygen-oxygen pair-distribution function of ambient water from x-ray diffraction measurements with a wide q-range. *The Journal of chemical physics*, 138(7):074506, 2013.

[2] Quan Du, Eric Freysz, and Y. Ron Shen. Surface vibrational spectroscopic studies of hydrogen bonding and hydrophobicity. *Science*, 264(5160):826–828, May 1994.

[3] Q Du, R Superfine, E Freysz, and YR Shen. Vibrational spectroscopy of water at the vapor/water interface. *Physical Review Letters*, 70(15):2313, 1993.

[4] Shumei Sun, Fujie Tang, Sho Imoto, Daniel R Moberg, Tatsuhiko Ohto, Francesco Paesani, Mischa Bonn, Ellen HG Backus, and Yuki Nagata. Orientational distribution of free oh groups of interfacial water is exponential. *Physical Review Letters*, 121(24):246101, 2018.

[5] Cho-Shuen Hsieh, R Kramer Campen, Masanari Okuno, Ellen HG Backus, Yuki Nagata, and Mischa Bonn. Mechanism of vibrational energy dissipation of free oh groups at the air–water interface. *Proceedings of the National Academy of Sciences*, 110(47):18780–18785, 2013.

[6] Jan Schaefer, Ellen HG Backus, Yuki Nagata, and Mischa Bonn. Both inter-and intramolecular coupling of o–h groups determine the vibrational response of the water/air interface. *The Journal of Physical Chemistry Letters*, 7(22):4591–4595, 2016.

[7] Satoshi Nihonyanagi, Tatsuya Ishiyama, Touk-kwan Lee, Shoichi Yamaguchi, Mischa Bonn, Akihiro Morita, and Tahei Tahara. Unified molecular view of the air/water interface based on experimental and theoretical χ (2) spectra of an isotopically diluted water surface. *Journal of the American Chemical Society*, 133(42):16875–16880, 2011.

[8] Satoshi Nihonyanagi, Ryoji Kusaka, Ken-ichi Inoue, Aniruddha Adhikari, Shoichi Yamaguchi, and Tahei Tahara. Accurate determination of complex χ (2) spectrum of the air/water interface. *The Journal of Chemical Physics*, 143(12):124707, 2015.

[9] Shoichi Yamaguchi. Development of single-channel heterodyne-detected sum frequency generation spectroscopy and its application to the water/vapor interface. *The Journal of chemical physics*, 143(3):034202, 2015.

[10] M Brehm, M Thomas, S Gehrke, and B Kirchner. Travis—a free analyzer for trajectories from molecular simulation. *The Journal of chemical physics*, 152(16):164105, 2020.

[11] Matthew Welborn, Jiahao Chen, Lee-Ping Wang, and Troy Van Voorhis. Why many semiempirical molecular orbital theories fail for liquid water and how to fix them. *Journal of Computational Chemistry*, 36(12):934–939, 2015.

[12] Tatsuhiko Ohto, Mayank Dodia, Jianhang Xu, Sho Imoto, Fujie Tang, Frederik Zysk, Thomas D Kühne, Yasuteru Shigeta, Mischa Bonn, Xifan Wu, et al. Accessing the accuracy of density functional theory through structure and dynamics of the water–air interface. *The journal of physical chemistry letters*, 10(17):4914–4919, 2019.

[13] M. Born and R. Oppenheimer. Zur quantentheorie der molekeln. *Annalen der Physik*, 389(20):457–484, 1927.

[14] Péter Pulay. Convergence acceleration of iterative sequences. the case of scf iteration. *Chemical Physics Letters*, 73(2):393–398, 1980.

[15] J. A. Pople, D. P. Santry, and G. A. Segal. Approximate self-consistent molecular orbital theory. i. invariant procedures. *The Journal of Chemical Physics*, 43(10):S129–S135, 1965.

[16] Luigi Oleari, Gianni De Michelis, and Lorenzo Di Sipio. The spectra and electronic structure of tetrahedral ions. *Molecular Physics*, 10(2):111–129, 1966.

[17] G. Klopman. *A Semiempirical Treatment of Molecular Structures. Molecular Terms and Application to Diatomic Molecules*, volume 86. J. Am. Chem. Soc., 1964.

[18] M. J. S. Dewar and N. L. Hojvat(Sabelli). The split p-orbital (s.p.o.) method. relationship to other m.o. treatments and application to benzene, butadiene, and naphthalene. *J. Phys. Chem.*, 66:2310, 1962.

[19] N. Matage and K. Nishimoto. Electronic structure and spectra of nitrogen heterocycles. *Zeitschrift für Physikalische Chemie*, 13(34):140–157, 1957.

[20] M. J. S. Dewar amd W. Thiel. Ground states of molecules. the mndo method. approximations and parameters. *J. Am. Chem. Soc.*, 99:4899–4907, 1977.

[21] Julian D. Gale. Semi-empirical methods as a tool in solid-state chemistry. *Faraday Discuss.*, 106:219–232, 1997.

[22] Teodoro Laino and Jürg Hutter. Notes on "ewald summation of electrostatic multipole interactions up to quadrupolar level" [j. chem. phys. 119, 7471 (2003)]. *The Journal of Chemical Physics*, 129(7):074102, 2008.

[23] M. J. S. Dewar, E. G. Zoebisch, F. E. Healy, and J. J. P. Stewart. Am1: A new general purpose quantum mechanical molecular model. *Am. Chem. Soc.*, 107:3902, 1985.

[24] James J. P. Stewart. Optimization of parameters for semiempirical methods ii. applications. *Journal of Computational Chemistry*, 10(2):221–264, 1989.

[25] James JP Stewart. Optimization of parameters for semiempirical methods v: Modification of nddo approximations and application to 70 elements. *Journal of Molecular modeling*, 13(12):1173–1213, 2007.

[26] James JP Stewart. Optimization of parameters for semiempirical methods iv: extension of mndo, am1, and pm3 to more main group elements. *Journal of Molecular Modeling*, 10(2):155–164, 2004.

[27] J E Lennard-Jones. Cohesion. *Proceedings of the Physical Society*, 43(5):461–482, sep 1931.

[28] Yan Zhou and Jingzhi Pu. Reaction path force matching: A new strategy of fitting specific reaction parameters for semiempirical methods in combined qm/mm simulations. *Journal of Chemical Theory and Computation*, 10(8):3038–3054, 2014. PMID: 26588275.

[29] Antoine Marion, Gérald Monard, Manuel F. Ruiz-López, and Francesca Ingrosso. Water interactions with hydrophobic groups: Assessment and recalibration of semiempirical molecular orbital methods. *The Journal of Chemical Physics*, 141(3):034106, 2014.

[30] Erwin Schrödinger. Quantisierung als eigenwertproblem. *Annalen der physik*, 385(13):437–490, 1926.

[31] Erwin Schrödinger. Quantisierung als eigenwertproblem. *Annalen der physik*, 385(13):437–490, 1926.

[32] Max Born and W Heisenberg. Zur quantentheorie der molekeln. In *Original Scientific Papers Wissenschaftliche Originalarbeiten*, pages 216–246. Springer, 1985.

[33] Enrico Fermi. Un metodo statistico per la determinazione di alcune priorieta dell'atome. *Rend. Accad. Naz. Lincei*, 6(602-607):32, 1927.

[34] Llewellyn H Thomas. The calculation of atomic fields. In *Mathematical proceedings of the Cambridge philosophical society*, volume 23, pages 542–548. Cambridge University Press, 1927.

[35] P. Hohenberg and W. Kohn. Inhomogeneous electron gas. *Phys. Rev.*, 136:B864–B871, Nov 1964.

[36] Seymour H Vosko, Leslie Wilk, and Marwan Nusair. Accurate spin-dependent electron liquid correlation energies for local spin density calculations: a critical analysis. *Canadian Journal of physics*, 58(8):1200–1211, 1980.

[37] David C Langreth and SH Vosko. Response functions and nonlocal approximations. In *Advances in quantum chemistry*, volume 21, pages 175–199. Elsevier, 1990.

[38] Peter S Liss and PG Slater. Flux of gases across the air-sea interface. *Nature*, 247(5438):181–184, 1974.

[39] John P Perdew, Kieron Burke, and Matthias Ernzerhof. Generalized gradient approximation made simple. *Physical review letters*, 77(18):3865, 1996.

[40] Axel D Becke. Density-functional exchange-energy approximation with correct asymptotic behavior. *Physical review A*, 38(6):3098, 1988.

[41] Erin R Johnson and Axel D Becke. A post-hartree-fock model of intermolecular interactions: Inclusion of higher-order corrections. *The Journal of chemical physics*, 124(17):174104, 2006.

[42] Stephan Ehrlich, Jonas Moellmann, Werner Reckien, Thomas Bredow, and Stefan Grimme. System-dependent dispersion coefficients for the dft-d3 treatment of adsorption processes on ionic surfaces. *ChemPhysChem*, 12(17):3414–3420, 2011.

[43] Akio Koide. A new expansion for dispersion forces and its application. *Journal of Physics B: Atomic and Molecular Physics (1968-1987)*, 9(18):3173, 1976.

[44] Kühne T. and Khaliullin R. Electronic signature of the instantaneous asymmetry in the first coordination shell of liquid water. *Nat Commun*, 4:1450, 2013.

[45] D. KKühne and Rustam Z Khaliullin. Nature of the asymmetry in the hydrogen-bond networks of hexagonal ice and liquid water. *Journal of the American Chemical Society*, 136(9):3395–3399, 2014.

[46] Ruben Staub, Marcella Iannuzzi, Rustam Z Khaliullin, and Stephan N Steinmann. Energy decomposition analysis for metal surface–adsorbate interactions by block localized wave functions. *Journal of Chemical Theory and Computation*, 15(1):265–275, 2018.

[47] Rustam Z Khaliullin and Thomas D Kühne. Microscopic properties of liquid water from combined ab initio molecular dynamics and energy decomposition studies. *Physical Chemistry Chemical Physics*, 15(38):15746–15766, 2013.

[48] Khaliullin R.Z., Cobar E.A., Lochan R.C., Bell A.T., and Head-Gordon M. Unravelling the origin of intermolecular interactions using absolutely localized molecular orbitals. *J Phys Chem A*, 111(36):8753–65, 2007.

[49] Poul B Petersen, Richard J Saykally, Martin Mucha, and Pavel Jungwirth. Enhanced concentration of polarizable anions at the liquid water surface: Shg spectroscopy and md simulations of sodium thiocyanide. *The Journal of Physical Chemistry B*, 109(21):10915–10921, 2005.

[50] Tatsuhiko Ohto, Kota Usui, Taisuke Hasegawa, Mischa Bonn, and Yuki Nagata. Toward ab initio molecular dynamics modeling for sum-frequency generation spectra; an efficient algorithm based on surface-specific velocity-velocity correlation function. *The Journal of Chemical Physics*, 143(12):124702, 2015.

[51] Tatsuhiko Ohto, Kota Usui, Taisuke Hasegawa, Mischa Bonn, and Yuki Nagata. Toward ab initio molecular dynamics modeling for sum-frequency generation spectra; an efficient algorithm based on surface-specific velocity-velocity correlation function. *The Journal of Chemical Physics*, 143(12):124702, 2015.

[52] Jian Liu, William H Miller, Francesco Paesani, Wei Zhang, and David A Case. Quantum dynamical effects in liquid water: A semiclassical study on the diffusion and the infrared absorption spectrum. *The Journal of chemical physics*, 131(16):164509, 2009.

[53] Akihiro Morita and James T Hynes. A theoretical analysis of the sum frequency generation spectrum of the water surface. ii. time-dependent approach. *The Journal of Physical Chemistry B*, 106(3):673–685, 2002.

[54] Zhaohui Wang, Yoonsoo Pang, and Dana D Dlott. The vibrational stokes shift of water (hod in d 2 o). *The Journal of chemical physics*, 120(18):8345–8348, 2004.

[55] Naveen Kumar Kaliannan, Andres Henao Aristizabal, Hendrik Wiebeler, Frederik Zysk, Tatsuhiko Ohto, Yuki Nagata, and Thomas D. Kühne. Impact of intermolecular vibrational coupling effects on the sum-frequency generation spectra of the water/air interface. *Molecular Physics*, 118(4):1620358, 2020.

[56] John P Perdew, John A Chevary, Sy H Vosko, Koblar A Jackson, Mark R Pederson, Dig J Singh, and Carlos Fiolhais. Atoms, molecules, solids, and surfaces: Applications of the generalized gradient approximation for exchange and correlation. *Physical review B*, 46(11):6671, 1992.

[57] Axel D Becke and Marc R Roussel. Exchange holes in inhomogeneous systems: A coordinate-space model. *Physical Review A*, 39(8):3761, 1989.

[58] Jianmin Tao, John P Perdew, Viktor N Staroverov, and Gustavo E Scuseria. Climbing the density functional ladder: Nonempirical meta–generalized gradient approximation designed for molecules and solids. *Physical Review Letters*, 91(14):146401, 2003.

[59] AD Becke. Density-functional thermochemistry. iii the role of exact exchange j chem phys 98: 5648–5652, 1993.

[60] Marcos F Calegari Andrade, Hsin-Yu Ko, Roberto Car, and Annabella Selloni. Structure, polarization, and sum frequency generation spectrum of interfacial water on anatase tio2. *The journal of physical chemistry letters*, 9(23):6716–6721, 2018.

[61] Marialore Sulpizi, Marie-Pierre Gaigeot, and Michiel Sprik. The silica–water interface: how the silanols determine the surface acidity and modulate the water properties. *Journal of chemical theory and computation*, 8(3):1037–1047, 2012.

[62] I-Feng W Kuo and Christopher J Mundy. An ab initio molecular dynamics study of the aqueous liquid-vapor interface. *Science*, 303(5658):658–660, 2004.

[63] Ming Ma, Gabriele Tocci, Angelos Michaelides, and Gabriel Aeppli. Fast diffusion of water nanodroplets on graphene. *Nature materials*, 15(1):66–71, 2016.

[64] Marcel D Baer, I-Feng W Kuo, Douglas J Tobias, and Christopher J Mundy. Toward a unified picture of the water self-ions at the air–water interface: A density functional theory perspective. *The Journal of Physical Chemistry B*, 118(28):8364–8372, 2014.

[65] Thomas D. Kühne, Tod A. Pascal, Efthimios Kaxiras, and Yousung Jung. New insights into the structure of the vapor/water interface from large-scale first-principles simulations. *The Journal of Physical Chemistry Letters*, 2(2):105–113, 2011. PMID: 26295528.

[66] Jan Kessler, Hossam Elgabarty, Thomas Spura, Kristof Karhan, Pouya Partovi-Azar, Ali A. Hassanali, and Thomas D. Kühne. Structure and dynamics of the instantaneous water/vapor interface revisited by path-integral and ab initio molecular dynamics simulations. *The Journal of Physical Chemistry B*, 119(31):10079–10086, 2015. PMID: 26174102.

[67] Michael J Gillan, Dario Alfe, and Angelos Michaelides. Perspective: How good is dft for water? *The Journal of chemical physics*, 144(13):130901, 2016.

[68] I-Chun Lin, Ari P Seitsonen, Mauricio D Coutinho-Neto, Ivano Tavernelli, and Ursula Rothlisberger. Importance of van der waals interactions in liquid water. *The Journal of Physical Chemistry B*, 113(4):1127–1131, 2009.

[69] Yuki Nagata, Tatsuhiko Ohto, Mischa Bonn, and Thomas D Kühne. Surface tension of ab initio liquid water at the water-air interface. *The Journal of chemical physics*, 144(20):204705, 2016.

[70] Stefan Grimme, Andreas Hansen, Jan Gerit Brandenburg, and Christoph Bannwarth. Dispersion-corrected mean-field electronic structure methods. *Chemical reviews*, 116(9):5105–5154, 2016.

[71] Jiří Klimeš and Angelos Michaelides. Perspective: Advances and challenges in treating van der waals dispersion forces in density functional theory. *The Journal of chemical physics*, 137(12):120901, 2012.

[72] Luis Ruiz Pestana, Narbe Mardirossian, Martin Head-Gordon, and Teresa Head-Gordon. Ab initio molecular dynamics simulations of liquid water using high quality meta-gga functionals. *Chemical science*, 8(5):3554–3565, 2017.

[73] Junwei Lucas Bao, Laura Gagliardi, and Donald G Truhlar. Self-interaction error in density functional theory: An appraisal. *The journal of physical chemistry letters*, 9(9):2353–2358, 2018.

[74] Saman Hosseinpour, Fujie Tang, Fenglong Wang, Ruth A Livingstone, Simon J Schlegel, Tatsuhiko Ohto, Mischa Bonn, Yuki Nagata, and Ellen HG Backus. Chemisorbed and physisorbed water at the tio2/water interface. *The journal of physical chemistry letters*, 8(10):2195–2199, 2017.

[75] Chungwen Liang, Jonggu Jeon, and Minhaeng Cho. Ab initio modeling of the vibrational sum-frequency generation spectrum of interfacial water. *The Journal of Physical Chemistry Letters*, 10(5):1153–1158, 2019.

[76] Jürg Hutter, Marcella Iannuzzi, Florian Schiffmann, and Joost VandeVondele. cp2k: atomistic simulations of condensed matter systems. *Wiley Interdisciplinary Reviews: Computational Molecular Science*, 4(1):15–25, 2014.

[77] Richard Car and Mark Parrinello. Unified approach for molecular dynamics and density-functional theory. *Physical review letters*, 55(22):2471, 1985.

[78] Paolo Giannozzi, Stefano Baroni, Nicola Bonini, Matteo Calandra, Roberto Car, Carlo Cavazzoni, Davide Ceresoli, Guido L Chiarotti, Matteo Cococcioni, Ismaila Dabo, et al. Quantum espresso: a modular and open-source software project for quantum simulations of materials. *Journal of physics: Condensed matter*, 21(39):395502, 2009.

[79] Manuel Guidon, Jurg Hutter, and Joost VandeVondele. Auxiliary density matrix methods for hartree- fock exchange calculations. *Journal of chemical theory and computation*, 6(8):2348–2364, 2010.

[80] Stefan Grimme, Jens Antony, Stephan Ehrlich, and Helge Krieg. A consistent and accurate ab initio parametrization of density functional dispersion correction (dft-d) for the 94 elements h-pu. *The Journal of chemical physics*, 132(15):154104, 2010.

[81] Daniel GA Smith, Lori A Burns, Konrad Patkowski, and C David Sherrill. Revised damping parameters for the d3 dispersion correction to density functional theory. *The journal of physical chemistry letters*, 7(12):2197–2203, 2016.

[82] Oleg A Vydrov and Troy Van Voorhis. Nonlocal van der waals density functional: The simpler the better. *The Journal of chemical physics*, 133(24):244103, 2010.

[83] S. Goedecker, M. Teter, and J. Hutter. Separable dual-space gaussian pseudopotentials. *Phys. Rev. B*, 54:1703–1710, Jul 1996.

[84] DR Hamann, M Schlüter, and C Chiang. Norm-conserving pseudopotentials. *Physical Review Letters*, 43(20):1494, 1979.

[85] Taisuke Hasegawa and Yoshitaka Tanimura. A polarizable water model for intramolecular and intermolecular vibrational spectroscopies. *The Journal of Physical Chemistry B*, 115(18):5545–5553, 2011.

[86] Wilbert J Smit, Fujie Tang, M Alejandra Sánchez, Ellen HG Backus, Limei Xu, Taisuke Hasegawa, Mischa Bonn, Huib J Bakker, and Yuki Nagata. Excess hydrogen bond at the ice-vapor interface around 200 k. *Physical Review Letters*, 119(13):133003, 2017.

[87] Gregory R Medders and Francesco Paesani. Dissecting the molecular structure of the air/water interface from quantum simulations of the sum-frequency generation spectrum. *Journal of the American Chemical Society*, 138(11):3912–3919, 2016.

[88] Fujie Tang, Tatsuhiko Ohto, Taisuke Hasegawa, Wen Jun Xie, Limei Xu, Mischa Bonn, and Yuki Nagata. Definition of free o–h groups of water at the air–water interface. *Journal of chemical theory and computation*, 14(1):357–364, 2018.

[89] Jian Liu, William H Miller, George S Fanourgakis, Sotiris S Xantheas, Sho Imoto, and Shinji Saito. Insights in quantum dynamical effects in the infrared spectroscopy of liquid water from a semiclassical study with an ab initio-based flexible and polarizable force field. *The Journal of chemical physics*, 135(24):244503, 2011.

[90] Xinzijian Liu and Jian Liu. Critical role of quantum dynamical effects in the raman spectroscopy of liquid water. *Molecular Physics*, 116(7-8):755–779, 2018.

[91] Mauro Del Ben, Jürg Hutter, and Joost VandeVondele. Probing the structural and dynamical properties of liquid water with models including non-local electron correlation. *The Journal of chemical physics*, 143(5):054506, 2015.

[92] Mohan Chen, Hsin-Yu Ko, Richard C Remsing, Marcos F Calegari Andrade, Biswajit Santra, Zhaoru Sun, Annabella Selloni, Roberto Car, Michael L Klein, John P Perdew, et al. Ab initio theory and modeling of water. *Proceedings of the National Academy of Sciences*, 114(41):10846–10851, 2017.

[93] Bingqing Cheng, Edgar A Engel, Jörg Behler, Christoph Dellago, and Michele Ceriotti. Ab initio thermodynamics of liquid and solid water. *Proceedings of the National Academy of Sciences*, 116(4):1110–1115, 2019.

[94] Mayank Dodia, Tatsuhiko Ohto, Sho Imoto, and Yuki Nagata. Structure and dynamics of water at the water–air interface using first-principles molecular dynamics simulations. ii. nonlocal vs empirical van der waals corrections. *Journal of Chemical Theory and Computation*, 15(6):3836–3843, 2019.

[95] Michael G Medvedev, Ivan S Bushmarinov, Jianwei Sun, John P Perdew, and Konstantin A Lyssenko. Density functional theory is straying from the path toward the exact functional. *Science*, 355(6320):49–52, 2017.

[96] Sharon Hammes-Schiffer. A conundrum for density functional theory. *Science*, 355(6320):28–29, 2017.

[97] Mischa Bonn, Yuki Nagata, and Ellen H. G. Backus. Molecular structure and dynamics of water at the water–air interface studied with surface-specific vibrational spectroscopy. *Angewandte Chemie International Edition*, 54(19):5560–5576, 2015.

[98] Ondrej Marsalek and Thomas E Markland. Quantum dynamics and spectroscopy of ab initio liquid water: The interplay of nuclear and electronic quantum effects. *The journal of physical chemistry letters*, 8(7):1545–1551, 2017.

[99] M. O. Andreae and P. J. Crutzen. Atmospheric aerosols: Biogeochemical sources and role in atmospheric chemistry. *Science*, 276(5315):1052–1058, may 1997.

[100] Sutapa Ghosal, John C. Hemminger, Hendrik Bluhm, Bongjin Simon Mun, Eleonore L. D. Hebenstreit, Guido Ketteler, D. Frank Ogletree, Felix G. Requejo, and Miquel Salmeron. Electron spectroscopy of aqueous solution interfaces reveals surface enhancement of halides. *Science*, 307(5709):563–566, jan 2005.

[101] Man Xu, Cheng Y. Tang, Aaron M. Jubb, Xiangke Chen, and Heather C. Allen. Nitrate anions and ion pairing at the air-aqueous interface. *J. Phys. Chem. C*, 113(6):2082–2087, December 2008.

[102] E. M. Knipping, M. J. Lakin, K. L. Foster, P. Jungwirth, D. J. Tobias, R. B. Gerber, D. Dabdub, and B. J. Finlayson-Pitts. Experiments and simulations of ion-enhanced interfacial chemistry on aqueous nacl aerosols. *Science*, 288(5464):301–306, apr 2000.

[103] Allen E Haddrell, David Lewis, Tanya Church, Reinhard Vehring, Darragh Murnane, and Jonathan P Reid. Pulmonary aerosol delivery and the importance of growth dynamics. *Therapeutic Delivery*, 8(12):1051–1061, nov 2017.

[104] Jeya Jeevahan, M. Chandrasekaran, G. Britto Joseph, R. B. Durairaj, and G. Mageshwaran. Superhydrophobic surfaces: a review on fundamentals, applications, and challenges. *Journal of Coatings Technology and Research*, 15(2):231–250, 2018.

[105] Naoe Hosoda and Stanislav Gorb Gorb. Underwater locomotion in a terrestrial beetle: combination of surface dewetting and capillary forces. *Proceedings of the Royal Society B: Biological Sciences*, 279(1745):4236–4242, October 2012.

[106] Philip Ball. Water as an active constituent in cell biology. *Chemical Reviews*, 108(1):74–108, 2008. PMID: 18095715.

[107] Barbara J. Finlayson-Pitts. Reactions at surfaces in the atmosphere: integration of experiments and theory as necessary (but not necessarily sufficient) for predicting the physical chemistry of aerosols. *Phys. Chem. Chem. Phys.*, 11(36):7760–7779, 2009.

[108] P. S. Liss. Processes of gas-exchange across an air-water interface. *Deep-sea Research*, 20(3):221–238, 1973.

[109] L. Merlivat and L. MEMERY. Gas-exchange across an air-water-interface - experimental results and modeling of bubble contribution to transfer. *Journal of Geophysical Research-oceans and Atmospheres*, 88(NC1):707–724, 1983.

[110] Ana Vila Verde, Peter G. Bolhuis, and R. Kramer Campen. Statics and dynamics of free and hydrogen-bonded oh groups at the air/water interface. *The Journal of Physical Chemistry B*, 116(31):9467–9481, 2012. PMID: 22788714.

[111] Yicun Ni, Scott M. Gruenbaum, and James L. Skinner. Slow hydrogen-bond switching dynamics at the water surface revealed by theoretical two-dimensional sum-frequency spectroscopy. *Proceedings of the National Academy of Sciences*, 110(6):1992–1998, February 2013.

[112] Yujin Tong, Ana Vila Verde, and R. Kramer Campen. The free OD at the air/D_2O interface is structurally and dynamically heterogeneous. *J. Phys. Chem. B*, 117(39):11753–11764, September 2013.

[113] Phillip L. Geissler. Water interfaces, solvation, and spectroscopy. *Annu. Rev. Phys. Chem.*, 64(1):317–337, April 2013.

[114] Aaron M. Jubb, Wei Hua, and Heather C. Allen. Organization of water and atmospherically relevant ions and solutes: Vibrational sum frequency spectroscopy at the vapor/liquid and liquid/solid interfaces. *Accounts of Chemical Research*, 45(1):110–119, January 2012.

[115] Vasudevan Venkateshwaran, Srivathsan Vembanur, and Shekhar Garde. Water-mediated ion interactions are enhanced at the water vapor-liquid interface. *Proceedings of the National Academy of Sciences*, 111(24):8729–8734, June 2014.

[116] Cho-Shuen Hsieh, R. Kramer Campen, Ana Celia Vila Verde, Peter Bolhuis, Han-Kwang Nienhuys, and Mischa Bonn. Ultrafast reorientation of dangling OH groups at the air/water interface. *Physical review letters*, 107:116102, 2011.

[117] Zhen Zhang, Lukasz Piatkowski, Huib J. Bakker, and Mischa Bonn. Communication: Interfacial water structure revealed by ultrafast two-dimensional surface vibrational spectroscopy. *Journal of Chemical Physics*, 135(2):021101, jul 2011.

[118] W. L. Jorgensen and C. Jenson. Temperature dependence of tip3p, spc, and tip4p water from npt monte carlo simulations: Seeking temperatures of maximum density. *Journal of Computational Chemistry*, 19(10):1179–1186, 1998. J. Comput. Chem.

[119] Jay W Ponder, Chuanjie Wu, Pengyu Ren, Vijay S Pande, John D Chodera, Michael J Schnieders, Imran Haque, David L Mobley, Daniel S Lambrecht, Robert A DiStasio Jr, et al. Current status of the amoeba polarizable force field. *The journal of physical chemistry B*, 114(8):2549–2564, 2010.

[120] F. Paesani. Temperature-dependent infrared spectroscopy of water from a first-principles approach. *Journal of Physical Chemistry A*, 115(25):6861–6871, June 2011.

[121] F. Paesani, S. Yoo, H. J. Bakker, and S. S. Xantheas. Nuclear quantum effects in the reorientation of water. *Journal of Physical Chemistry Letters*, 1(15):2316–2321, 2010.

[122] Thomas Spura, Christopher John, Scott Habershon, and Thomas D. Kühne. Nuclear quantum effects in liquid water from path-integral simulations using an ab initio force-matching approach. *Molecular Physics*, 113(8):808–822, 2015.

[123] I-F. Will Kuo, Christopher J. Mundy, Becky L. Eggimann, Matthew J. McGrath, J. Ilja Siepmann, Bin Chen, John Vieceli, and Douglas J. Tobias. Structure and dynamics of the aqueous liquid-vapor interface: A comprehensive particle-based simulation study. *The Journal of Physical Chemistry B*, 110(8):3738–3746, 2006. PMID: 16494432.

[124] Y. T. Wang, N. O. Hodas, Y. S. Jung, and R. A. Marcus. Microscopic structure and dynamics of air/water interface by computer simulations-comparison with sum-frequency generation experiments. *Physical Chemistry Chemical Physics*, 13(12):5388–5393, 2011.

[125] Gyoergy Hantal, Maria Darvas, Livia B. Partay, George Horvai, and Pal Jedlovszky. Molecular level properties of the free water surface and different organic liquid/water interfaces, as seen from itim analysis of computer simulation results. *Journal of Physics-condensed Matter*, 22(28):284112, July 2010.

[126] Kevin R. Wilson, R. D. Schaller, D. T. Co, R. J. Saykally, Bruce S. Rude, T. Catalano, and J. D. Bozek. Surface relaxation in liquid water and methanol studied by x-ray absorption spectroscopy. *The Journal of Chemical Physics*, 117(16):7738–7744, 2002. journal article.

[127] Tatsuya Ishiyama and Akihiro Morita. Vibrational spectroscopic response of intermolecular orientational correlation at the water surface. *The Journal of Physical Chemistry C*, 113(37):16299–16302, 2009.

[128] Mischa Bonn, Yuki Nagata, and Ellen H. G. Backus. Molecular structure and dynamics of water at the water–air interface studied with surface-specific vibrational spectroscopy. *Angewandte Chemie International Edition*, 54(19):5560–5576, 2015.

[129] HJ Bakker and JL Skinner. Vibrational spectroscopy as a probe of structure and dynamics in liquid water. *Chemical reviews*, 110(3):1498–1517, 2010.

[130] Fivos Perakis, Luigi De Marco, Andrey Shalit, Fujie Tang, Zachary R Kann, Thomas D Kühne, Renato Torre, Mischa Bonn, and Yuki Nagata. Vibrational spectroscopy and dynamics of water. *Chemical reviews*, 116(13):7590–7607, 2016.

[131] Rossend Rey, Klaus B Möller, and James T Hynes. Hydrogen bond dynamics in water and ultrafast infrared spectroscopy. *The Journal of Physical Chemistry A*, 106(50):11993–11996, 2002.

[132] B Auer, R Kumar, JR Schmidt, and JL Skinner. Hydrogen bonding and raman, ir, and 2d-ir spectroscopy of dilute hod in liquid d2o. *Proceedings of the National Academy of Sciences*, 104(36):14215–14220, 2007.

[133] BM Auer and JL Skinner. Ir and raman spectra of liquid water: Theory and interpretation. *The Journal of Chemical Physics*, 128(22):224511, 2008.

[134] JR Schmidt, ST Roberts, JJ Loparo, A Tokmakoff, MD Fayer, and JL Skinner. Are water simulation models consistent with steady-state and ultrafast vibrational spectroscopy experiments? *Chemical Physics*, 341(1-3):143–157, 2007.

[135] YR Shen. Surface properties probed by second-harmonic and sum-frequency generation. *Nature*, 337(6207):519–525, 1989.

[136] Elizabeth A Raymond, Teresa L Tarbuck, Mac G Brown, and Geraldine L Richmond. Hydrogen-bonding interactions at the vapor/water interface investigated by vibrational sum-frequency spectroscopy of hod/h2o/d2o mixtures and molecular dynamics simulations. *The Journal of Physical Chemistry B*, 107(2):546–556, 2003.

[137] Wei Gan, Dan Wu, Zhen Zhang, Ran-ran Feng, and Hong-fei Wang. Polarization and experimental configuration analyses of sum frequency generation vibrational spectra, structure, and orientational motion of the air/water interface. *The Journal of chemical physics*, 124(11):114705, 2006.

[138] Lori M Levering, M Roxana Sierra-Hernandez, and Heather C Allen. Observation of hydronium ions at the air- aqueous acid interface: vibrational spectroscopic studies of aqueous hcl, hbr, and hi. *The Journal of Physical Chemistry C*, 111(25):8814–8826, 2007.

[139] Akihiro Morita and James T. Hynes. A theoretical analysis of the sum frequency generation spectrum of the water surface. *Chemical Physics*, 258(2):371–390, 2000.

[140] Gregory R Medders, Volodymyr Babin, and Francesco Paesani. A critical assessment of two-body and three-body interactions in water. *Journal of chemical theory and computation*, 9(2):1103–1114, 2013.

[141] Kazuo Kitaura and Keiji Morokuma. A new energy decomposition scheme for molecular interactions within the hartree-fock approximation. *International Journal of Quantum Chemistry*, 10(2):325–340, 1976.

[142] Wei Chen and Mark S. Gordon. Energy decomposition analyses for many-body interaction and applications to water complexes. *The Journal of Physical Chemistry*, 100(34):14316–14328, 1996.

[143] Z. Khaliullin, Rustam, T. Bell, Alexis, and Martin Head-Gordon. Electron donation in the water–water hydrogen bond. *Chemistry – A European Journal*, 15(4):851–855, 2009.

[144] Eloy Ramos-Cordoba, Daniel S. Lambrecht, and Martin Head-Gordon. Charge-transfer and the hydrogen bond: Spectroscopic and structural implications from electronic structure calculations. *Faraday Discuss.*, 150:345–362, 2011.

[145] G. Jenness F. F. Wang, W. A. Al-Saidi, and K. D. Jordan. Assessment of the performance of common density functional methods for describing the interaction energies of (h2o)6 clusters. *The Journal of chemical physics*, 132:134303, 2010.

[146] Moilanen D. E., Fenn E. E., Lin Y. S., Skinner J. L., Bagchi B., and Fayer M. D. Water inertial reorientation: hydrogen bond strength and the angular potential. *Proceedings of the National Academy of Sciences of the United States of America*, 105:5295–5300, 2008.

[147] Damien Laage and James T. Hynes. Do more strongly hydrogen-bonded water molecules reorient more slowly? *Chemical Physics Letters*, 433:80–85, 2006.

[148] C. P. Lawrence and J. L. Skinner. Vibrational spectroscopy of hod in liquid d2o. iii. spectral diffusion, and hydrogen-bonding and rotational dynamics. *Journal Of Chemical Physics*, 118(1):264–272, 2003.

[149] Scott Habershon, Thomas E. Markland, and David E. Manolopoulos. Competing quantum effects in the dynamics of a flexible water model. *The Journal of Chemical Physics*, 131(2):024501, 2009.

[150] C. J. Tainter, L. Shi, and J. L. Skinner. Structure and oh-stretch spectroscopy of low- and high-density amorphous ices. *The Journal of Chemical Physics*, 140(13):134503, 2014.

[151] Adam P. Willard and David Chandler. Instantaneous liquid interfaces. *The Journal of Physical Chemistry B*, 114(5):1954–1958, 2010. PMID: 20055377.

[152] Ana Vila Verde and Reinhard Lipowsky. Cooperative slowdown of water rotation near densely charged ions is intense but short-ranged. *The Journal of Physical Chemistry B*, 117(36):10556–10566, 2013. PMID: 23947617.

[153] KB Jinesh and JWM Frenken. Experimental evidence for ice formation at room temperature. *Physical review letters*, 101(3):036101, 2008.

[154] K Koga. Xc zeng, and h, tanaka. *Phys. Rev. Lett*, 79:5262–5265, 1997.

[155] JM Rimsza, Jejoon Yeon, ACT Van Duin, and Jincheng Du. Water interactions with nanoporous silica: comparison of reaxff and ab initio based molecular dynamics simulations. *The Journal of Physical Chemistry C*, 120(43):24803–24816, 2016.

[156] Qiang Li, Jie Song, Flemming Besenbacher, and Mingdong Dong. Two-dimensional material confined water. *Accounts of chemical research*, 48(1):119–127, 2015.

[157] P Gallo, M Rovere, and E Spohr. Glass transition and layering effects in confined water: a computer simulation study. *The Journal of Chemical Physics*, 113(24):11324–11335, 2000.

[158] P Gallo, MA Ricci, and M Rovere. Layer analysis of the structure of water confined in vycor glass. *The Journal of chemical physics*, 116(1):342–346, 2002.

[159] Richard Renou, Anthony Szymczyk, and Aziz Ghoufi. Water confinement in nanoporous silica materials. *The Journal of Chemical Physics*, 140(4):044704, 2014.

[160] R Kumar, JR Schmidt, and JL Skinner. Hydrogen bonding definitions and dynamics in liquid water. *The Journal of chemical physics*, 126(20):05B611, 2007.

[161] Adam P Willard and David Chandler. The molecular structure of the interface between water and a hydrophobic substrate is liquid-vapor like. *The Journal of chemical physics*, 141(18):18C519, 2014.

[162] Aziz Ghoufi, Denis Morineau, Ronan Lefort, Ivanne Hureau, Leila Hennous, Haochen Zhu, Anthony Szymczyk, Patrice Malfreyt, and Guillaume Maurin. Molecular simulations of confined liquids: An alternative to the grand canonical monte carlo simulations. *The Journal of chemical physics*, 134(7):074104, 2011.

[163] Garima Mittal, Vivek Dhand, Kyong Yop Rhee, Soo-Jin Park, and Wi Ro Lee. A review on carbon nanotubes and graphene as fillers in reinforced polymer nanocomposites. *Journal of Industrial and Engineering Chemistry*, 21:11–25, 2015.

[164] Alberto Striolo. The mechanism of water diffusion in narrow carbon nanotubes. *Nano letters*, 6(4):633–639, 2006.

[165] G Nagy, MC Gordillo, E Guàrdia, and J Martí. Liquid water confined in carbon nanochannels at high temperatures. *The Journal of Physical Chemistry B*, 111(43):12524–12530, 2007.

[166] Ying-Chun Liu, Qi Wang, and Ling-Hong Lu. Water confined in nanopores: its molecular distribution and diffusion at lower density. *Chemical physics letters*, 381(1-2):210–215, 2003.

[167] Aleksandr Noy, Hyung Gyu Park, Francesco Fornasiero, Jason K Holt, Costas P Grigoropoulos, and Olgica Bakajin. Nanofluidics in carbon nanotubes. *Nano today*, 2(6):22–29, 2007.

[168] MHW Chan, KI Blum, SQ Murphy, GKS Wong, and JD Reppy. Disorder and the superfluid transition in liquid he 4. *Physical review letters*, 61(17):1950, 1988.

[169] M Cammarata, M Levantino, A Cupane, A Longo, A Martorana, and F Bruni. Structure and dynamics of water confined in silica hydrogels: X-ray scattering and dielectric spectroscopy studies. *The European Physical Journal E*, 12(1):63–66, 2003.

[170] A Malek and S Farooq. Kinetics of hydrocarbon adsorption on activated carbon and silica gel. *AIChE journal*, 43(3):761–776, 1997.

[171] P Gallo, M Rovere, and SH Chen. Water confined in mcm-41: a mode coupling theory analysis. *Journal of Physics: Condensed Matter*, 24(6):064109, 2012.

[172] Christoph Allolio, Felix Klameth, Michael Vogel, and Daniel Sebastiani. Ab initio h2o in realistic hydrophilic confinement. *ChemPhysChem*, 15(18):3955–3962, 2014.

[173] Xiu S Zhao, GQ Lu, and Graeme J Millar. Advances in mesoporous molecular sieve mcm-41. *Industrial & Engineering Chemistry Research*, 35(7):2075–2090, 1996.

[174] Dongyuan Zhao, Jinyu Sun, Quanzhi Li, and Galen D Stucky. Morphological control of highly ordered mesoporous silica sba-15. *Chemistry of materials*, 12(2):275–279, 2000.

[175] Bob Grünberg, Thomas Emmler, Egbert Gedat, Ilja Shenderovich, Gerhard H Findenegg, Hans-Heinrich Limbach, and Gerd Buntkowsky. Hydrogen bonding of water confined in mesoporous silica mcm-41 and sba-15 studied by 1h solid-state nmr. *Chemistry–A European Journal*, 10(22):5689–5696, 2004.

[176] Gerd Buntkowsky, Hergen Breitzke, Anna Adamczyk, Frank Roelofs, Thomas Emmler, Egbert Gedat, Bob Grünberg, Yeping Xu, Hans-Heinrich Limbach, Ilja Shenderovich, et al. Structural and dynamical properties of guest molecules confined in mesoporous silica materials revealed by nmr. *Physical Chemistry Chemical Physics*, 9(35):4843–4853, 2007.

[177] E Gedat, A Schreiber, GH Findenegg, I Shenderovich, H-H Limbach, and G Buntkowsky. Stray field gradient nmr reveals effects of hydrogen bonding on diffusion coefficients of pyridine in mesoporous silica. *Magnetic Resonance in Chemistry*, 39(S1):S149–S157, 2001.

[178] Reiner Anwander, Iris Nagl, Markus Widenmeyer, Günter Engelhardt, Olaf Groeger, Clemens Palm, and Thomas Röser. Surface characterization and functionalization of mcm-41 silicas via silazane silylation. *The Journal of Physical Chemistry B*, 104(15):3532–3544, 2000.

[179] DW Aksnes and L Gjerdåker. Nmr line width, relaxation and diffusion studies of cyclohexane confined in porous silica. *Journal of molecular structure*, 475(1):27–34, 1999.

[180] Lars Gjerdåker, Dagfinn W Aksnes, Geir Humborstad Sørland, and Michael Stöcker. Relaxation and diffusion studies of cyclohexane confined in mcm-41 by nmr. *Microporous and mesoporous materials*, 42(1):89–96, 2001.

[181] HE Stanley, P Kumar, G Franzese, L Xu, Z Yan, Marco G Mazza, SV Buldyrev, S-H Chen, and F Mallamace. Liquid polyamorphism: Possible relation to the anomalous behaviour of water. *The European Physical Journal Special Topics*, 161(1):1–17, 2008.

[182] Pablo G Debenedetti and Frank H Stillinger. Supercooled liquids and the glass transition. *Nature*, 410(6825):259–267, 2001.

[183] Pablo G Debenedetti. Supercooled and glassy water. *Journal of Physics: Condensed Matter*, 15(45):R1669, 2003.

[184] J-M Zanotti, M-C Bellissent-Funel, and S-H Chen. Relaxational dynamics of supercooled water in porous glass. *Physical Review E*, 59(3):3084, 1999.

[185] Alan K Soper, Fabio Bruni, and Maria Antonietta Ricci. Water confined in vycor glass. ii. excluded volume effects on the radial distribution functions. *The Journal of chemical physics*, 109(4):1486–1494, 1998.

[186] Christopher E Bertrand, Yang Zhang, and Sow-Hsin Chen. Deeply-cooled water under strong confinement: neutron scattering investigations and the liquid–liquid critical point hypothesis. *Physical Chemistry Chemical Physics*, 15(3):721–745, 2013.

[187] Wolfgang Götze. *Complex dynamics of glass-forming liquids: A mode-coupling theory*, volume 143. Oxford University Press on Demand, 2009.

[188] MA Ricci, F Bruni, P Gallo, M Rovere, and AK Soper. Water in confined geometries: experiments and simulations. *Journal of Physics: condensed matter*, 12(8A):A345, 2000.

[189] P Gallo, MA Ricci, and M Rovere. Layer analysis of the structure of water confined in vycor glass. *The Journal of chemical physics*, 116(1):342–346, 2002.

[190] Dario Corradini, Paola Gallo, and Mauro Rovere. Thermodynamics of supercooled water in solutions. In *Journal of Physics: Conference Series*, volume 177, page 012003. IOP Publishing, 2009.

[191] Meymanat Zokaie and Masumeh Foroutan. Comparative study on confinement effects of graphene and graphene oxide on structure and dynamics of water. *RSC Advances*, 5(49):39330–39341, 2015.

[192] Christoph Hartnig, Wolfgang Witschel, Eckhard Spohr, Paola Gallo, Maria Antonietta Ricci, and Mauro Rovere. Modifications of the hydrogen bond network of liquid water in a cylindrical sio2 pore. *Journal of Molecular Liquids*, 85(1-2):127–137, 2000.

[193] M Weigler, M Brodrecht, G Buntkowsky, and M Vogel. Reorientation of deeply cooled water in mesoporous silica: Nmr studies of the pore-size dependence. *The Journal of Physical Chemistry B*, 123(9):2123–2134, 2019.

[194] Gernot Rother, Andrew G Stack, Siddharth Gautam, Tingting Liu, David R Cole, and Andreas Busch. Water uptake by silica nanopores: impacts of surface hydrophilicity and pore size. *The Journal of Physical Chemistry C*, 124(28):15188–15194, 2020.

[195] S Le Caër, S Pin, S Esnouf, Q Raffy, J Ph Renault, J-B Brubach, G Creff, and P Roy. A trapped water network in nanoporous material: the role of interfaces. *Physical Chemistry Chemical Physics*, 13(39):17658–17666, 2011.

[196] Bettina Baumgartner, Jakob Hayden, Jérôme Loizillon, Sophia Steinbacher, David Grosso, and Bernhard Lendl. Pore size-dependent structure of confined water in mesoporous silica films from water adsorption/desorption using atr–ftir spectroscopy. *Langmuir*, 35(37):11986–11994, 2019.

[197] Evelyn Jantsch, Christian Weinberger, Michael Tiemann, and Thomas Koop. Phase transitions of ice in aqueous salt solutions within nanometer-sized pores. *The Journal of Physical Chemistry C*, 123(40):24566–24574, 2019.

[198] Andrew W Knight, Nikolai G Kalugin, Eric Coker, and Anastasia G Ilgen. Water properties under nano-scale confinement. *Scientific reports*, 9(1):1–12, 2019.

[199] Gerhard H Findenegg, Susanne Jähnert, Dilek Akcakayiran, and Andreas Schreiber. Freezing and melting of water confined in silica nanopores. *ChemPhysChem*, 9(18):2651–2659, 2008.

[200] Shigeharu Kittaka, Shuichi Takahara, Hideyuki Matsumoto, Yasuki Wada, Taku J Satoh, and Toshio Yamaguchi. Low temperature phase properties of water confined in mesoporous silica mcm-41: Thermodynamic and neutron scattering study. *The Journal of chemical physics*, 138(20):204714, 2013.

[201] S Jähnert, F Vaca Chávez, GE Schaumann, A Schreiber, M Schönhoff, and GH Findenegg. Melting and freezing of water in cylindrical silica nanopores. *Physical Chemistry Chemical Physics*, 10(39):6039–6051, 2008.

[202] Konrad Meister, Simona Strazdaite, Arthur L DeVries, Stephan Lotze, Luuk LC Olijve, Ilja K Voets, and Huib J Bakker. Observation of ice-like water layers at an aqueous protein surface. *Proceedings of the National Academy of Sciences*, 111(50):17732–17736, 2014.

[203] J-B Brubach, Al Mermet, A Filabozzi, A Gerschel, and P Roy. Signatures of the hydrogen bonding in the infrared bands of water. *The Journal of chemical physics*, 122(18):184509, 2005.

[204] Valentinos Mouarrawis, Raoul Plessius, Jarl Ivar Van der Vlugt, and Joost NH Reek. Confinement effects in catalysis using well-defined materials and cages. *Frontiers in chemistry*, 6:623, 2018.

[205] Ezequiel de la Llave, Valeria Molinero, and Damian A Scherlis. Role of confinement and surface affinity on filling mechanisms and sorption hysteresis of water in nanopores. *The Journal of Physical Chemistry C*, 116(2):1833–1840, 2012.

[206] J-B Brubach, A Mermet, Al Filabozzi, A Gerschel, D Lairez, MP Krafft, and P Roy. Dependence of water dynamics upon confinement size. *The Journal of Physical Chemistry B*, 105(2):430–435, 2001.

[207] Aashish Tuladhar, Stefan M Piontek, and Eric Borguet. Insights on interfacial structure, dynamics, and proton transfer from ultrafast vibrational sum frequency generation spectroscopy of the alumina (0001)/water interface. *The Journal of Physical Chemistry C*, 121(9):5168–5177, 2017.

[208] Mark J DelloStritto, James D Kubicki, and Jorge O Sofo. Effect of ions on h-bond structure and dynamics at the quartz (101)–water interface. *Langmuir*, 32(44):11353–11365, 2016.

[209] Laetitia Dalstein, Elizaveta Potapova, and Eric Tyrode. The elusive silica/water interface: Isolated silanols under water as revealed by vibrational sum frequency spectroscopy. *Physical Chemistry Chemical Physics*, 19(16):10343–10349, 2017.

[210] Jenée D Cyran, Michael A Donovan, Doris Vollmer, Flavio Siro Brigiano, Simone Pezzotti, Daria R Galimberti, Marie-Pierre Gaigeot, Mischa Bonn, and Ellen HG Backus. Molecular hydrophobicity at a macroscopically hydrophilic surface. *Proceedings of the national academy of sciences*, 116(5):1520–1525, 2019.

[211] Guillaume Stirnemann, Peter J Rossky, James T Hynes, and Damien Laage. Water reorientation, hydrogen-bond dynamics and 2d-ir spectroscopy next to an extended hydrophobic surface. *Faraday discussions*, 146:263–281, 2010.

[212] Simona Strazdaite, Jan Versluis, Ellen HG Backus, and Huib J Bakker. Enhanced ordering of water at hydrophobic surfaces. *The Journal of Chemical Physics*, 140(5):054711, 2014.

[213] Hidehiko Asanuma, Hidenori Noguchi, Kohei Uosaki, and Hua-Zhong Yu. Water structure at superhydrophobic quartz/water interfaces: a vibrational sum frequency generation spectroscopy study. *The Journal of Physical Chemistry C*, 113(50):21155–21161, 2009.

[214] Travis G Trudeau, Kailash C Jena, and Dennis K Hore. Water structure at solid surfaces of varying hydrophobicity. *The Journal of Physical Chemistry C*, 113(46):20002–20008, 2009.

[215] Sandra Roy and Dennis K Hore. Simulated structure and nonlinear vibrational spectra of water next to hydrophobic and hydrophilic solid surfaces. *The Journal of Physical Chemistry C*, 116(43):22867–22877, 2012.

[216] Eric Tyrode and Jonathan FD Liljeblad. Water structure next to ordered and disordered hydrophobic silane monolayers: a vibrational sum frequency spectroscopy study. *The Journal of Physical Chemistry C*, 117(4):1780–1790, 2013.

[217] Jiahui Zhang, Junjun Tan, Ruoqi Pei, Shuji Ye, and Yi Luo. Ordered water layer on the macroscopically hydrophobic fluorinated polymer surface and its ultrafast vibrational dynamics. *Journal of the American Chemical Society*, 143(33):13074–13081, 2021.

[218] LF Scatena, MG Brown, and GL Richmond. Water at hydrophobic surfaces: weak hydrogen bonding and strong orientation effects. *Science*, 292(5518):908–912, 2001.

[219] Rémi Khatib, Ellen HG Backus, Mischa Bonn, María-José Perez-Haro, Marie-Pierre Gaigeot, and Marialore Sulpizi. Water orientation and hydrogen-bond structure at the fluorite/water interface. *Scientific reports*, 6(1):1–10, 2016.

[220] Álvaro Cimas, Frederik Tielens, Marialore Sulpizi, Marie-Pierre Gaigeot, and Dominique Costa. The amorphous silica–liquid water interface studied by ab initio molecular dynamics (AIMD): local organization in global disorder. *Journal of Physics: Condensed Matter*, 26(24):244106, may 2014.

[221] L Liu, A Faraone, CY Mou, CW Yen, and SH Chen. Slow dynamics of supercooled water confined in nanoporous silica materials. *Journal of Physics: Condensed Matter*, 16(45):S5403, 2004.

[222] Silvina Cerveny, Francesco Mallamace, Jan Swenson, Michael Vogel, and Limei Xu. Confined water as model of supercooled water. *Chemical reviews*, 116(13):7608–7625, 2016.

[223] Ilja G Shenderovich, Gerd Buntkowsky, Andreas Schreiber, Egbert Gedat, Shasad Sharif, Judith Albrecht, Nikolaj S Golubev, Gerhard H Findenegg, and Hans-Heinrich Limbach. Pyridine-15 na mobile nmr sensor for surface acidity and surface defects of mesoporous silica. *The Journal of Physical Chemistry B*, 107(43):11924–11939, 2003.

[224] Adrien Lerbret, Gérald Lelong, Philip E Mason, Marie-Louise Saboungi, and John W Brady. Water confined in cylindrical pores: a molecular dynamics study. *Food biophysics*, 6(2):233–240, 2011.

[225] Shuichi Takahara, Naoya Sumiyama, Shigeharu Kittaka, Toshio Yamaguchi, and Marie-Claire Bellissent-Funel. Neutron scattering study on dynamics of water molecules in mcm-41. 2. determination of translational diffusion coefficient. *The Journal of Physical Chemistry B*, 109(22):11231–11239, 2005.

[226] Eckhard Spohr, Christoph Hartnig, Paola Gallo, and Mauro Rovere. Water in porous glasses. a computer simulation study. *Journal of Molecular Liquids*, 80(2-3):165–178, 1999.

[227] Ian C Bourg and Carl I Steefel. Molecular dynamics simulations of water structure and diffusion in silica nanopores. *The Journal of Physical Chemistry C*, 116(21):11556–11564, 2012.

[228] Xiang Yang Guo, Tobias Watermann, Shane Keane, Christoph Allolio, and Daniel Sebastiani. First principles calculations of nmr chemical shifts of liquid water at an amorphous silica interface. *Zeitschrift für Physikalische Chemie*, 226(11-12):1415–1424, 2012.

[229] Kenneth R Harris and Lawrence A Woolf. Pressure and temperature dependence of the self diffusion coefficient of water and oxygen-18 water. *Journal of the Chemical Society, Faraday Transactions 1: Physical Chemistry in Condensed Phases*, 76:377–385, 1980.

[230] Jincheng Du and Alastair N. Cormack. Molecular dynamics simulation of the structure and hydroxylation of silica glass surfaces. *Journal of the American Ceramic Society*, 88(9):2532–2539, 2005.

[231] P Gallo, M Rovere, and S-H Chen. Anomalous dynamics of water confined in mcm-41 at different hydrations. *Journal of Physics: Condensed Matter*, 22(28):284102, jun 2010.

[232] Christian Weinberger, Simon Vetter, Michael Tiemann, and Thorsten Wagner. Assessment of the density of (meso)porous materials from standard volumetric physisorption data. *Microporous and Mesoporous Materials*, 223:53–57, 2016.

[233] M.D. Hanwell, D.E. Curtis, and D.C. Lonie. Avogadro: an advanced semantic chemical editor, visualization, and analysis platform. *J. Cheminform*, 4, 2012.

[234] J. J. P. Stewart. Optimization of parameters for semi-empirical methods v: Modification of nddo approximations and application to 70 elements. *J. Mol. Model.*, 13:1173–1213, 2007.

[235] Thomas D. Kühne, Marcella Iannuzzi, Mauro Del Ben, Vladimir V. Rybkin, Patrick Seewald, Frederick Stein, Teodoro Laino, Rustam Z. Khaliullin, Ole Schütt, Florian Schiffmann, Dorothea Golze, Jan Wilhelm, Sergey Chulkov, Mohammad Hossein Bani-Hashemian, Valéry Weber, Urban Borštnik, Mathieu Taillefumier, Alice Shoshana Jakobovits, Alfio Lazzaro, Hans Pabst, Tiziano Müller, Robert Schade, Manuel Guidon, Samuel Andermatt, Nico Holmberg, Gregory K. Schenter, Anna Hehn, Augustin Bussy, Fabian Belleflamme, Gloria Tabacchi, Andreas Glöß, Michael Lass, Iain Bethune, Christopher J. Mundy, Christian Plessl, Matt Watkins, Joost VandeVondele, Matthias Krack, and Jürg Hutter. Cp2k: An electronic structure and molecular dynamics software package - quickstep: Efficient and accurate electronic structure calculations. *The Journal of Chemical Physics*, 152(19):194103, 2020.

[236] Thomas D. Kühne, Matthias Krack, and Michele Parrinello. Static and dynamical properties of liquid water from first principles by a novel car-parrinello-like approach. *Journal of Chemical Theory and Computation*, 5(2):235–241, 2009. PMID: 26610101.

[237] Giovanni Bussi, Davide Donadio, and Michele Parrinello. Canonical sampling through velocity rescaling. *The Journal of Chemical Physics*, 126(1):014101, 2007.

[238] Thomas F Willems, Chris H Rycroft, Michaeel Kazi, Juan C Meza, and Maciej Haranczyk. Algorithms and tools for high-throughput geometry-based analysis of crystalline porous materials. *Microporous and Mesoporous Materials*, 149(1):134–141, 2012.

[239] Richard Luis Martin, Berend Smit, and Maciej Haranczyk. Addressing challenges of identifying geometrically diverse sets of crystalline porous materials. *Journal of chemical information and modeling*, 52(2):308–318, 2012.

[240] Hamid Mosaddeghi, Saman Alavi, MH Kowsari, and Bijan Najafi. Simulations of structural and dynamic anisotropy in nano-confined water between parallel graphite plates. *The Journal of chemical physics*, 137(18):184703, 2012.

[241] Robert M Shroll and David E Smith. Molecular dynamics simulations in the grand canonical ensemble: Application to clay mineral swelling. *The Journal of chemical physics*, 111(19):9025–9033, 1999.

[242] Abhijit V Shevade, Shaoyi Jiang, and Keith E Gubbins. Molecular simulation study of water–methanol mixtures in activated carbon pores. *The Journal of Chemical Physics*, 113(16):6933–6942, 2000.

[243] Joël Puibasset and Roland J-M Pellenq. Grand canonical monte carlo simulation study of water structure on hydrophilic mesoporous and plane silica substrates. *The Journal of chemical physics*, 119(17):9226–9232, 2003.

[244] Alenka Luzar and David Chandler. Effect of environment on hydrogen bond dynamics in liquid water. *Physical review letters*, 76(6):928, 1996.

[245] Douglas R Banyai, Tatiana Murakhtina, and Daniel Sebastiani. Nmr chemical shifts as a tool to analyze first principles molecular dynamics simulations in condensed phases: the case of liquid water. *Magnetic Resonance in Chemistry*, 48(S1):S56–S60, 2010.

[246] Melville S Green. Markoff random processes and the statistical mechanics of time-dependent phenomena. *The Journal of Chemical Physics*, 20(8):1281–1295, 1952.

[247] Melville S Green. Markoff random processes and the statistical mechanics of time-dependent phenomena. ii. irreversible processes in fluids. *The Journal of chemical physics*, 22(3):398–413, 1954.

[248] Albert Einstein. Über die von der molekularkinetischen theorie der wärme geforderte bewegung von in ruhenden flüssigkeiten suspendierten teilchen. *Annalen der physik*, 4, 1905.

[249] Marian Von Smoluchowski. Zur kinetischen theorie der brownschen molekularbewegung und der suspensionen. *Annalen der physik*, 326(14):756–780, 1906.

[250] Manfred Holz, Stefan R Heil, and Antonio Sacco. Temperature-dependent self-diffusion coefficients of water and six selected molecular liquids for calibration in accurate 1h nmr pfg measurements. *Physical Chemistry Chemical Physics*, 2(20):4740–4742, 2000.

[251] Pauline Simonnin, Benoit Noetinger, Carlos Nieto-Draghi, Virginie Marry, and Benjamin Rotenberg. Diffusion under confinement: Hydrodynamic finite-size effects in simulation. *Journal of Chemical Theory and Computation*, 13(6):2881–2889, 2017.

[252] Neha Awasthi and Jochen S Hub. Simulations of pore formation in lipid membranes: reaction coordinates, convergence, hysteresis, and finite-size effects. *Journal of chemical theory and computation*, 12(7):3261–3269, 2016.

[253] F Klameth and M Vogel. Structure and dynamics of supercooled water in neutral confinements. *The Journal of chemical physics*, 138(13):134503, 2013.

[254] Martin Thomas, Martin Brehm, Reinhold Fligg, Peter Vöhringer, and Barbara Kirchner. Computing vibrational spectra from ab initio molecular dynamics. *Physical Chemistry Chemical Physics*, 15(18):6608–6622, 2013.

[255] Ellen HG Backus, Jan Schaefer, and Mischa Bonn. Probing the mineral–water interface with nonlinear optical spectroscopy. *Angewandte Chemie International Edition*, 60(19):10482–10501, 2021.

[256] Christian Weinberger, Frederik Zysk, Marc Hartmann, Naveen K. Kaliannan, Waldemar Keil, Thomas D. Kühne, and Michael Tiemann. The structure of water in silica mesopores – influence of the pore wall polarity. *Advanced Materials Interfaces*, 9(20):2200245, 2022.

[257] TW Allen, Serdar Kuyucak, and S-H Chung. The effect of hydrophobic and hydrophilic channel walls on the structure and diffusion of water and ions. *The Journal of chemical physics*, 111(17):7985–7999, 1999.

[258] Stefan Wilski, Jens Wipperfürth, Montgomery Jaritz, Dennis Kirchheim, Felix Mitschker, Peter Awakowicz, Rainer Dahlmann, and Christian Hopmann. Mechanisms of oxygen permeation through plastic films and barrier coatings. *Journal of Physics D: Applied Physics*, 50(42):425301, 2017.

[259] Stefan Wilski, Philipp Alizadeh, Lara Kleines, Christian Hopmann, and Rainer Dahlmann. Influence of pore spacing in barrier coatings on the mass transport through plastics—a simulative and experimental approach. *Journal of Physics D: Applied Physics*, 54(47):475305, 2021.

[260] Anastasios I Skoulidas, David M Ackerman, J Karl Johnson, and David S Sholl. Rapid transport of gases in carbon nanotubes. *Physical review letters*, 89(18):185901, 2002.

[261] Anastasios I Skoulidas and David S Sholl. Self-diffusion and transport diffusion of light gases in metal-organic framework materials assessed using molecular dynamics simulations. *The Journal of Physical Chemistry B*, 109(33):15760–15768, 2005.

[262] Tomohisa Yoshioka, Eisuke Nakanishi, Toshinori Tsuru, and Masashi Asaeda. Experimental studies of gas permeation through microporous silica membranes. *AIChE journal*, 47(9):2052–2063, 2001.

[263] AM Vieira-Linhares and NA Seaton. Non-equilibrium molecular dynamics simulation of gas separation in a microporous carbon membrane. *Chemical engineering science*, 58(18):4129–4136, 2003.

[264] JMD MacElroy and K Raghavan. Adsorption and diffusion of a lennard-jones vapor in microporous silica. *The Journal of chemical physics*, 93(3):2068–2079, 1990.

[265] Rajamani Krishna. Describing the diffusion of guest molecules inside porous structures. *The Journal of Physical Chemistry C*, 113(46):19756–19781, 2009.

[266] Anastasios I Skoulidas, David S Sholl, and Rajamani Krishna. Correlation effects in diffusion of ch4/cf4 mixtures in mfi zeolite. a study linking md simulations with the maxwell- stefan formulation. *Langmuir*, 19(19):7977–7988, 2003.

[267] Rajamani Krishna and Jasper M Van Baten. A molecular dynamics investigation of the unusual concentration dependencies of fick diffusivities in silica mesopores. *Microporous and mesoporous materials*, 138(1-3):228–234, 2011.

[268] Joshua D Moore, Jeremy C Palmer, Ying-Chun Liu, Thomas J Roussel, John K Brennan, and Keith E Gubbins. Adsorption and diffusion of argon confined in ordered and disordered microporous carbons. *Applied Surface Science*, 256(17):5131–5136, 2010.

[269] JM Don. MacElroy et al. Transport of an adsorbing vapour in a model silica system. *Journal of the Chemical Society, Faraday Transactions*, 87(13):1971–1987, 1991.

[270] Anne Goj, David S Sholl, E Demet Akten, and Daniela Kohen. Atomistic simulations of co2 and n2 adsorption in silica zeolites: the impact of pore size and shape. *The Journal of Physical Chemistry B*, 106(33):8367–8375, 2002.

[271] Raghavan Ranganathan, Srujan Rokkam, Tapan Desai, Pawel Keblinski, Peter Cross, and Richard Burnes. Modeling high-temperature diffusion of gases in micro and mesoporous amorphous carbon. *The Journal of Chemical Physics*, 143(8):084701, 2015.

Appendix

8.0.1 Acknowledgements

I would like to thank Prof. Dr. Jadran Vrabec for first sparking my interest into molecular dynamics, when I was studying mechanical engineering. Which led to me first working with Thomas as a student research assistant and then as a doctoral candidate in theoretical chemistry. Thomas has always worked to give us space to do the best science we can. I am thanking him for the good working culture he fostered and the help and critique he provided. The time working with him has shaped me as a person. I also want to thank my coworkers, especially Hossam, who helped me countless times, discussing solutions while running or in coffee breaks. I also want to thank my second supervisor Matthias for his trust and support with chemistry knowledge. I was very happy to have worked with competent and interesting scientists and engineers from the "Institute for lightweight design with hybrid systems" and to cooperate with members of the SFB-TR 78 in diverse scientific projects. Of course all of this would not have been possible without the great support by my parents, girlfriend and family. I also want to thank my friends for making me forget difficulties and overcome stress.

8.0.2 Publications

Ohto, T., Dodia, M., Xu, J., Imoto, S., Tang, F., Zysk, F., ... Nagata, Y. (2019). Accessing the accuracy of density functional theory through structure and dynamics of the water–air interface. The journal of physical chemistry letters, 10(17), 4914-4919.

Weinberger, C., Zysk, F., Hartmann, M., Kaliannan, N. K., Keil, W., Kühne, T. D., Tiemann, M. (2022). The Structure of Water in Silica Mesopores–Influence of the Pore Wall Polarity. Advanced Materials Interfaces, 9(20), 2200245.

Kaliannan, N. K., Henao Aristizabal, A., Wiebeler, H., Zysk, F., Ohto, T., Nagata, Y., & Kühne, T. D. (2020). Impact of intermolecular vibrational coupling effects on the sum-frequency generation spectra of the water/air interface. Molecular Physics, 118(4), 1620358.

Gujt, J., Zimmer, P., Zysk, F., Süß, V., Felser, C., Bauer, M., & Kühne, T. D. (2020). Water structure near the surface of Weyl semimetals as catalysts in photocatalytic proton reduction. Structural Dynamics, 7(3), 034101.

de los Arcos, T., Weinberger, C., Zysk, F., Damerla, V. R., Kollmann, S., Vieth, P., ... & Grundmeier, G. (2022). Challenges in the interpretation of gas core levels for the determination of gas-solid interactions within dielectric porous films by ambient pressure XPS. Applied Surface Science, 604, 154525.

Ojha, D., Henao, A., Zysk, F., & Kühne, T. D. (2022). Nuclear quantum effects on the vibrational dynamics of the water-air interface. arXiv preprint arXiv:2202.09592.

Mai, L., Maniar, D., Zysk, F., Schöbel, J., Kühne, T. D., Loos, K., & Devi, A. (2022). Influence of different ester side groups in polymers on the vapor phase infiltration with trimethyl aluminum. Dalton Transactions, 51(4), 1384-1394.

Franke, Jonas and Zysk, Frederik and Wilski, Stefan and Liedke, Oskar and Butterling, M. and Attallah, A.G. and Wagner, A. and Kühne, T.D. and Dahlmann, R. "Consideration of the Effect of Nanoscale Porosity on Mass Transport Phenomena in PECVD Coatings" [In preparation]

Frederik Zysk, Ana Vila Verde, Kristof Karhan, Hendrik Wiebeler, Jan Kessler and Thomas D. Kühne "Unravelling the relationship between the H-Bond strength and the reorientation dynamics" [In preparation]

Frederik Zysk and Thomas D. Kühne "Impact of Hydrophobicity and size on the structure and dynamics in silicaoxide nanopores" [In preparation]